

2

**PL-TR-95-2098**

## **Penetrating Radiation Environment and Effects Study**

**H. D. Voss**

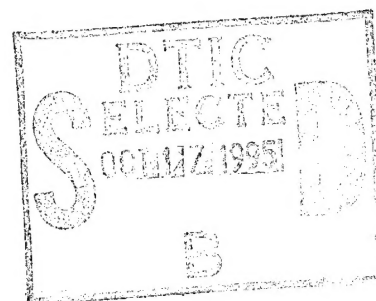
**W. L. Imhof**

**J. Mobilia**

**Space Sciences Laboratory, 091-20, B252  
Lockheed Martin Palo Alto Research Laboratory  
3251 Hanover Street  
Palo Alto, Ca. 94304**

**June 6, 1995**

**Final Report  
May 1990-June 1995**



**Approved for public release, distribution unlimited**

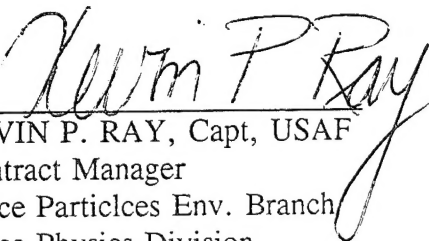


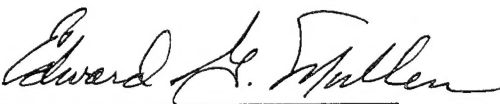
**PHILLIPS LABORATORY  
Directorate of Geophysics  
AIR FORCE MATERIEL COMMAND  
Hanscom AFB, MA 01731-3010**

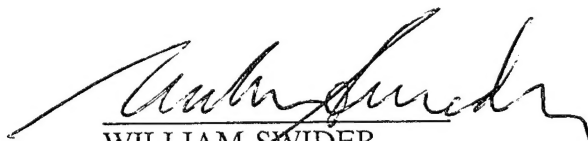
**19951013 009**

**DTIC QUALITY INSPECTED 3**

"This technical report has been reviewed and is approved for publication"

  
KEVIN P. RAY, Capt, USAF  
Contract Manager  
Space Particles Env. Branch  
Space Physics Division

  
EDWARD G. MULLEN, Chief  
Space Particles Env. Branch  
Space Physics Division

  
WILLIAM SWIDER  
Deputy Director  
Space Physics Division

This report has been reviewed by the ESC Public Affairs Office (PA) and is releasable to the National Technical Information Service (NTIS).

Qualified requestors may obtain additional copies from the Defense Technical Information Center. All others should apply to the National Technical Information Service.

If your address has changed, or if you wish to be removed from the mailing list, or if the addressee is no longer employed by your organization, please notify PL/TSI, 29 Randolph Road, Hanscom AFB, MA 01731-3010. This will assist us in maintaining a current mailing list.

Do not return copies of this report unless contractual obligations or notices on a specific document requires that it be returned.

REPORT DOCUMENTATION PAGE			Form Approved OMB No. 0704-0188	
Public reporting burden for this collection of information is estimated to average 1 hour per response, including the time for reviewing instructions, searching existing data sources, gathering and maintaining the data needed, and completing and reviewing the collection of information. Send comments regarding this burden estimate or any other aspect of this collection of information, including suggestions for reducing this burden, to Washington Headquarters Services, Directorate for Information Operations and Reports, 1215 Jefferson Davis Highway, Suite 1204, Arlington, VA 22202-4302, and to the Office of Management and Budget, Paperwork Reduction Project (0704-0188), Washington, DC 20503.				
1. AGENCY USE ONLY (Leave blank)	2. REPORT DATE 6 June 1995	3. REPORT TYPE AND DATES COVERED Final Report May 1990 to June 1995		
4. TITLE AND SUBTITLE  Penetrating Radiation Environment and Effects Study		5. FUNDING NUMBERS  PE62101F PR 7601 TA22 WU LD Contract F19128-90-C-0103		
6. AUTHOR(S) H.D. Voss* W.L. Imhof J. Mobilia				
7. PERFORMING ORGANIZATION NAME(S) AND ADDRESS(ES)  Lockheed Palo Alto Research Laboratory Space Science Laboratory 3251 Hanover Street Palo Alto, CA 94304-1191		8. PERFORMING ORGANIZATION REPORT NUMBER		
9. SPONSORING/MONITORING AGENCY NAME(S) AND ADDRESS(ES) Phillips Laboratory 29 Randolph Road Hanscom AFB, Ma. 01731-3010  Contract Manager : Kevin Ray Capt., USAF/GPSP		10. SPONSORING/MONITORING AGENCY REPORT NUMBER  PL-TR-95-2098		
11. SUPPLEMENTARY NOTES  * Taylor University, Physics Dept., 500 W. Reade Ave., Upland, In. 46989-1001				
12a. DISTRIBUTION / AVAILABILITY STATEMENT  Approved for public release; distribution unlimited		12b. DISTRIBUTION CODE		
13. ABSTRACT (Maximum 200 words)  This report summarizes some of the PREE achievements to date on data acquired from the Lockheed IMS-HI and SEP instruments on the CRRES satellite. The primary objectives of the PREE research are to, 1) inter-calibrate the ONR 307 instruments, 2) develop algorithms and software for understanding and modeling the radiation belts, 3) develop key parameters, and 4) study the dynamic radiation belt variations in the slot region and the outer belt. The new IMS-HI instrument performed well during the CRRES mission and has been inter-calibrated with the IMS-LO, SEP, and EPAS instruments. Much progress has been made in the development of key algorithms and software for mapping the electron, ion, and neutral flux. Energetic neutrals from the ring current have been observed directly and are an important low altitude and low latitude ionization source. Surveys of the medium energy (20-1000 keV) ion and neutral database indicate a sharp edge to the ring current flux which is not apparent in previous studies. The neutral flux is linked strongly with the low altitude edge of the ring current. To properly map the radiation belts and select key parameters a simple physical model was developed for the response of the magnetosphere to magnetic storms. The CRRES data indicate that the radiation belts including the inner belt are strongly modified during a sudden commencement (SC) on the order of several minutes. This momentary compression results in a net acceleration and transport of particles to low L in violation of the third invariant. For the 24 March 1991 magnetic storm the magnetopause is inferred to have penetrated to L ~ 3.0 resulting in the possible establishment of the "new inner belt".				
14. SUBJECT TERMS  Ions, Neutrals, Radiation Belts, Geomagnetic Storms, Acceleration		15. NUMBER OF PAGES 124		
		16. PRICE CODE		
17. SECURITY CLASSIFICATION OF REPORT Unclassified	18. SECURITY CLASSIFICATION OF THIS PAGE Unclassified	19. SECURITY CLASSIFICATION OF ABSTRACT Unclassified	20. LIMITATION OF ABSTRACT SAR	

## Contents

1. Introduction.....	1
2. Experiment and Data.....	3
2.1 Medium Energy Ion Mass Spectrometer (IMS-HI) .....	3
2.2 Spectrometer for Electrons and Protons (SEP ) .....	5
3. Research Activities .....	7
3.1 Intercalibrations .....	7
3.2 Neutral Atoms from the Ring Current .....	13
3.3 Radiation Belt Modeling .....	17
3.3.1 Model Description.....	17
3.3.2 Generation of the IMS-HI Database.....	17
3.3.3 IMS-HI Radiation Belt Model.....	19
3.3.4 AFPL Summary Database for IMS-HI .....	23
3.4 Magnetic Storm Dynamics.....	23
3.4.1 Wave Particle Interactions.....	28
3.4.2 Particle Transport and Acceleration during a Sudden Commencement .....	28
3.4.3 Simulation of the Radiation Belt Electron Bursts.....	32
3.5 Radiation Belt Acceleration and Transport .....	39
3.6 Rapid drop-off in the ion flux in the ring current.....	54
3.6.1 Rapid drop-off in the flux at the inner edge of the ring current.....	54
3.6.2 Narrow flux drop-offs and enhancements in the outer radiation belt..	54
4. Summary .....	55
5. References.....	56
Appendix 1 IMS-HI Instrument Paper.....	59
Appendix 2 SEP Instrument Paper.....	64
Appendix 3 Neutral Atom Paper.....	69
Appendix 4 Narrow Flux Dropouts in the Outer Radiation Belt Paper.....	82
Appendix 5 Abstracts.....	111

Box	
<input checked="" type="checkbox"/> <input type="checkbox"/> <input type="checkbox"/>	
Justification	
By	
Distribution	
Availability Codes	
Dist	Avail and/or Special
A-1	



## Figures

1	CRRES orbit plane with respect to the relevant magnetospheric particle regions .....	2
2	The principle of operation for IMS-HI .....	4
3	SEP Instrument Design .....	6
4a.	IMS-HI Color Mode 0 survey plot for orbit 587 .....	8
4b.	IMS-HI Color Mode 1 survey plot for orbit 587 .....	9
5	Flux line plots of $H^+$ , $He^+$ , and $O^+$ for orbit 587 .....	10
6	Example of intercalibration of IMS-HI with IMS-LO .....	11
7	Example of intercalibration of IMS-HI with SEP .....	11
8	Intercalibration for protons with the EPAS, PROTEL, and GOES instruments....	12
9	Energetic neutral atoms in the radiation belts .....	14
10	Mass spectrogram from IMS-HI detector 2 in the low altitude ion belt .....	15
11	Outline of IMS-HI data processing .....	18
12a	Mass spectrum plot from the IMS-HI detectors .....	20
12b	Line plot of Mode 1 data from the IMS-HI detectors .....	21
13	Summary display for the IMS-HI radiation belt Static Model .....	22
14	Spectrogram of $H^+$ flux from IMS-HI versus L-shell for CRRES mission.....	24
15	Spectrogram of $O^{++}$ flux from IMS-HI versus L-shell.....	25
16	Spectrogram of $He^+$ flux from IMS-HI versus L-shell for CRRES mission.....	26

17	Spectrogram of $H^+$ flux from IMS-HI versus L-shell for CRRES mission.....	27
18	The IMS-HI instrument differential ion flux for 18 keV and ..... 56 keV $H^+$ , the ULF wave is observed in the magnetometer data (upper panel) and 18 keV proton (lower panel) channel	29
19	The association of $B_z$ activity with 18 keV protons .....	29
20	Strong injected electron flux observed by IMS-HI during the..... 24 March 1991 magnetic storm onset	30
21	Greater than 50 MeV proton peak observed in the neutral detector ..... about 35 s before the large electron peak.	31
22	SEP electron data before, during, and after 24 March 91 storm.....	33
23	SEP instrument response to the slot region injection event of ..... 24 March 1991. The upper panel is for the E detector and the lower panel for the Anti-scintillator shield.	34
24	Monte Carlo simulation of the L=2.5 injection of energetic ..... electrons (inset) and the SEP A detector	35
25	Simulation of the longitude interval of injection (lower panel) ..... compared to the SEP E1 detector data.	36
26	Pitch angle sensitivity simulation .....	37
27	Simulation of the energy spectrum and pitch angle spread for ..... injected electrons at L=2.5	38
28	Tsyganenko model for $K_p > 5$ during the CRRES injection event .....	40
29	Field line trace of a dynamic magnetosphere using an image dipole .....	42

30	CRRES magnetic field data during the 25 March 1991 sudden commencement .....	43
31	Approximate shift of particle drift orbits during a magnetic compression due to an image dipole .....	44
32	Standoff distance vs. time based on the image dipole compression of the magnetosphere. ....	46
33	Magnetic field line displacement during a sudden commencement .....	47
34	Magnetic field compression (acceleration) factor during a large sudden commencement .....	48
35	Constant B drift contours for particles during various stages of the compression event .....	49
36	Model of acceleration and injection of > 10 MeV electrons, protons, and alphas into the radiation belt slot region during a sudden commencement. ....	50
37	Inner edge ring current ion flux .....	51
38	Inner edge ring current ion flux .....	52
39	Inner edge ring current ion flux .....	53

## Tables

1	IMS-HI Specifications.....	4
2	SEP Specifications .....	6

## 1. 0 Introduction

The purpose of this research activity is to improve our understanding of the Earth's radiation belts in the energy range  $> 18$  keV. At present, the dynamics of the radiation belts are only poorly understood. This is exemplified in the unexpected appearance of a new inner belt (Mullen et al., 1991 and Gussenhoven et al., 1991) and the injection of  $> 10$  MeV particles into the slot region (Vampola and Korth, 1992; Blake et al., 1992; Voss et al., 1992a) at the time of the 24 March 1991 storm. What the data show (Gussenhoven et al., 1991) is that, depending on orbit, both the existing proton and electron models can give large errors in dose that can compromise space systems performance and lifetime. The Combined Release and Radiation Effects Satellite (CRRES) is overcoming this problem by making state-of-the-art measurements in the relevant magnetospheric particle trapping and precipitation regions as illustrated in Figure 1.

Models exist for the radiation belt environment, but certain important features such as the energetic neutral and ion mass component are not well known. The belts are also quite variable in regard to intensity, energy, and composition. Large particle doses can result from solar particle events and these occur in a somewhat random and unpredictable manner. Therefore, for an accurate knowledge of the radiation environment in space, it is necessary to perform in situ measurements at the times and positions of concern. Such measurements have been performed on the CRRES satellite and permit the development of a comprehensive database.

The IMS-HI instrument (ONR 307-8-3) on the CRRES satellite (Voss et al., 1992b, see Appendix I) has the unique features that it is able to measure mass and energy ( $18 \text{ keV} < E < 2 \text{ MeV}$ ) simultaneously with 100% duty cycle, has a large geometrical factor and count rate dynamic range, and has good background rejection because the ion mass peak to valley ratio is measured. The neutral detector in the IMS-HI instrument is providing the first neutral atom model of the Earth's radiation belts. The ONR 307-3 Spectrometer for Electrons and Protons (SEP) measures with fine pitch-angle resolution the flux of energetic electrons in the energy range of 20 keV to 5 MeV and flux of energetic protons in the energy range 500 keV to 100 MeV.

The first area of investigation was to intercalibrate the IMS-HI instrument with ions from the IMS-LO instrument and with protons from the SEP instrument. Limited intercalibrations were also made with the AFGL EPAS and Protel instruments during the 24 March 1991 storm period. Because the IMS-HI neutral atom capability was unique to the CRRES satellite, the data near perigee were investigated first to "intercalibrate" with previous low-altitude satellite measurements (Voss et al., 1992c).

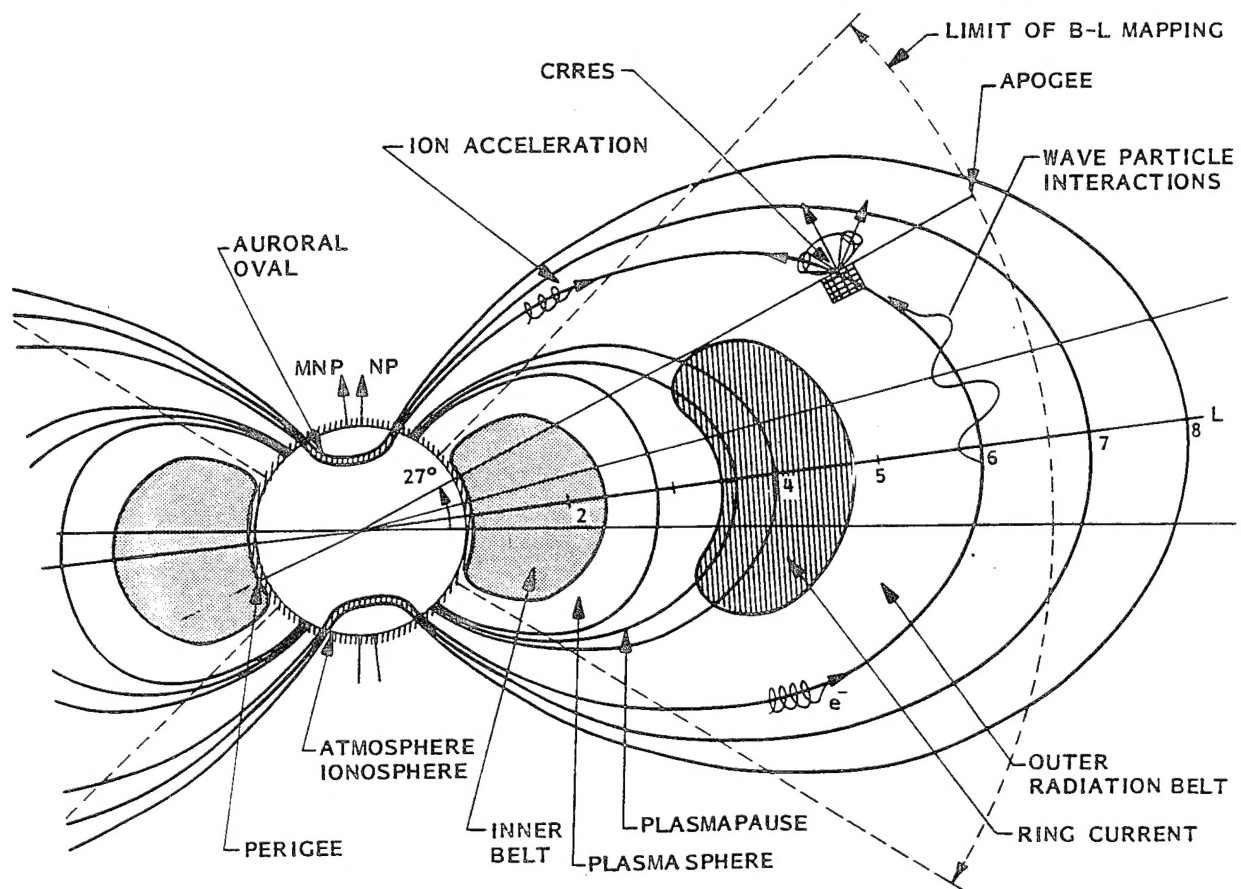


Figure 1 CRRES orbit plane with respect to the relevant magnetospheric particle regions

A series of computer programs were then developed as outlined in section 3.3 to process the IMS-HI data for a comprehensive radiation belt model. Of particular concern in these models is the rejection of background counts and the organization of the data according to location and magnetic storm dynamics. It has become very apparent in the CRRES data that storm time activity causes major transport and injection of particles in radiation belts. These topics are discussed in sections 3.4 and 3.5.

Of particular excitement is the preliminary finding that the magnetic shock on the magnetosphere by a large storm can penetrate down to L-shells as low as 2.0. A simple model using an image dipole moving toward the earth is used to simulate the shock. The data from this simple model can explain much of the observed CRRES data for the 24 March event 1991. This transport and acceleration mechanism is crucial to the proper modeling of the radiation belts.

## **2.0 Experiment and Data**

### **2.1 Medium Energy Ion Mass Spectrometer (IMS-HI)**

The primary objective of the medium energy ion mass spectrometer (ONR 307-8-3) on the CRRES satellite is to obtain the necessary data to construct models of the energetic ion (10 to 2000 keV-AMU/q<sup>2</sup>) and neutral atom (10 to 1500 keV) environment of the Earth's radiation belts. The spectrometer (Voss et al., 1992b) measures the energetic ion composition, energy spectrum, charge, and pitch angle distribution with good mass, temporal, and spatial resolution. The ion rejection in the neutral detector is <100 MeV-AMU/q<sup>2</sup>. The instrument principle of operation is based on ion momentum separation in a 7 kG magnetic field followed by energy and mass defect analysis using an array of cooled silicon solid-state detectors. The architecture is parallel with simultaneous mass and energy analysis at relatively high sensitivity (100% duty cycle). The instrument performed as designed in orbit with the major groups of hydrogen, helium, oxygen, and neutrals clearly resolved.

The conceptual instrument design is given in Figure 2 and the specifications are given in Table 1. An entrance collimator defines the ion beam angular resolution using a series of rectangular baffles and includes a broom magnet to reject electrons with energy less than 1 MeV. A 7-kG magnetic field then disperses the collimated ions onto a set of six passively cooled (-40 °C) silicon surface barrier detectors. The energy range, which varies with ion species, is approximately  $EM/q^2 = 10\text{-}2000$  keV-AMU/q<sup>2</sup>. A seventh sensor, located directly in line with the collimator, measures energetic neutrals.

Table 1 Medium Energy Ion Mass Spectrometer (IMS-HI) Specifications

Analyzer	7KG magnet( $q^2/m$ ) and Mass Defect
Sensors	Silicon Surface Barrier (-55°C)
Number of Imaging Sensors	7 at 0.5 cm <sup>2</sup> each
Look Direction from Spin Axis	75°
Particles and Energy Range:	
Neutrals	10-1500 keV
Protons	15-2000 keV
Helium	10-500 keV
Oxygen	20-130 keV
Oxygen++	20-500 keV
Other Ions	E>20 keV
Number of Differential Mass Channels	64
Number of High Rate Mass Channels	4
Number of Differential Energy Channels	6
Pitch Angle Resolution	4° FWHM
Geometric Factor	10 <sup>-2</sup> - 10 <sup>-3</sup> cm <sup>2</sup>
Duty Cycle	100%

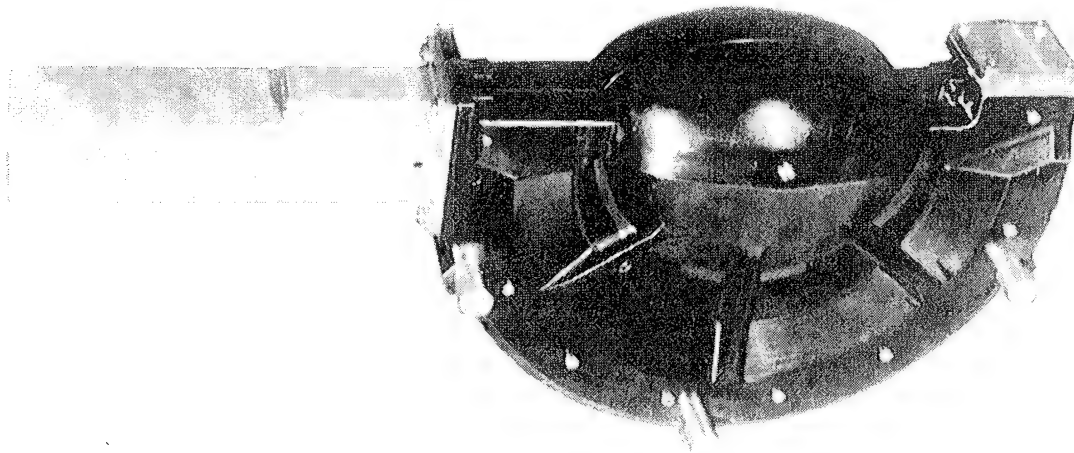
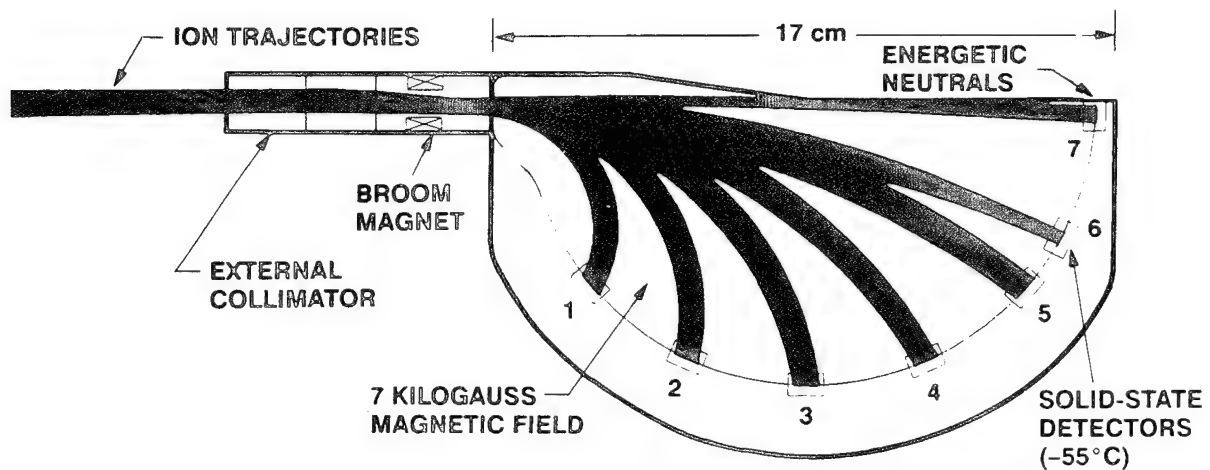


Figure 2 The principle of operation for IMS-HI

Solid-state detectors 1-7 are located at angle,  $\vartheta$ , of 40°, 65°, 90°, 115°, 140°, 162.5°, and 180°, respectively. Solid-state detectors 1-6 are n-type silicon having either 20 or 40 micrograms  $\text{cm}^{-2}$  of gold surface deposit. The neutral detector is of p-type silicon to improve light rejection and radiation damage sensitivity and has 20 micrograms  $\text{cm}^{-2}$  of aluminum surface deposit. The energy loss in surface barrier windows for H, He, and O is discussed by Voss, 1982. The mass defect in solid-state detectors results from energy loss of non-ionizing nuclear collisions within the solid that reduce the efficiency of electronic signal generation. The mass defect increases with atomic weight of the nuclei in a well understood way and causes further mass separation, with commensurate energy scatter, for the heavier nuclei.

Two basic modes of instrument operation are used: Mass Lock and Mass Scan. In the Mass Scan mode each of the seven solid-state detectors is pulse height analyzed into 256 levels of which 64 intervals are accumulated in memory and read out every eight seconds. This mode is used to scan all mass peaks within the range of the sensor relative to the background continuum. In the Mass lock mode, each of the seven solid-state sensors is pulse height analyzed into 256 levels, of which four intervals (typically four ions) are accumulated in memory and read out every half second. This mode is used for making rapid spectral snapshots of four ions as a function of pitch angle. Baseline operation of the instrument was a toggle mode (32.768 seconds) between Mass Lock mode and the Mass Scan mode. Additional information on the IMS-HI instrument is given in Appendix I.

## **2.2 Spectrometer for Electrons and Protons (SEP)**

The SEP design is based on the heavily successful SC-3 spectrometer (Reagan et al., 1981) flown on the SCATHA mission. Unlike the single-detector system used on SCATHA, SEP consists of three solid-state particle spectrometers oriented at 40°, 60°, and 80° from the spacecraft spin axis. A cross-sectional view of one of the telescopes is shown in Figure. 3. Each spectrometer has four detector elements labeled A, D, E, and E'. Various logic combinations of the four detector elements in each spectrometer are used to determine the particle types and energy ranges which are measured sequentially. The operational modes of each telescope are individually commandable.

Each of the three identical SEP particle telescopes has a high-resolution, 3° (FWHM) field of view provided by a long collimator (20 cm) containing 10 baffles. The



**Table 2                      SEP Specifications**

	Sensor A		Sensor B		Sensor C	
Mode	Energy range, MeV	Width, MeV	Energy range, MeV	Width, MeV	Energy range, MeV	Width, MeV
Electron 1	0.042-.324	0.0235	0.042-0.336	0.0245	0.041-.313	0.0227
Electron 2	0.164-4.93	0.397	0.171-5.12	0.413	0.170-5.11	0.412
Proton 1	0.875-6.60	0.478	0.916-6.7	0.482	0.920-6.8	0.490
Proton 2	2.5-38.7	3.01	2.2-33.7	2.62	2.0-30.4	2.37
Proton 3	35.8-80.2	3.7	31.2-69.9	3.22	28.2-63.1	2.91
Proton 4	45-94	4.08	45-105	5.00	45-110	5.42
Alphas	6.8-24	1.43	6.9-24.3	1.45	7.00-24	1.47

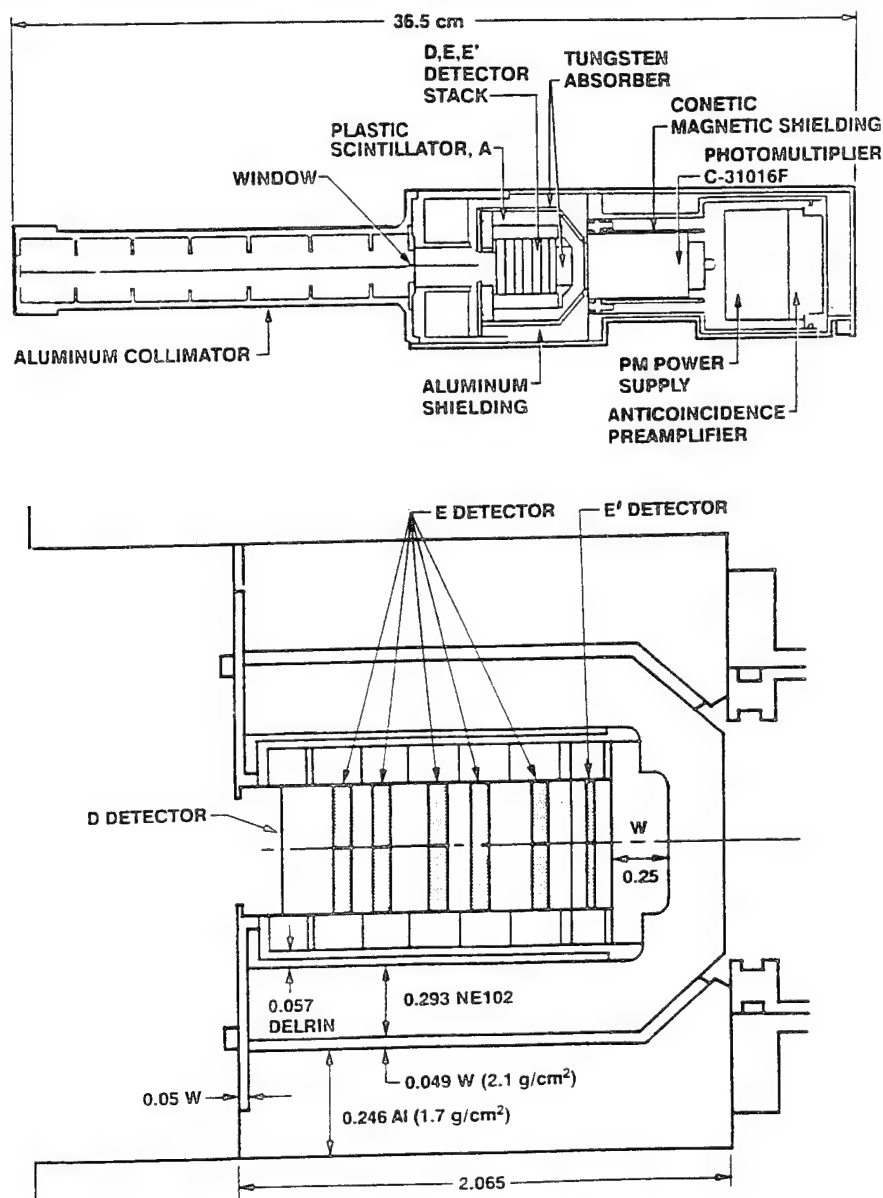


**Figure 3                      SEP Instrument Design**

collimators are identical to the ones used on the SC-3 instrument (Reagan et al., 1981) providing an instrument geometric factor of  $\sim 3 \times 10^{-3} \text{ cm}^2 \text{ sr}$ . For the  $80^\circ$  and  $60^\circ$  telescopes, measurements over 12 energy channels are obtained every 0.25 seconds with a dead time of 2 millisecond. Due to telemetry restrictions, the  $40^\circ$  telescope accumulates for 0.5 seconds with a dead time of 4 millisecond. Specifications for the SEP instrument are given in Table 2. Additional instrument details are given in the SEP instrument paper by Nightingale et al., 1992 (Appendix II).

### **3. Research Activities**

#### **3.1 Intercalibrations**

The quality of the measurements of the radiation environment directly affects the precision and reliability of studies utilizing the data. A continuing effort has been made to intercalibrate the various CRRES instruments in orbit. Potential problems have been found which include scattering in collimators and backgrounds due to bremsstrahlung, pile-up, and penetrating radiation. Unlike geostationary orbits, the CRRES orbit environment is demanding on the instrument hardware and therefore new and improved algorithms were developed to derive comprehensive flux measurements over all regions of the radiation belts.

An example of the IMS-HI survey plots for orbit 587 are shown in Figures 4a and 4b. Figure 4a only shows data from the 64 channel mass scan mode is shown. For detector 1 the 18 keV proton peak in the center mass channels is prominent. The mass channels covered for protons are numbers 38-42. Adjacent to this proton band, the penetrating background continuum is observed in all mass channels. The actual 18 keV  $\text{H}^+$  flux is thus the counts in the peak above the background continuum. Although this is obvious the IMS-HI instrument provides this added information for validating the ion flux. The more common broom-magnet spectrometers are unable to differentiate between background.

For  $L < 3$ , on both ends of the plot, the continuum is quite variable due to the inner belt and sudden commencement (0342 UT) associated particle penetration, yet no ion peak is observed in this region indicating the rapid drop off of ion flux and the importance of the peak to valley ratio background algorithms. For detector 2 hydrogen is located in mass channels, 58-63 and  $\text{He}^+$  is located in mass channels 33-35. Again the continuum is subtracted off of the peak count rates.

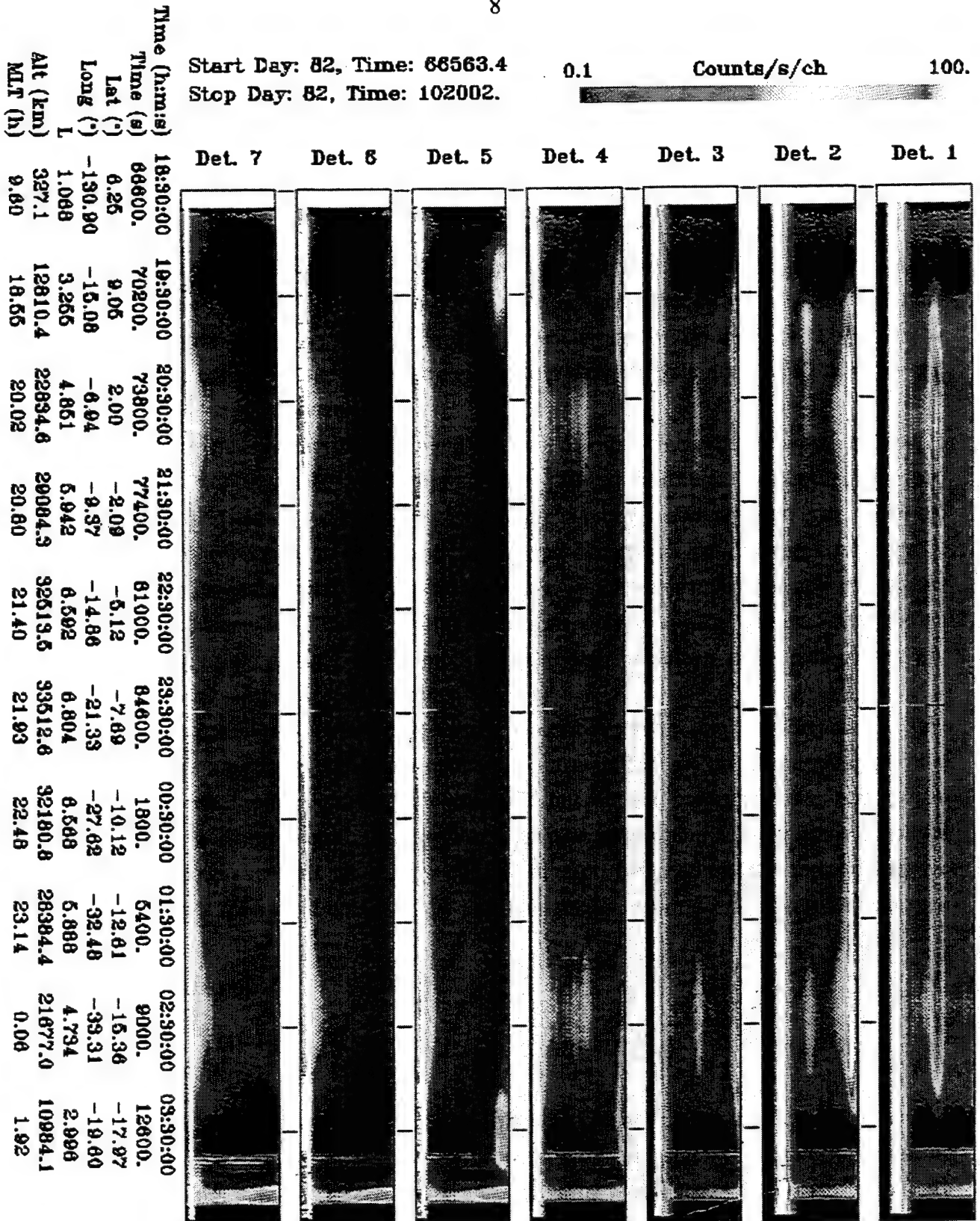
For the higher energy detectors the background subtraction algorithm is a combination of sensors. For example the proton flux in detector 6 is given by

Start Day: 82, Time: 88563.4  
Stop Day: 82, Time: 102002.

0.1

Counts/s/ch

100.



CRRES IMS-HI (ONR 307-8-3), Rev 587, Day 82

Figure 4a IMS-HI Color Mode 0 survey plot for orbit 587

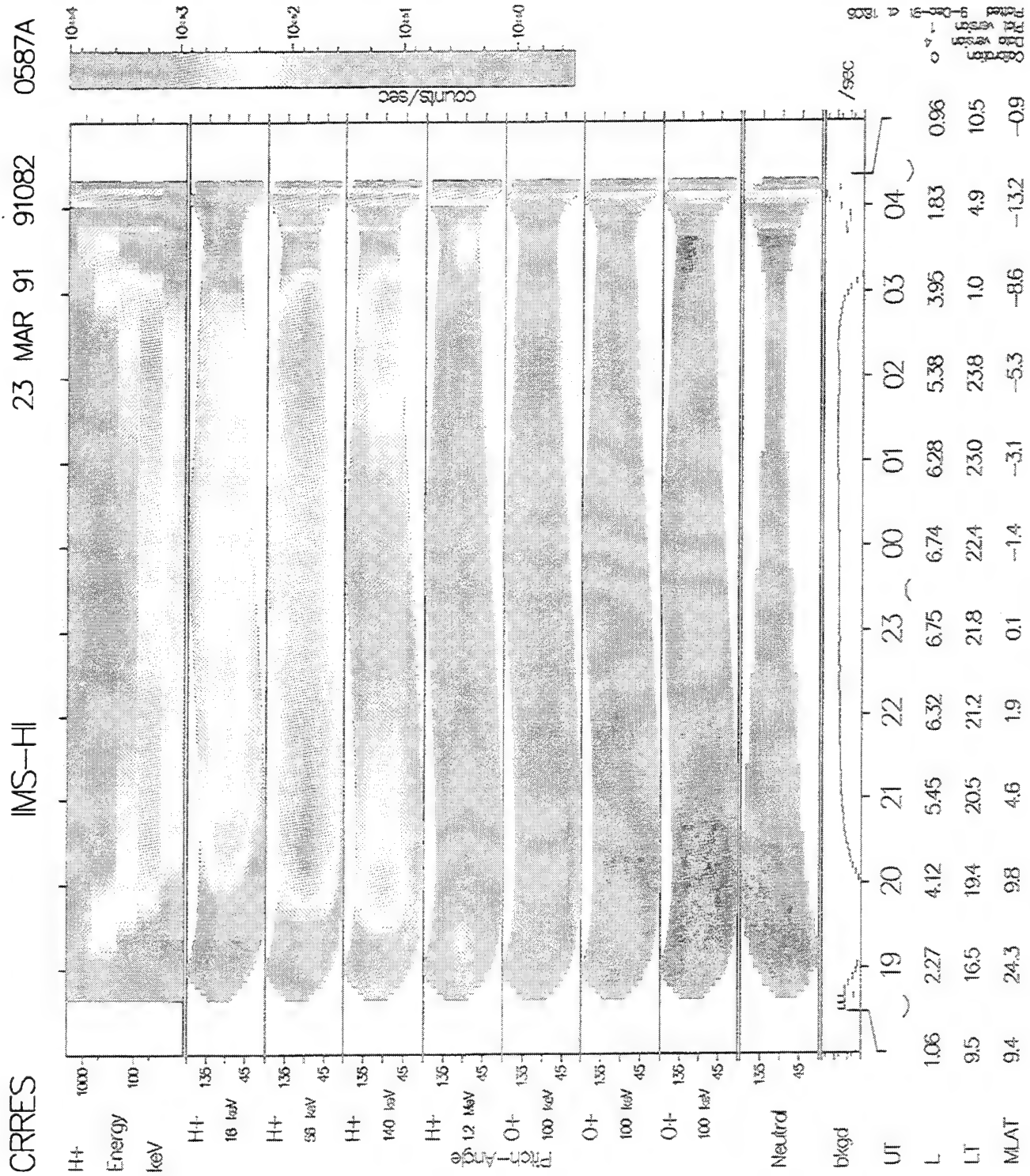


Figure 4b. IMS-HI Color Mode 1 survey plot for orbit 587

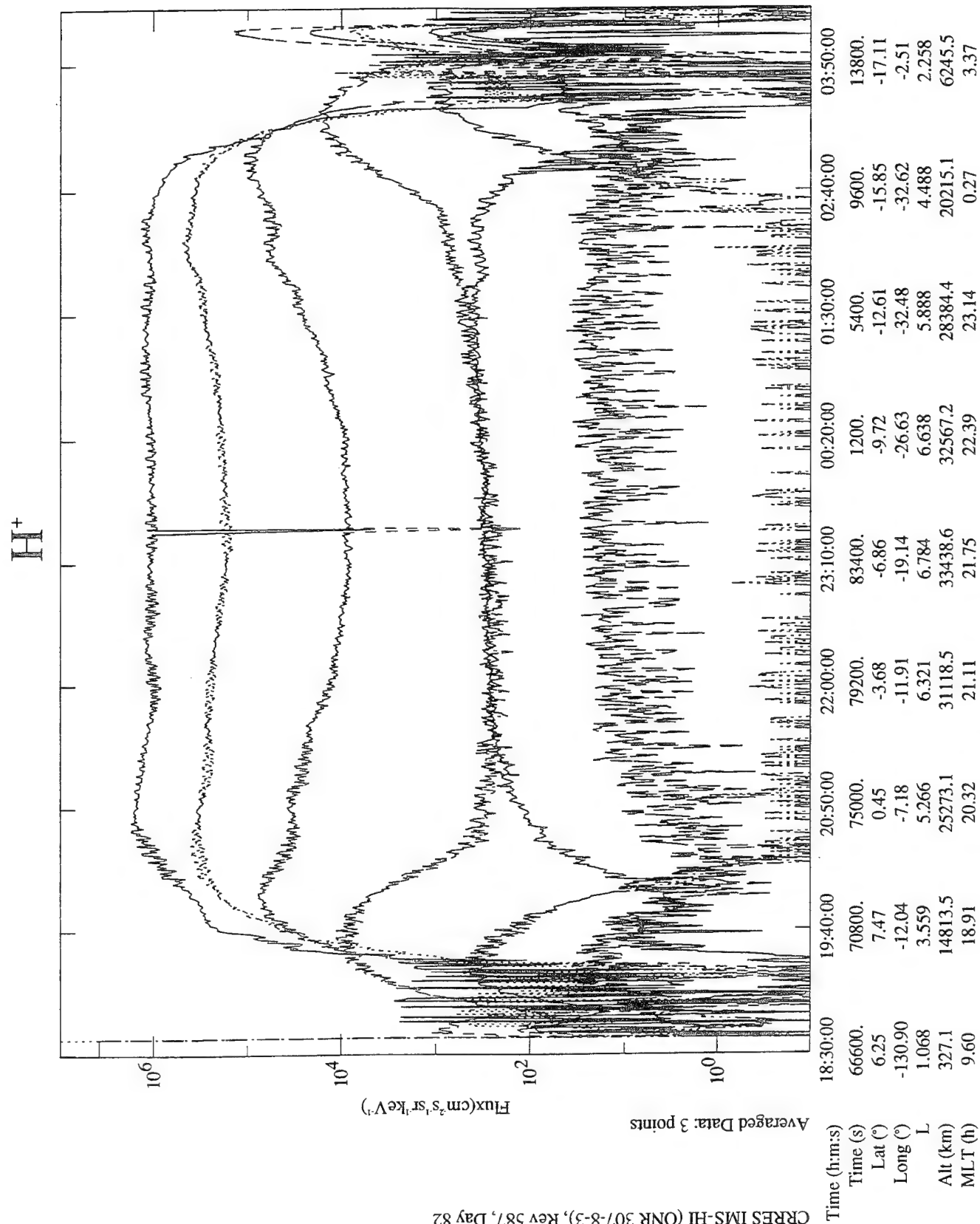
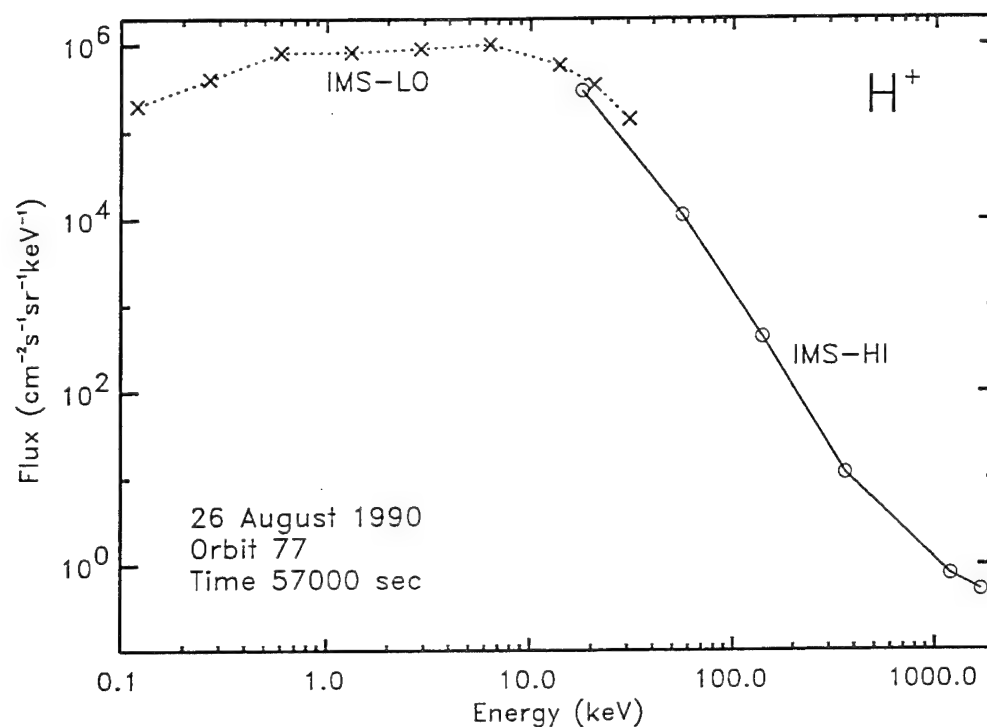
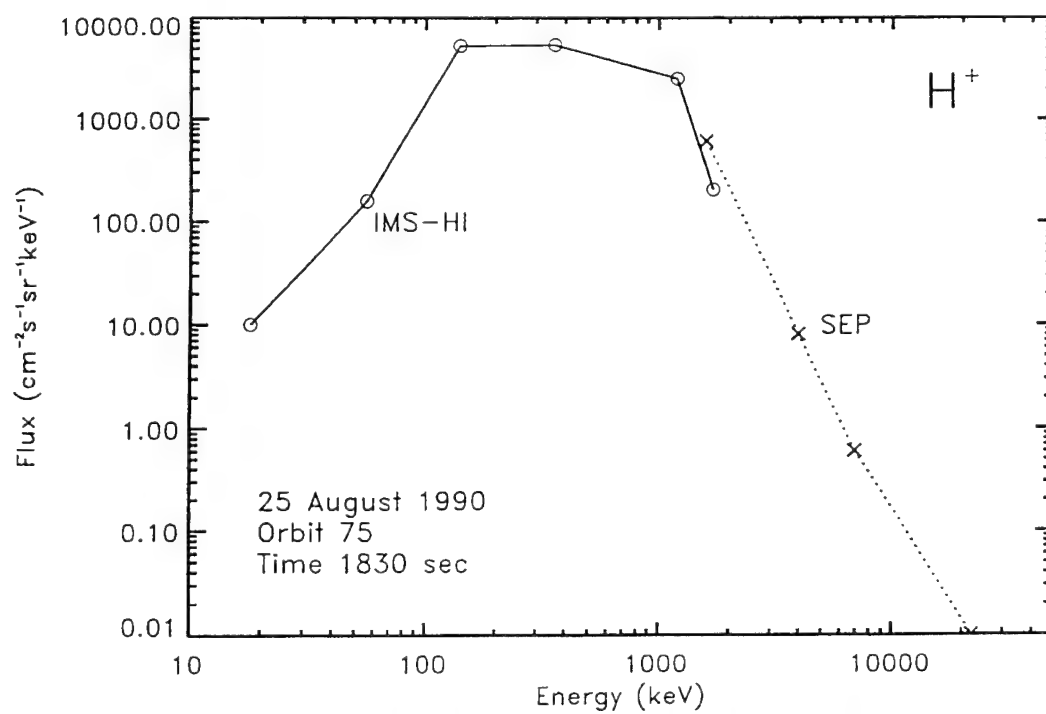


Figure 5 Flux line plots of  $H^+$ ,  $He^+$ , and  $O^+$  for orbit 587



**Figure 6** Example of intercalibration of IMS-HI with IMS-LO



**Figure 7** Example of intercalibration of IMS-HI with SEP

PROTON FLUX SPECTRUM  
ORBIT = 590 UT = 95832 TO 97920

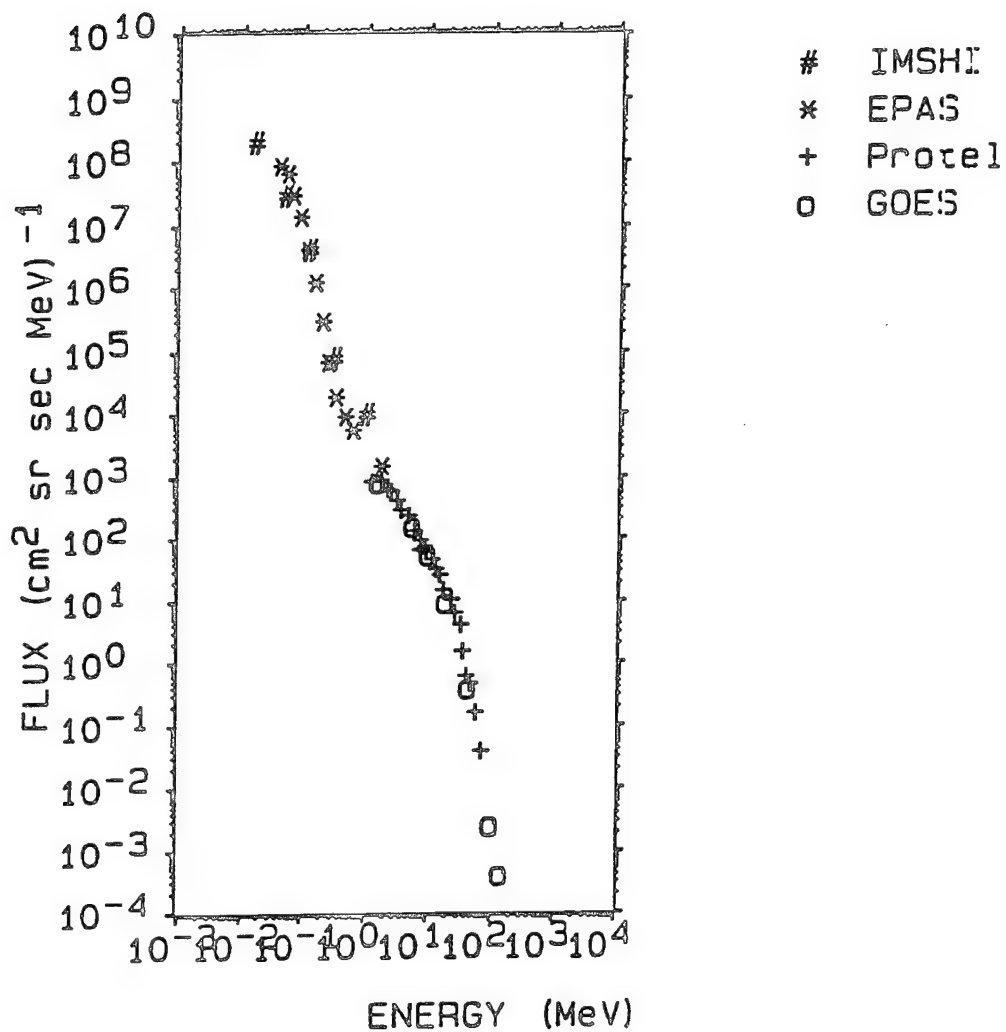


Figure 8 Intercalibration for protons with the EPAS, PROTEL, and GOES instruments



$$\text{Det 6 flux} = 0.14 \left[ \sum_{\text{ch 54}}^{63} \text{-ch63 of Det 5} \right] + 0.19 \left[ \sum_{\text{ch 54}}^{62} \text{of Det 5} - \sum_{\text{ch 43}}^{52} \text{of Det 5} \right]$$

A series of orbital flux profiles using the background subtraction is given in Figure 5 for orbit 587. For protons the L dependence of the various energies is apparent with the higher energies peaking at low L shells. The rapid drop off of 18 keV flux by several orders of magnitude at L~3.0 is surprising and indicates a strong loss process in this region. The enhanced flux of 1.7 MeV and E> 50 MeV protons is consistent with the on-going solar proton event. For He<sup>+</sup> the L dependence is in the opposite direction of the protons with the higher energies peaking at the higher L shells.

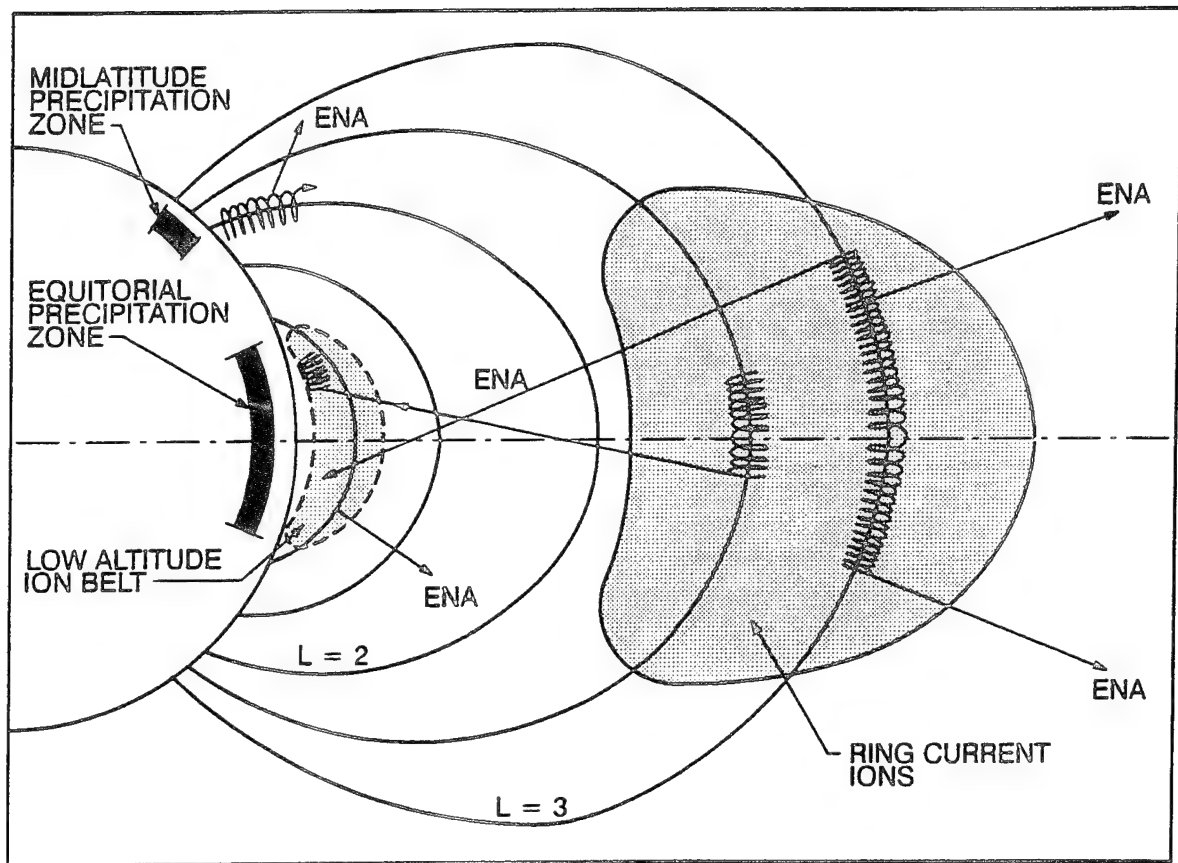
The IMS-HI instrument was intercalibrated with IMS-LO instrument for energetic protons. The IMS-HI 18 keV channel overlaps in energy with two of the IMS-LO channels. Both instruments have narrow fields-of-views. In general, the instruments agreed well in hydrogen flux measurements. An example of the typical overlap is shown in the spectrum of Figure 6. The IMS-HI instrument was intercalibrated with the SEP instrument for energetic protons in energy range 1 to 2 MeV. An example of the typical overlap is shown in the spectrum of Figure 7 for orbit 75.

Several periods of time were used to intercalibrate the IMS-HI with the EPAS and Protel instruments. An example of this intercalibration is shown in Figure 8. In this case the agreement is good, suggesting that the geometric factors and energy channel calibrations have been properly taken into account. However, when backgrounds are high (e.g. L<3) it appears that the EPAS instrument gives fluxes that are up to several orders of magnitude higher than from the IMS-HI. In fact, the IMS-HI instrument data indicates that there is a strong energy dependent cut off of ions in the slot region as indicated in Figures 4 and 5.

### 3.2 Neutral Atoms from the Ring Current

Modeling of the radiation belt protons and heavier ions requires an understanding of the neutral components. Energetic neutrals are the consequence of the charge exchange process of radiation belt ions with thermal ions, and vary according to the importance of this loss process. Because the neutrals are not restricted to the magnetic field they can rapidly fill all of the magnetosphere. Neutral atoms can therefore provide a mapping of the internal composition, spatial geometry, and temporal changes of the ring current, weighted by the appropriate cross sections and neutral hydrogen density; it provides a powerful method of studying the





2287NK

Figure 9 Energetic neutral atoms in the radiation belts

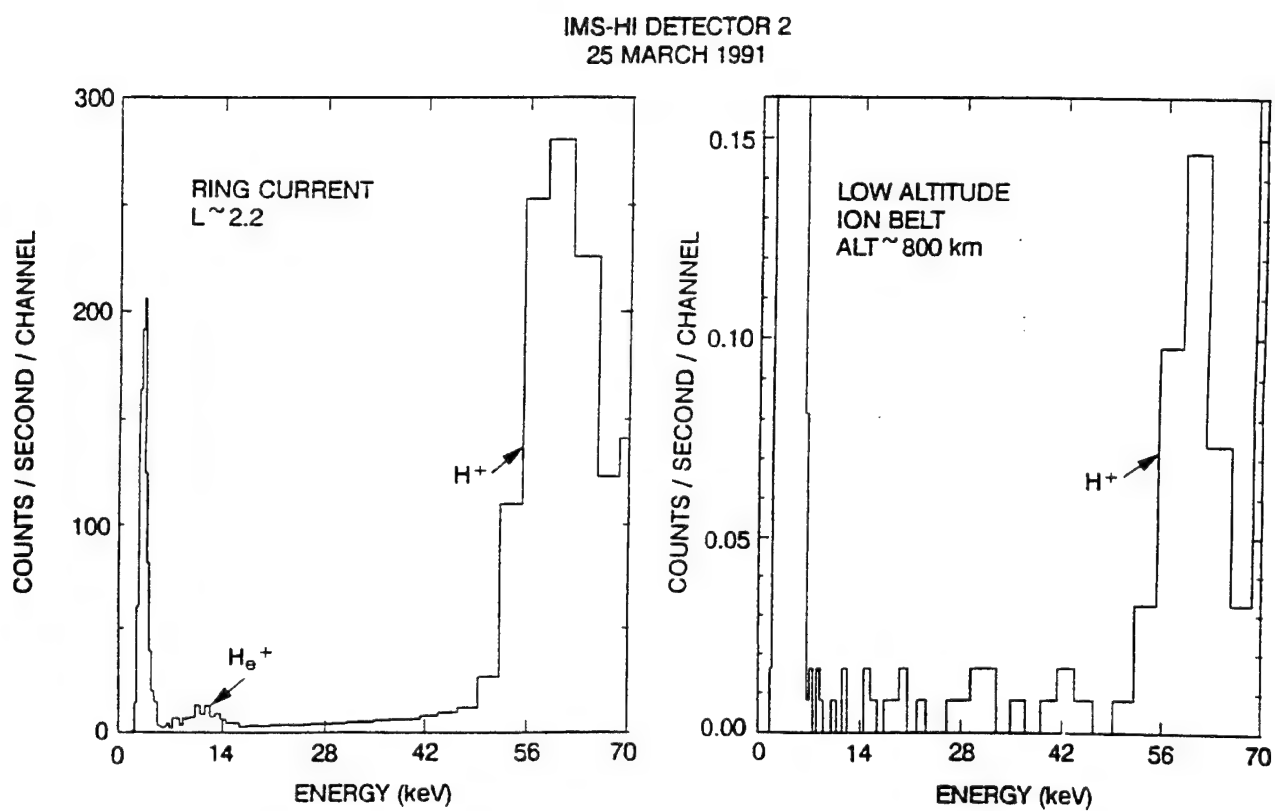


Figure 10 Mass spectrogram from IMS-HI detector 2 in the low altitude ion belt

magnetosphere (Roeloff et al., 1985, Hsieh et al. 1992). Using the IMS-HI instrument on the CRRES satellite the first in-depth investigation of the neutral atom radiation environment is being conducted.

The source of energetic neutral atoms (ENA) at low altitudes is believed to be a double-charge-exchange process of ions originating in the ring current (Moritz, 1972; Tinsley, 1981) as shown in Figure 9. The trapped ions of the ring current, by charge exchange with thermal hydrogen atoms of the geocorona, become high velocity neutral atoms which are focused, for those directed toward the earth, in the equatorial atmosphere where they again become ions by ionization collisions. In principle the spin of the CRRES satellite and orbit motion can be used to "raster scan" a portion of the magnetosphere to obtain a neutral atom image. In practice, however, the duty cycle associated with the spinning of the satellite and the background of the radiation belts make this a difficult task from CRRES. The injected energetic neutrals at low altitudes produce the equatorial precipitation zone and a temporary low altitude ion belt between 200 and 1000 km as illustrated in Figure 9.

Near perigee (<1000 km), when CRRES is below the inner belt, the IMS-HI instrument is able to directly view the ring current neutrals and ion composition of the low-altitude ion belt. Above the inner belt the IMS-HI instrument is able to make cross-sectional cuts of the ring current ion composition. About one day after the large magnetic storm of 24 March 1991 the ring current ions were observed to increase and move to lower altitudes. The ring current flux at this time extends down to  $L \sim 2.0$  and is dominated by hydrogen at  $E \sim 60$  keV.  $O^+$ ,  $O^{++}$ , and  $He^+$  are one to two orders of magnitude less in flux at these energies.

The ENA transported to low altitude is again charge exchanged by the atmosphere and temporarily becomes the low-altitude ion belt. Because the ions cannot support drift motion in much of the belt the loss rate is high. The steady-state ion population to first order is a mapping of the source composition multiplied by the appropriate atmospheric loss rates. A mass spectrogram of the low altitude ion belt for detector two is shown for the first time in Figure 10 for 25 March 1992. Also shown for comparison is the mass spectrogram of detector two near the inside edge of the ring current at  $L \sim 2.2$ . At this time the prominent ion, inferred from the ring current ENA, is  $H^+$  at 60 keV. The average low-altitude hydrogen count rate is about 2000 times lower than the average count rate in the ring current for the IMS-HI spectrometer.

### 3.3 Radiation Belt Modeling

#### 3.3.1 Model Description

The static version of the Empirical Model of medium energy ring current ion composition consist of a set of average equatorial energy and pitch-angle distributions of fluxes of  $H^+$ ,  $He^+$ , and  $O^+$  consistent with the IMS-LO database (Collin et al., 1992). The distributions are binned by energy and pitch-angle with 7 energy bins covering the whole of the IMS-HI energy range, 18 keV/AMU to 1.7 MeV/AMU, and eighteen,  $10^\circ$ , pitch angle bins which cover the full range of  $0^\circ$  to  $360^\circ$ , allowing for pitch-angle asymmetry. The model contains a  $H^+$ ,  $He^+$ , and  $O^+$  distribution for each of a number of spatial regions. These regions are defined by dividing the equatorial plane into six local time sections of four hours in width and into six radial sections between  $L = 2.5 R_e$  and  $L = 8.5 R_e$  each  $1.0 R_e$  in width. Associated with each flux value is an estimate of its statistical uncertainty and for development purposes a measure of the background and number of data samples used to determine the flux value (Collin et al., 1992). The model can therefore be used to determine the average ion distributions away from the equatorial plane, assuming the absence of parallel electric fields and wave-particle interactions, by mapping the equatorial distributions down the field lines to the location of interest.

In addition to the medium energy ion composition model a similar model is used for energetic neutrals. In this case the neutrals are binned into four energy ranges (out of 64 energy channels) and into eighteen angular bins relative to the earth's geometry over  $0$  to  $360^\circ$ . Because the neutral flux is several orders of magnitude less than the ring current ion flux the background must be validated for inclusion into the model.

#### 3.3.2 Generation of IMS-HI Database

A schematic of the IMS-HI data processing is shown in Figure 11. The first stage of processing is to unpack and decode the data on the agency tapes and then write the data from each orbit to a group of files for each instrument together with ephemeris and magnetometer files. At this stage all data is in the form of counts and engineering units at the full resolution of the instrument. This forms the high resolution database (level 1) and is stored on optical disks.

In level 2 the IMS-HI instrument data is stripped from the optical disk file along with other selected parameters and binary compressed. From this file the computational burden is significantly reduced for the summary database and level three processing. As indicated in Figure 11 level three processing has four formats: 1) Mode 0 color spectrograms of 64 channel mass (Figure 4a),

# IMS-HI Data Processing

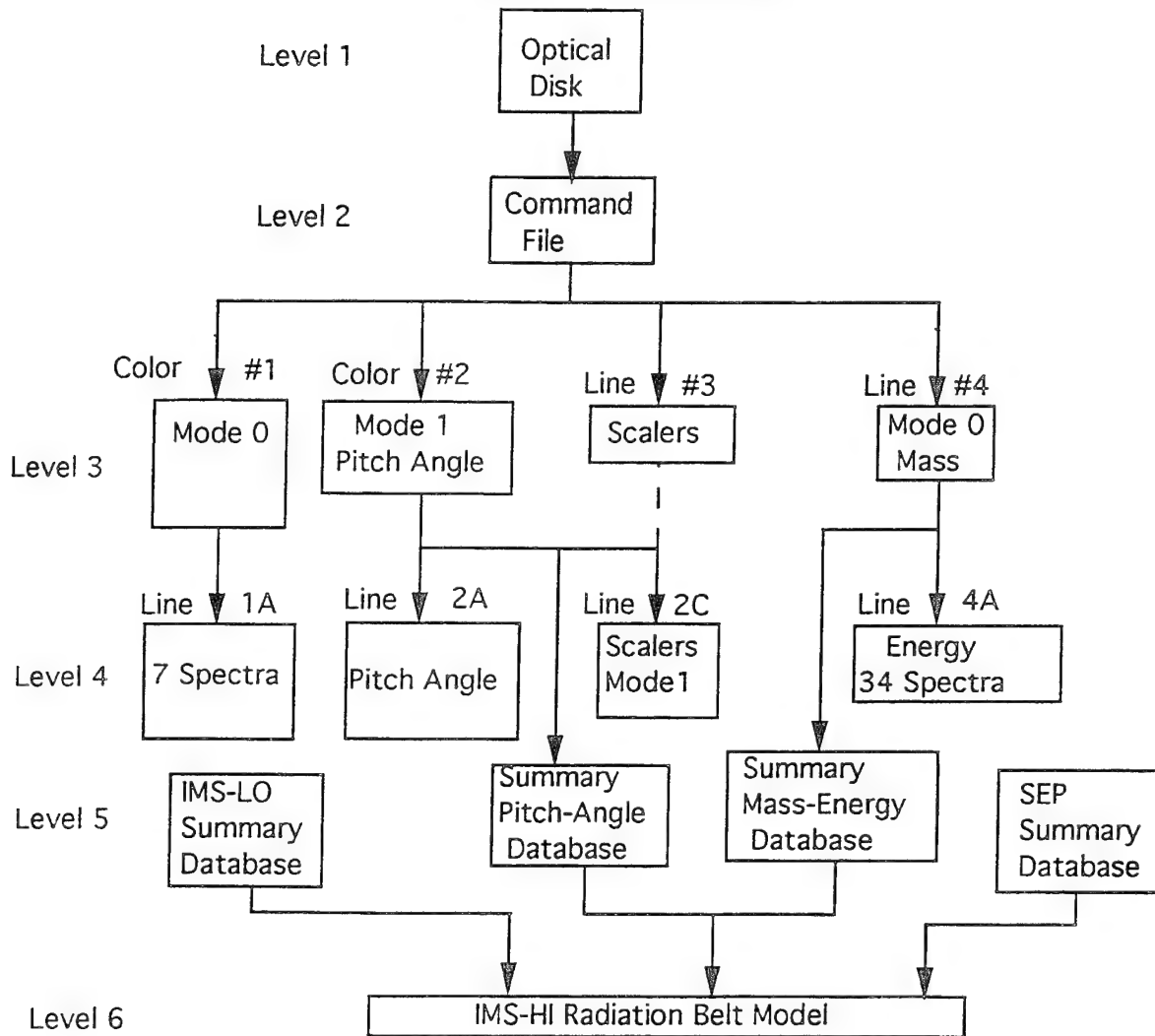


Figure 11 Outline of IMS-HI data processing

2) Mode 1 color pitch angle plots (Figure 4b), 3) Line plots/files of scaler data, and 4) at line plots of Mode 0 mass.

In level 4 processing four types of line plots are possible: mass spectrums plot up to seven detectors, (1A) pitch angle plot of 3 mass intervals (2A), mode 1 scales line plots, and 1 energy line plots of 3 mass intervals. An example of formats 1A is given in Figure 12a and of format 2 in Figure 12b.

Based on review of the level 3 and level 4 processing the level 5 summary database is being constructed. This IMS-HI Summary Database is a compact, partially processed database consisting of averages, over 131 seconds, of IMS-HI ion and neutral data sorted by energy and pitch angle. Supporting data include time, background count rate, status information, measured magnetic field and ephemeris information. The ion and neutral data are recorded as count rates in order to make the database independent of revisions to instrument calibration with cross calibrations underway. Calibrations are applied to the count rates where the database is accessed. The Summary Database is suitable for rapid retrieval of energy spectra, pitch angle distributions or survey and for the basis forms the statistical studies. An attempt has been made to keep the database similar to the IMS-LO database (Collin et al., 1992) so that the final Radiation Belt Model for IMS-HI will be consistent with the IMS-LO model. In level 6 processing the final IMS-HI Radiation Belt Model is formed. The model results are designed so that they can be compared with the IMS-LO and IMS-HI databases as well and for application of existing dose/shielding algorithms.

### **3.3.3 IMS-HI Radiation Belt Model**

The IMS-HI Summary Database can be used for both static and dynamic modeling. The model average equatorial distributions are constructed by accumulating and averaging equatorial distributions from many orbits. Similar to IMS-LO the data are binned by their energy and equatorial pitch-angle and sorted into ranges of L and local time. These distributions are mapped adiabatically from the satellite location to the equatorial plane. The mapping makes use of the modeled values of the local magnetic field strength and the minimum field on the same field line which are provided in the CRRES ephemeris files.

The quality of the database is strongly dependent on an understanding of contamination sources, especially for the neutral atom database. The capability of IMS-HI to measure the peak to valley ratio in each spectrometer mass channel eliminates background to a great degree (see section 3.1). In addition a quality factor (1 to 10) based on the signal to background ratio is given

# ONR-307 IMS-HI : MASS DISTRIBUTION

Averaged Data between 83, 25005.8 and 83, 27004.6

March 24, 1991

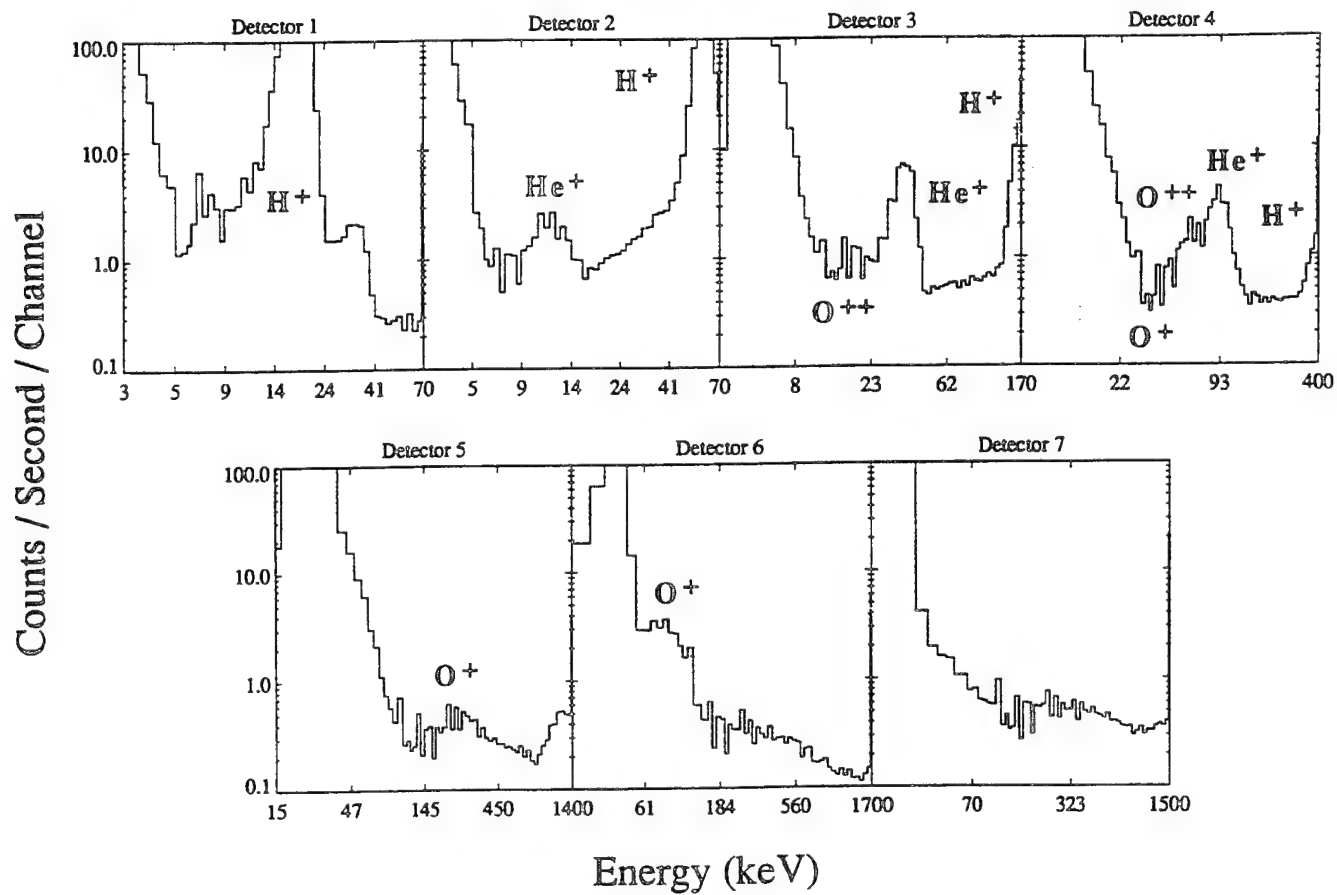


Figure 12a Mass spectrum plot from the IMS-HI detectors

# ONR-307 IMS-HI : MASS DISTRIBUTION

Rev 587, Detector 1

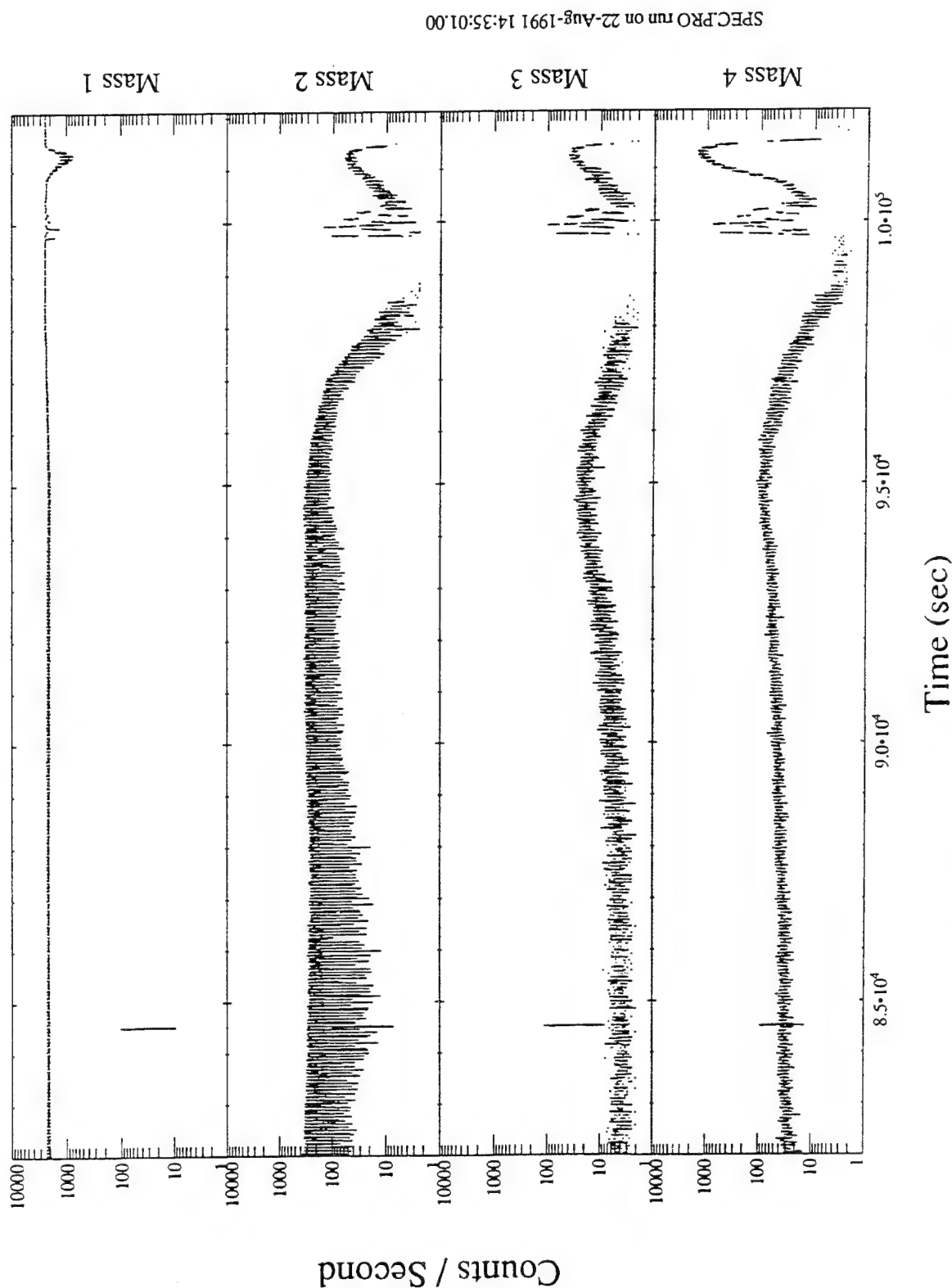


Figure 12b Line plot of Mode 1 data from the IMS-HI detectors



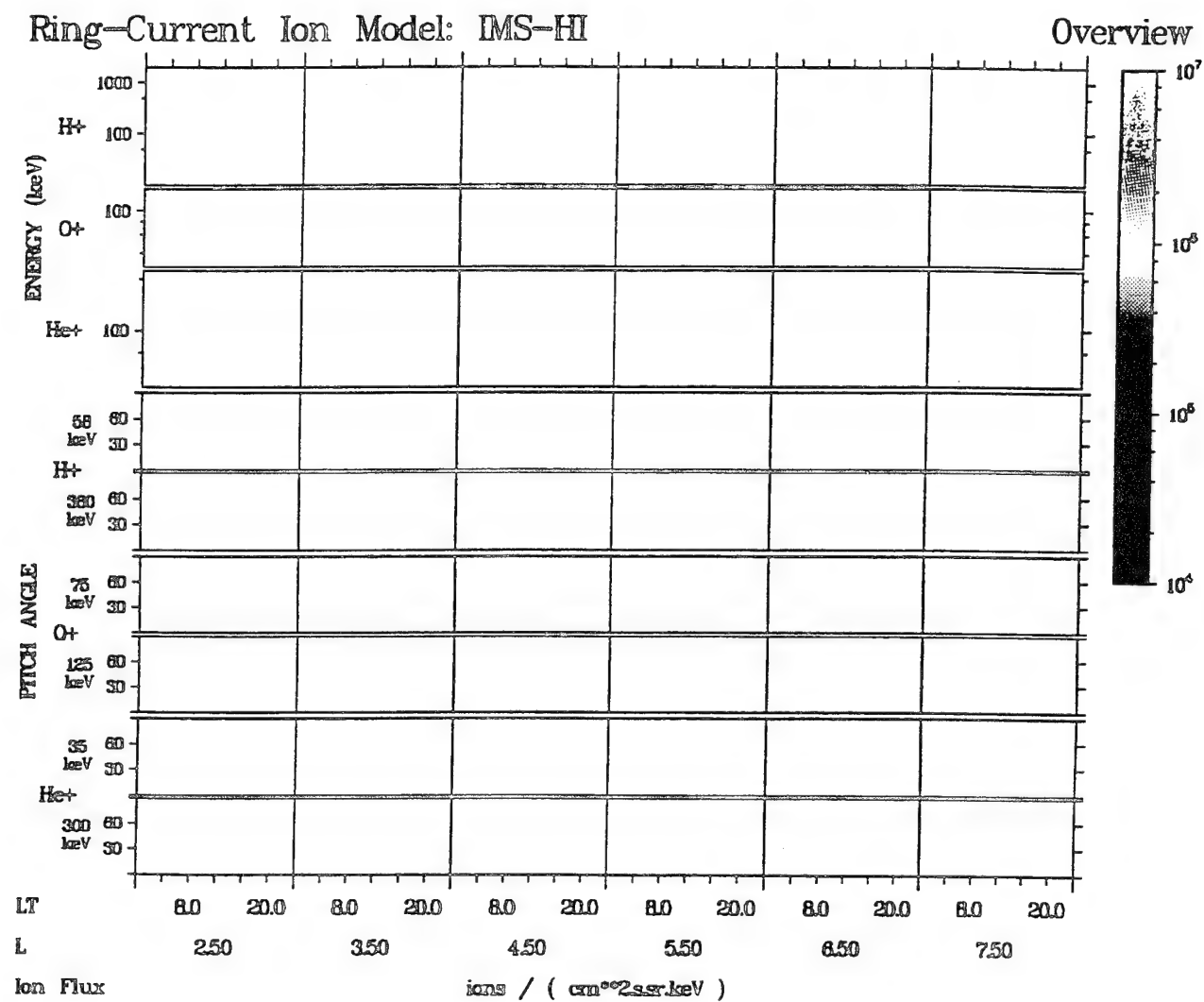


Figure 13 Summary display for the IMS-HI radiation belt Static Model

to each interval of time so that data quality can be tracked. Furthermore, each orbit's summary data will be checked manually with the high resolution color spectrogram data to verify that the data quality is valid. With the background rejection accurate data should be obtained over the whole orbit.

Figure 13 is a prototype display of data for the static model. The layout is based on a portion of the Summary Database and is consistent with the IMS-LO database. The top panel contains energy spectra, averaged over pitch angle for  $H^+$ ,  $He^+$ , and  $O^+$ . The bottom panels contain  $H^+$ ,  $He^+$ , and  $O^+$  pitch angle distributions at selected energy bands. These panels are divided horizontally by bold black vertical lines into six broad strips which correspond to six ranges of L. The left most of the broad strips, for example, corresponds to divided strips corresponding to a magnetic local time interval. Each of the narrow strips displays the average equatorial energy spectral and pitch-angle distributions for its own local time L range. As in IMS-LO database the energy spectra in the top panel (or pitch angle in the lower panels) can be referenced to the equatorial plane with radii of 2, 3, 4, 5, 6, at 7  $R_E$ .

The static model can be averaged over any interval during the CRRES lifetime. For the whole of the CRRES lifetime the model represents a fairly active time period during solar maximum. The use of the static model forms the basis for dynamic modeling by binning the static model according to various magnetic disturbance indices.

### **3.3.4 AFPL Summary Database for IMS-HI**

In addition to the internal database development activity on this contract we have worked with Phillips Laboratory to develop software for generating a model radiation belt database for IMS-HI. Several examples of the IMS-HI summary data plots for L-shell versus orbit during the CRRES mission are shown in Figures 14 to 17. These data, for the first time, show the dynamics of medium energy ions in the radiation belts during the active and quiet periods of the CRRES mission.

## **3.4 Magnetic Storm Dynamics**

The 26 August 1990 and 24 March 1991 Magnetic storms were investigated using the IMS-HI and SEP instruments on the CRRES satellite. These storms show considerable variation and variation with other events (e.g. Gloeckler et al., 1985 and McEntire et al., 1985). By understanding the injection, acceleration, and transport within the radiation belts the assumptions

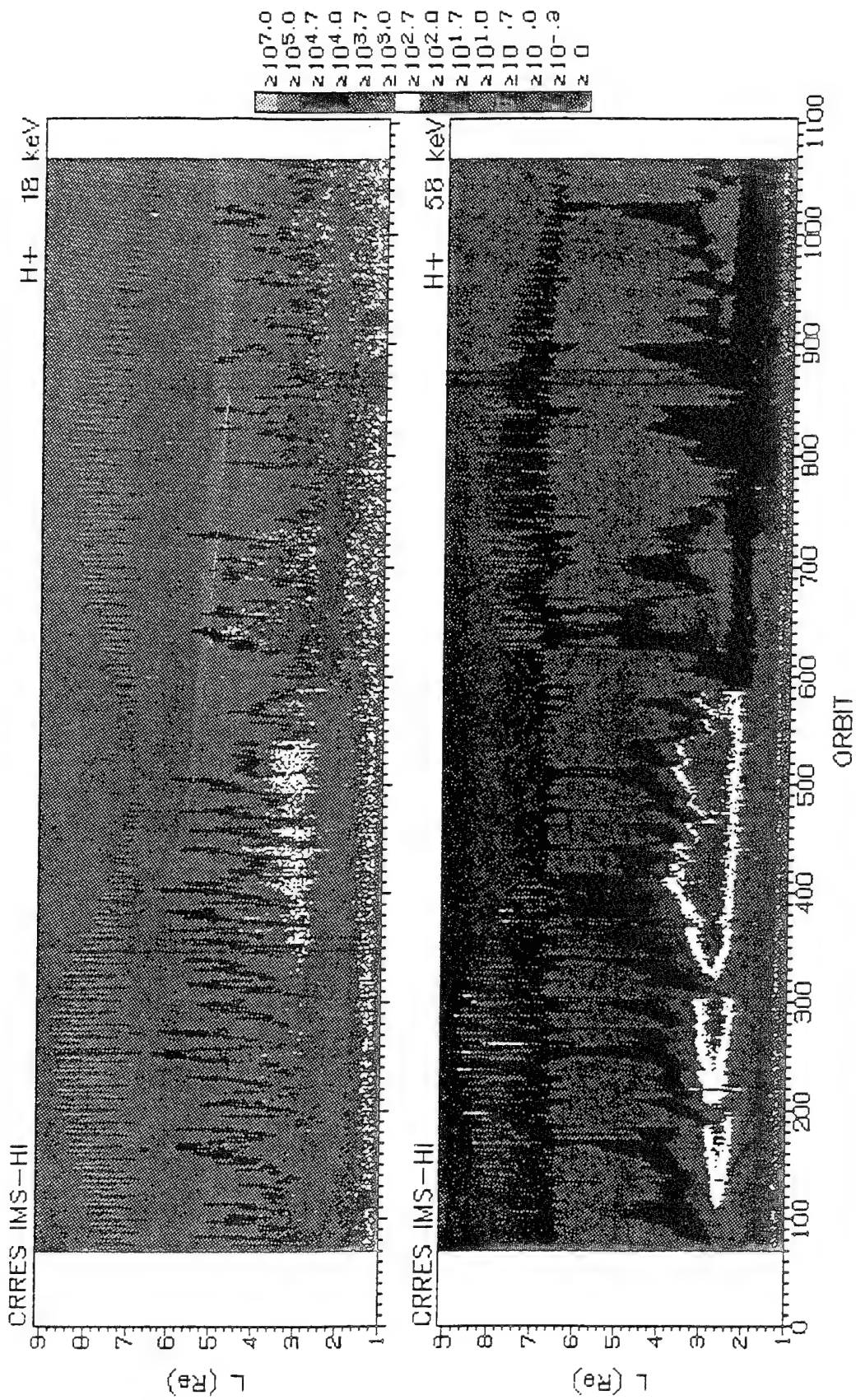


Figure 14 Spectrogram of H<sup>+</sup> Flux from IMS-HI vs. L-shell for CRRES Mission

CRRES IMS-HI

O++ 90 keV

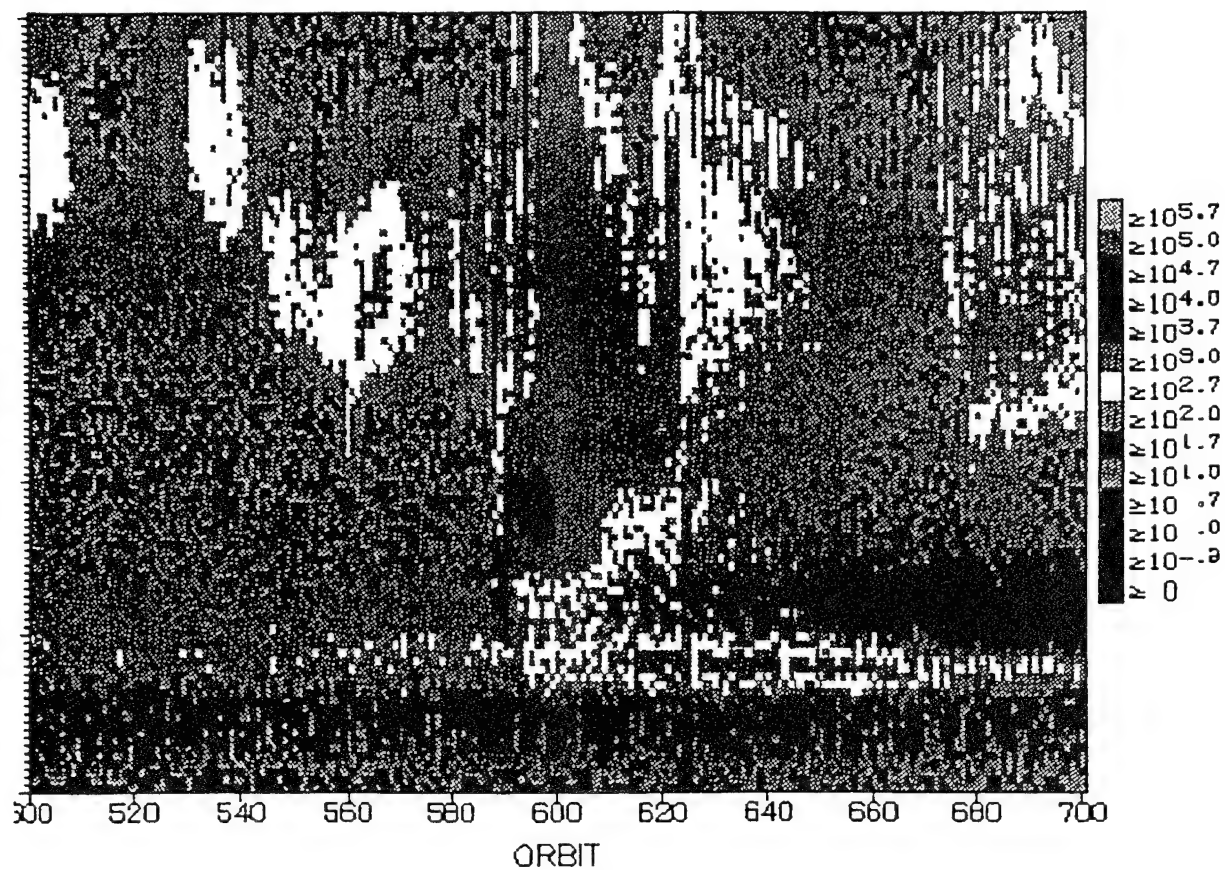


Figure 15 Spectrogram of O++ Flux from IMS-HI versus L-shell

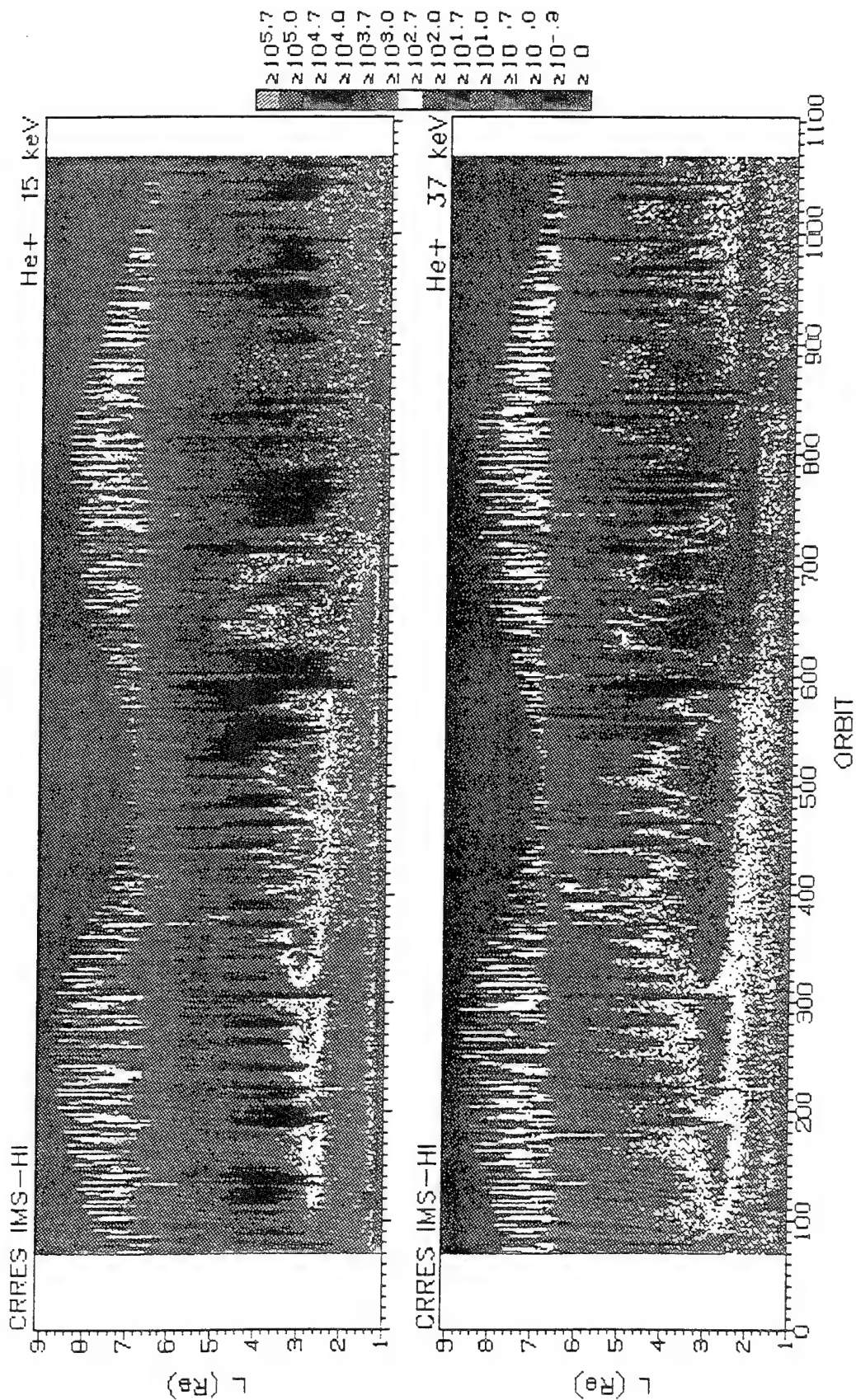


Figure 16 Spectrogram of He<sup>+</sup> Flux from IMS-HI vs. L-shell for CRRES Mission



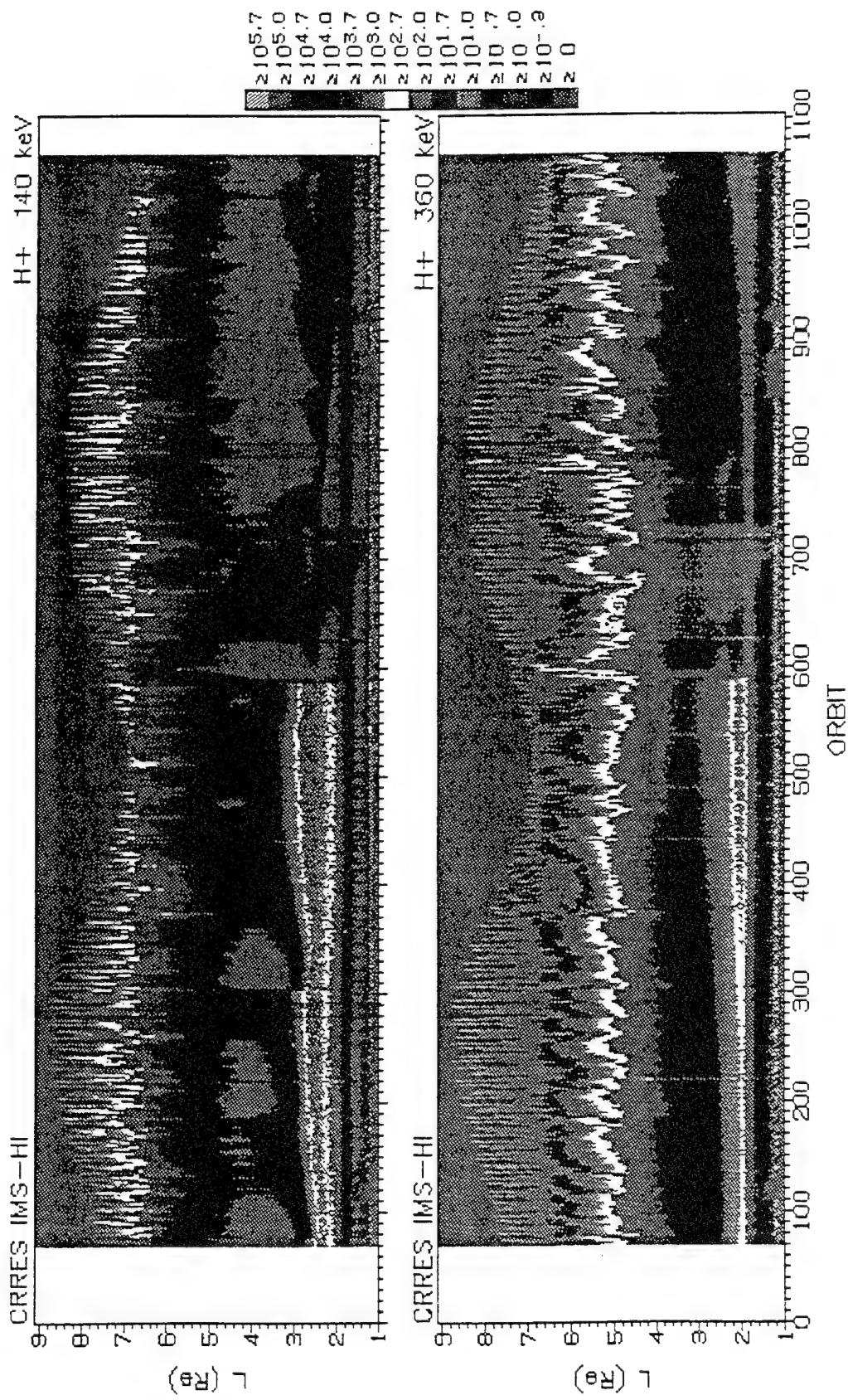


Figure 17 Spectrogram of H<sup>+</sup> Flux from IMS-HI vs. L-shell for CRRES Mission

for modeling algorithms can be improved. The best models are usually based on parameters which have good physical significance.

For the 26 August 1990 magnetic storm the Kp reached 7-. At the time of the sudden commencement CRRES was near apogee in the dawn sector. For 24 March 1991 the Kp reached 9-. At the time of the sudden commencement CRRES was in the slot region at  $L \sim 2.5$  at about 0300 hr UT.

### 3.4.1 Wave Particle Interactions

Of particular interest is the sensitivity of the differential ion flux measurements of the IMS-HI instrument to waves. In Figure 18, a 6 minute period ULF wave, that is observed prior to the sudden commencement, is also observed in the 18 keV proton channel. The resonant interaction is such that at 56 keV no interaction is observed. The small scale fluctuations in the 18 keV and 56 keV channels are associated with spin modulation. At the time of the sudden commencement the magnetic flux density is increased due to the magnetic compression and the particle flux is likewise increased in accordance with Louisville's theorem. Another association of  $B_z$  wave activity with 18 keV protons during this storm event is shown in Figure 19. Wave-particle interaction observed with the CRRES energetic electron and electric field experiments are currently being investigated by Dr. W.L. Imhof and will be reported in a later publication.

### 3.4.2 Particle Transport and MeV Acceleration during a Sudden Commencement

Simultaneous injection/acceleration of  $>10$  MeV particles at  $L \sim 2.5$  with a sudden commencement is surprising and suggests that an unexpected acceleration mechanism is active in that region. Between 0342 and 0354 UT the particle instruments on the CRRES satellite measured impulsive bursts of  $>10$  MeV electrons, protons, and alphas in the slot region ( $2.1 < L < 2.5$ ) near the equator at 0300 hours MLT (Mullen et al., 1991; Vampola and Korth, 1992; Blake et al., 1992; and Voss et al., 1992a). The electron bursts (Figure 20) are consistent with drift echoes of about 15 MeV electrons while the proton groups are consistent with drift echoes of  $>20$  MeV protons. No medium energy  $18 \text{ keV} < E < 1.5 \text{ MeV}$  ion bursts were observed. However, in the IMS-HI neutral detector, which is also sensitive to protons with  $E > 50 \text{ MeV}$ , a particle burst was observed 0.5 minutes before the electron peak (Figure 21). The electrons

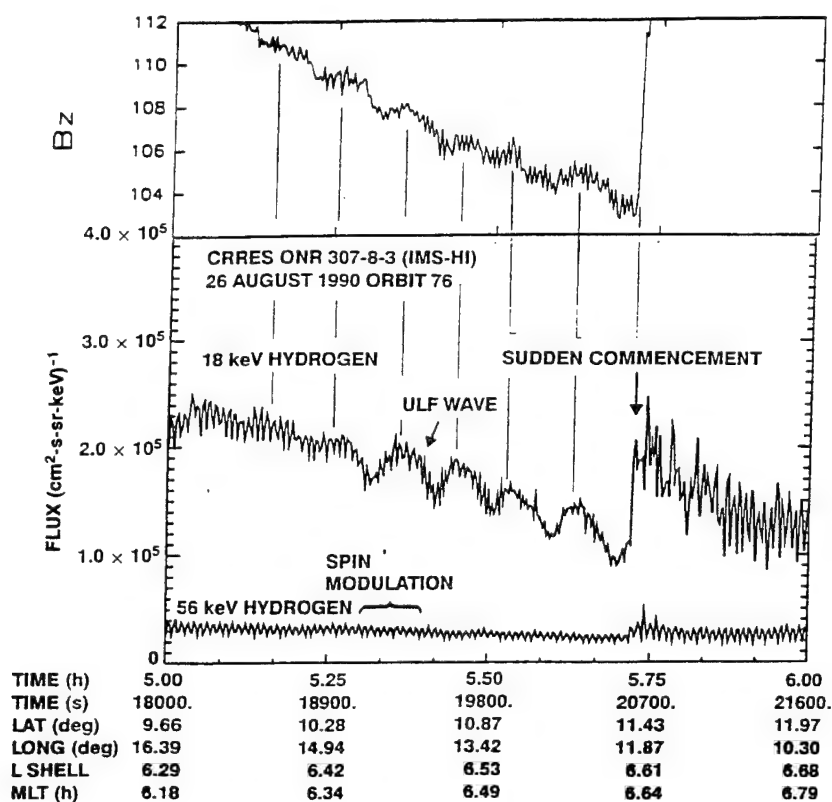


Figure 18 The IMS-HI instrument differential ion flux for 18 keV and 56 keV H<sup>+</sup> the ULF wave is observed in the magnetometer data (upper panel) and 18 keV proton (lower panel) channel

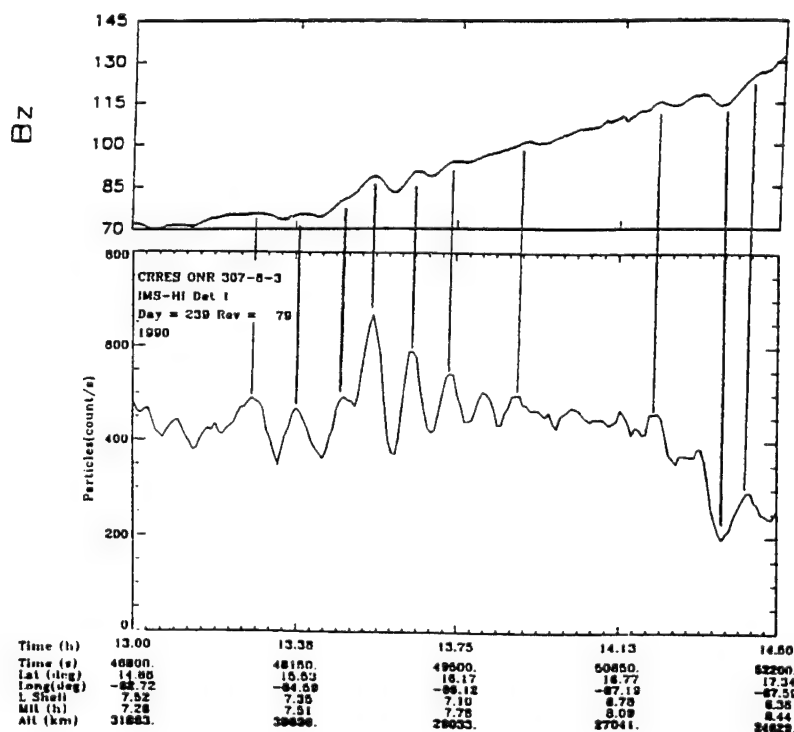


Figure 19 The association of B<sub>z</sub> activity with 18 keV protons



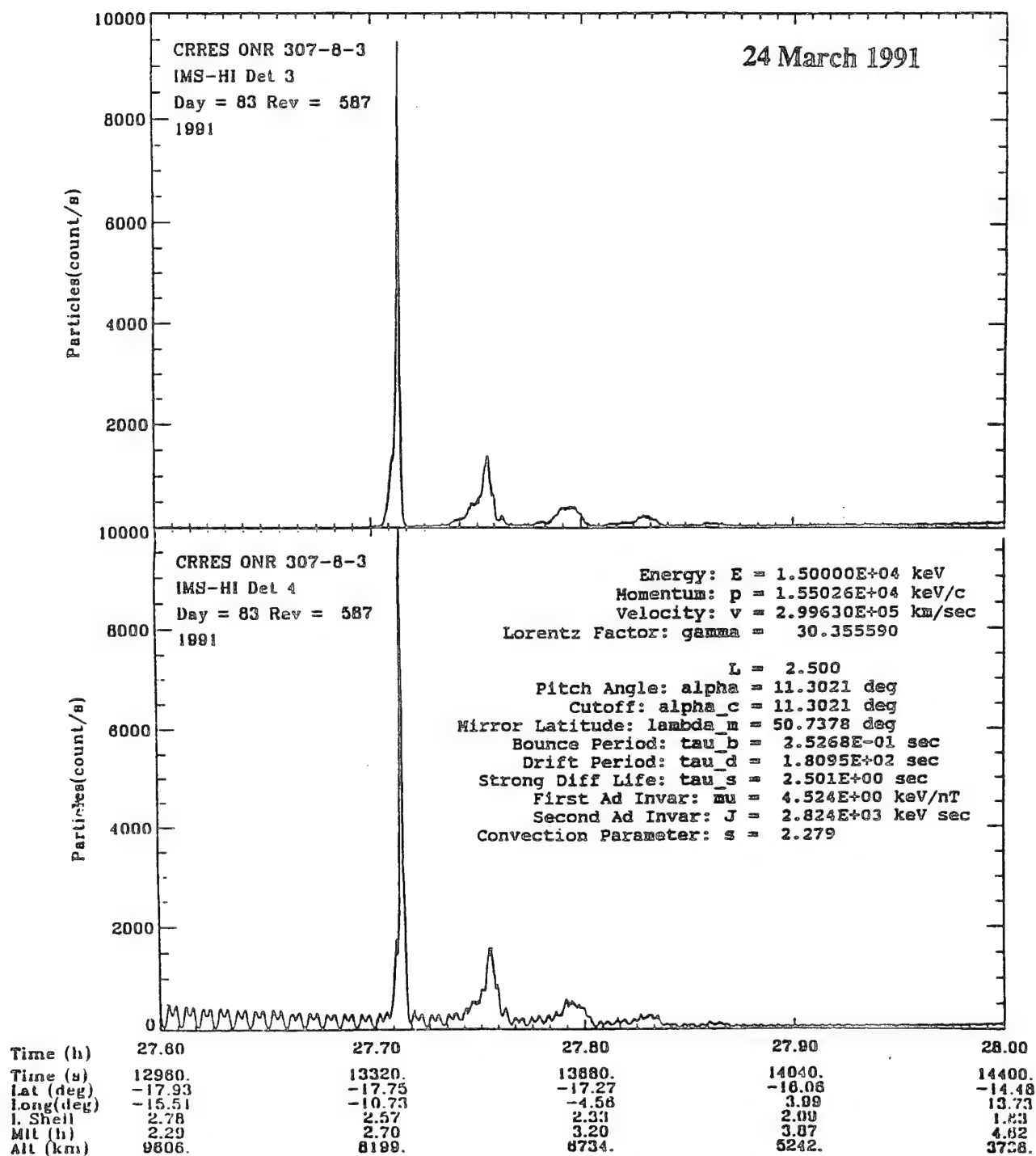


Figure 20 Strong injected electron flux observed by IMS-HI during the 24 March 1991 magnetic storm onset

# ONR-307 IMS-HI

Rev 587, Detector 7

24 March 1991

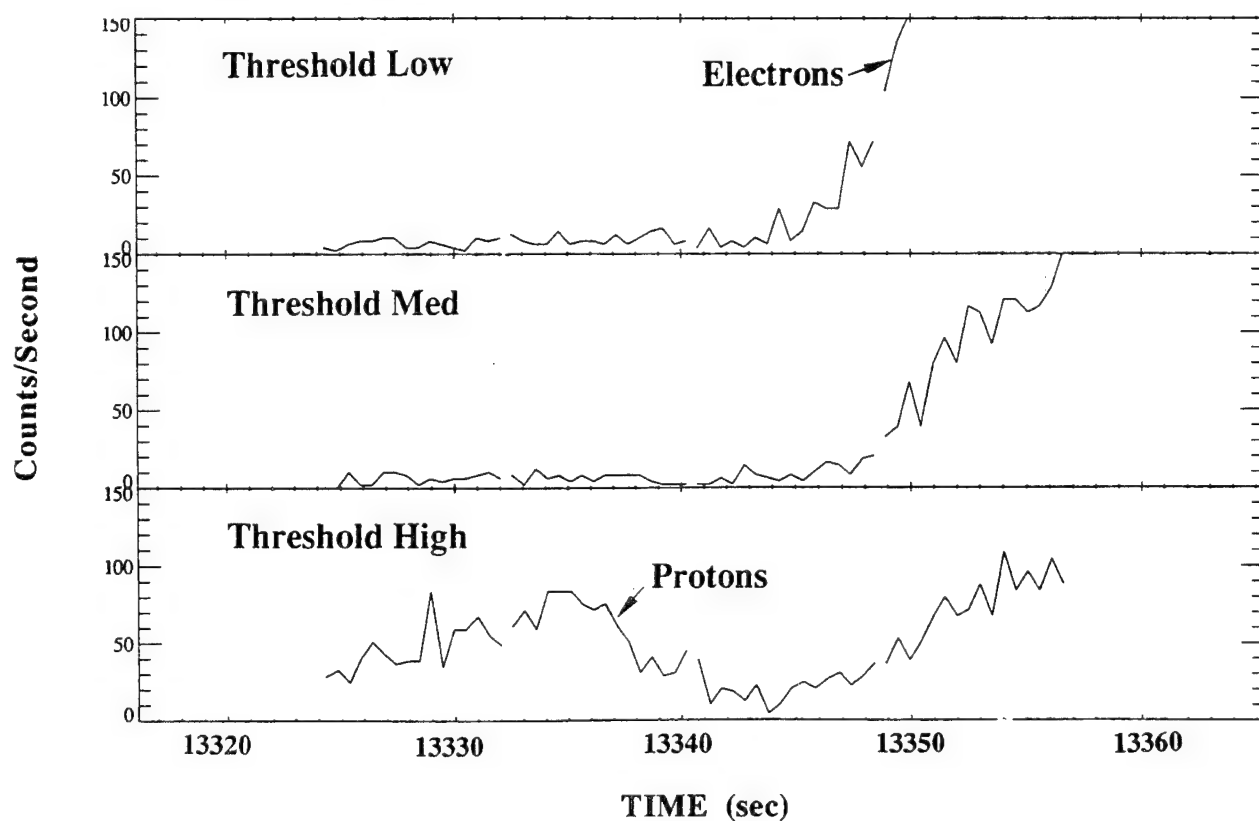


Figure 21 Greater than 50 MeV proton peak observed in the neutral detector about 35s before the large electron peak.

observed with the SEP instrument on CRRES for orbits before (586), during (587), and after (588) the magnetic storm SC are shown in Figure 22.

During the burst event the SEP instrument scanned through 7 logic modes (Figure 23) to measure the electron, proton, and alpha flux and energy spectra. In Figure 23 the lower panel shows the scintillator response of the anticoincidence shield on the SEP telescope. The voltage threshold of this scintillator is constant and is set at a low energy ( $\sim 100$  keV) so that it is very sensitive to penetrating radiation. The two largest peaks represent the first two electron bursts shown in Figure 23. The initial precursor at 13315 sec, which also appears in the E detector is thought to be  $E > 100$  MeV protons. The spin modulation may account for the apparent drop in flux after the precursor peak and before the low energy 20 MeV peak. The data indicate that the 100 MeV protons arrive at the detector first followed by the lower energy but higher fluxes of 25 MeV protons. The strong 15 MeV electron peak occurs about 30 seconds after the 25 MeV proton peak. This information can be used to infer some of the characteristics of the injection region.

### 3.4.3 Simulation of Radiation Belt Electron Bursts

The characteristics of the electron bursts of March 24 are: 1.) The peak is narrow in time (about 5 seconds), 2.) Some dispersion is apparent in the subsequent echoes as the successive peaks have lower amplitudes but are broader in time, 3.) The electron energy is large enough to penetrate the walls of the IMS-HI and SEP detectors and, 4.) The drift period decreases slightly between successive peaks as the L value of the satellite decreases. This observation strongly suggests the energy of the injected electrons increases with decreasing L.

This information can be used to investigate the initial energy and pitch angle distribution, the size of the injection region, and the time interval during which injection/acceleration persisted. As a first approximation it was assumed that electrons were injected into the unperturbed geomagnetic field and followed the normal gradient and curvature drifts. Various initial particle distributions were used and the count rates which would have been observed at the CRRES satellite were tabulated for comparison with the experimental data. An example of the simulation is shown in Figure 24. The simulation was developed by Dr. M. Walt using a Monte Carlo technique. Initial particles were drawn from various specified distributions in initial longitude, energy, time of injection, and pitch angle. The drift motion of each particle was then tracked about the earth and tabulated each time it reached the satellite position. The resulting count rates then gave the expected signal the CRRES satellite would have been expected to observe.

Samples of these results are shown in the insert of Figure 24, the lower panel of Figure 25, and in Figures 26 and 27. The energy dispersion is investigated in Figure 24 where the initial

# ELECTRONS

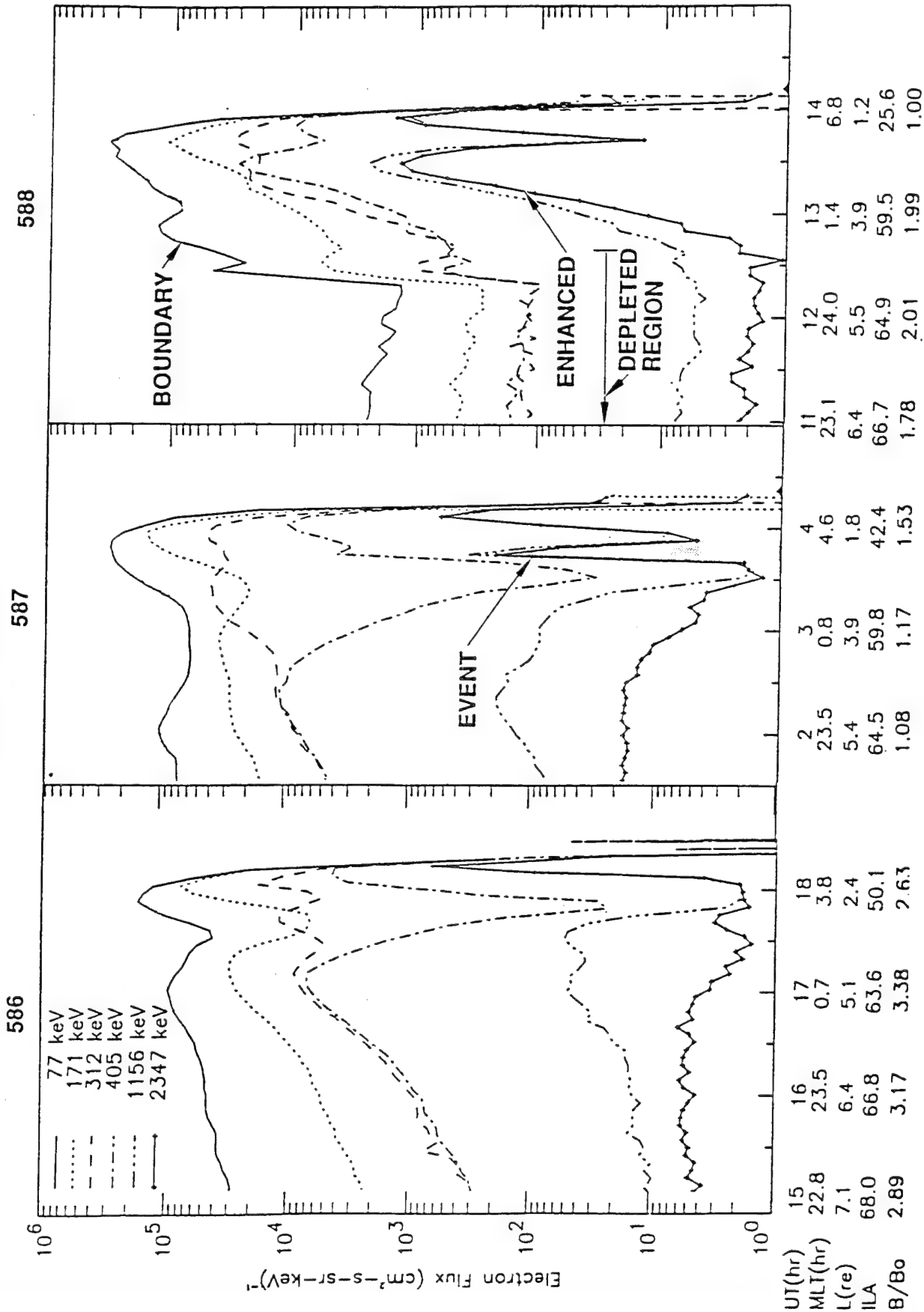


Figure 22 SEP electron data before and after 24 March 91 storm

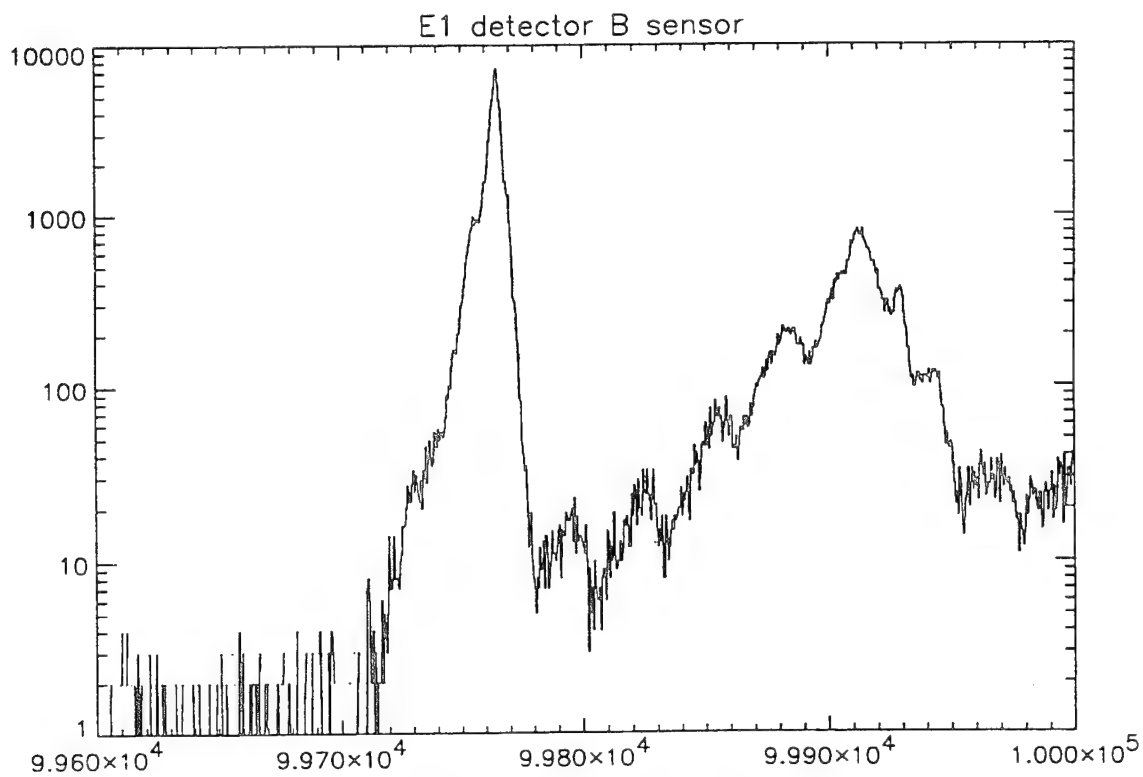
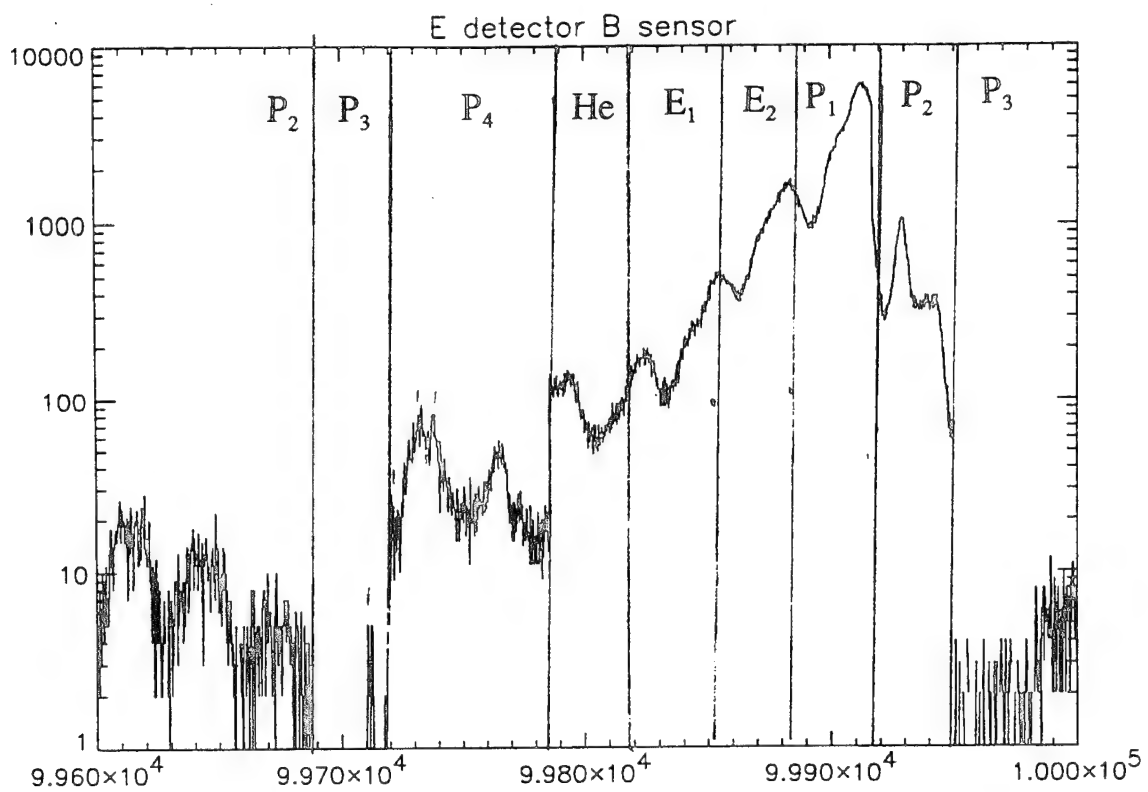


Figure 23 SEP instrument response to the slot region injection event of 24 March 1991. The upper panel is for the E detector and the lower panel for the Anti-scintillator shield

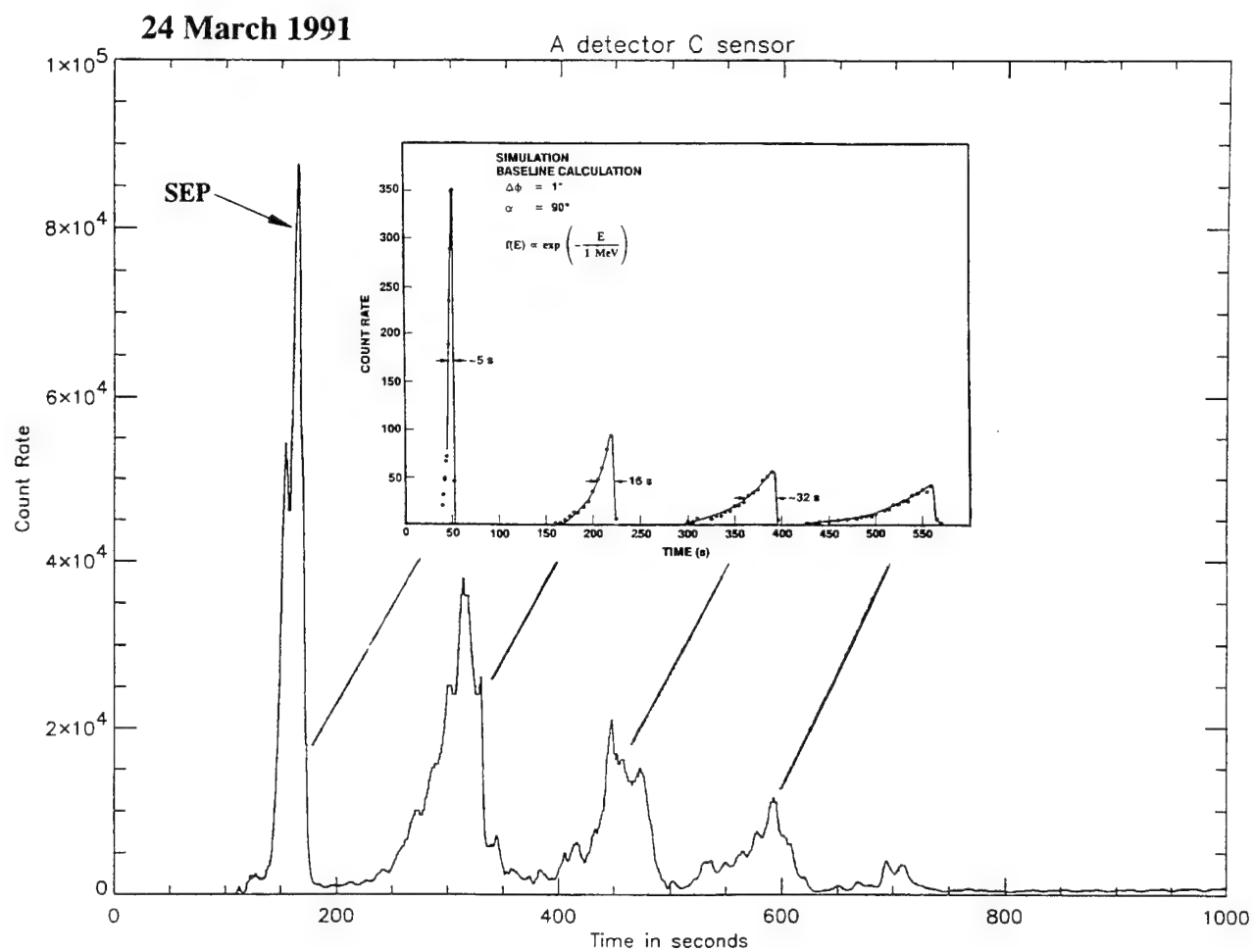


Figure 24 Monte Carlo simulation of the L=2.5 injection of energetic electrons (inset) and the SEP A detector

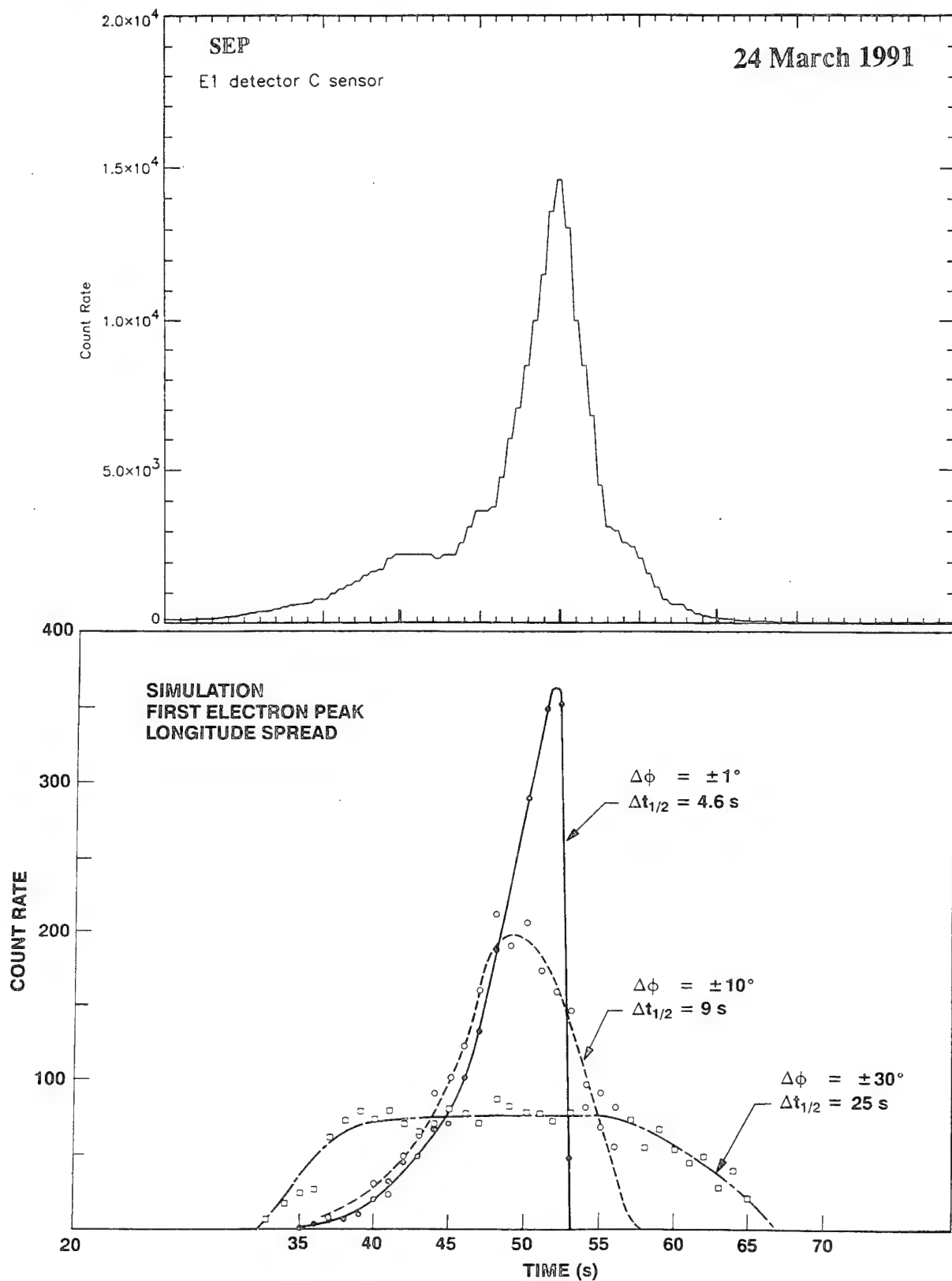


Figure 25 Simulation of the longitude interval of injection (lower panel) compared to the SEP E1 detector data.

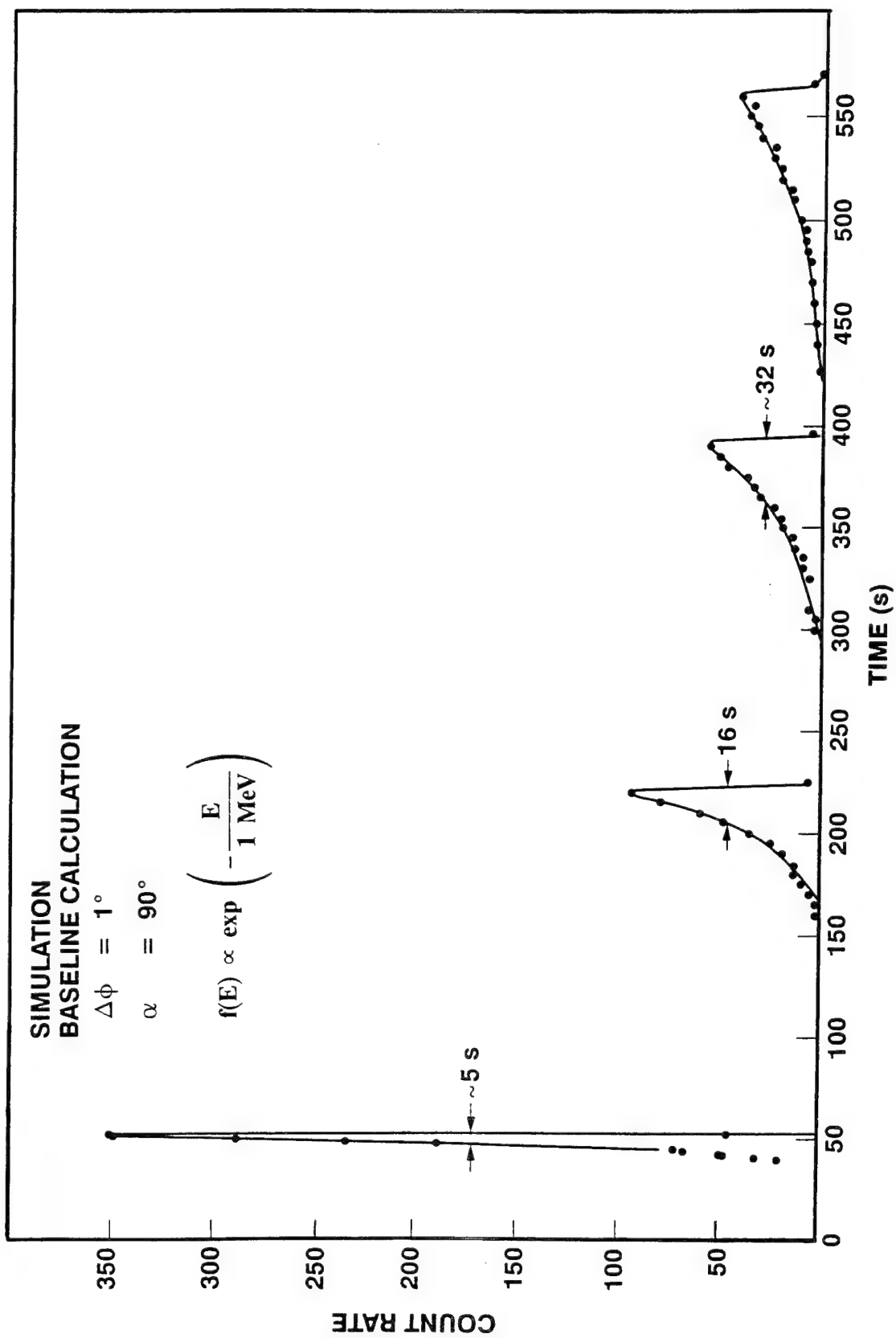


Figure 26 Pitch angle sensitivity simulation



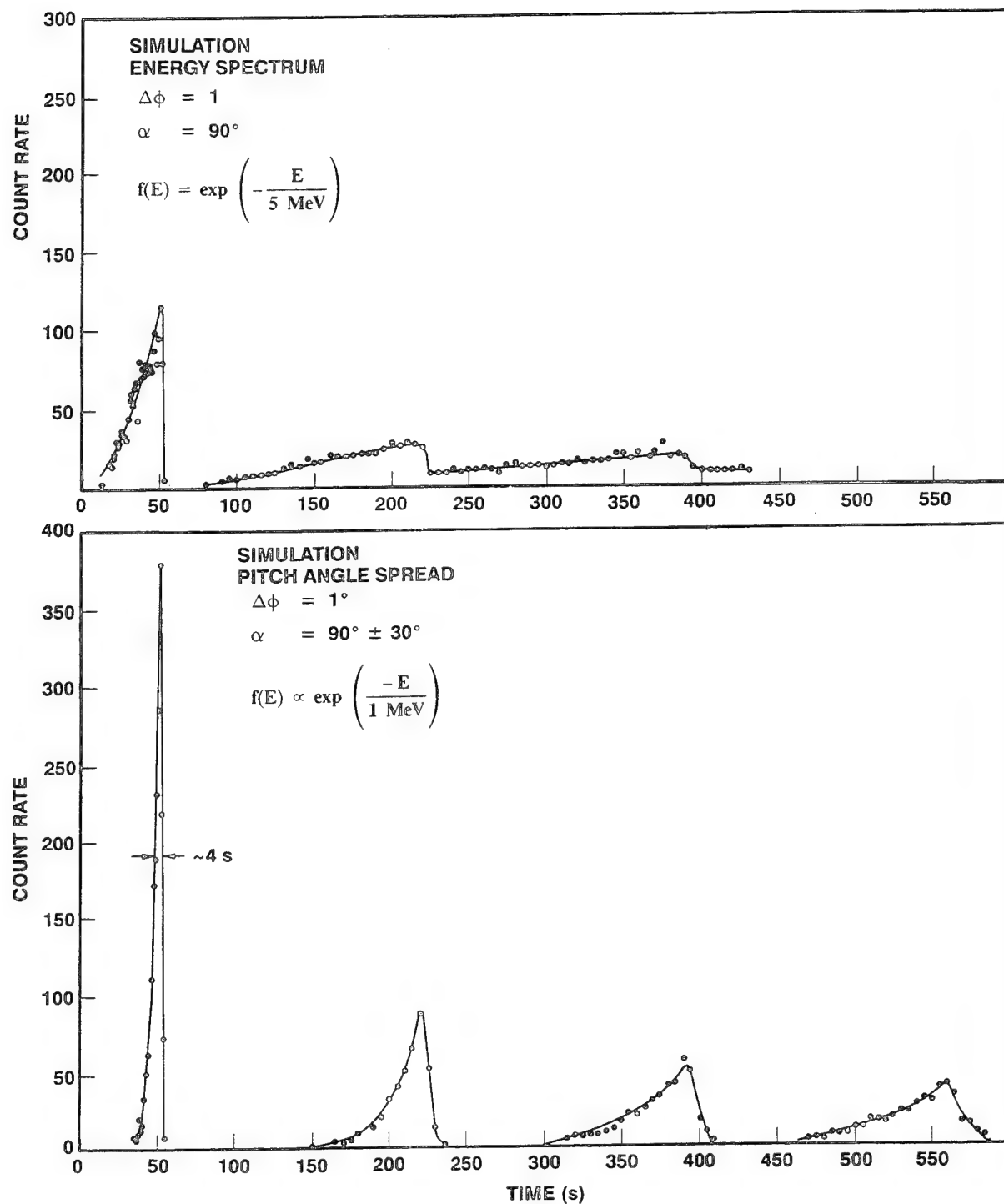


Figure 27 Simulation of the energy spectrum and pitch angle spread for injected electrons at L=2.5

energy distribution is represented by  $\exp(-E/2 \text{ MeV})$  with a threshold determined by the IMS-HI detector sensitivity at 10 MeV. Particles were injected simultaneously in a narrow longitude interval ( $1^\circ$ ) and in equatorial orbits. The calculated dispersion under these conditions is due entirely to the initial energy spread and is similar to the observed values. Therefore, the initial energy distribution, must have been very narrow and if expressed as an exponential, had an e-folding energy of no more than 2 MeV. The echo peaks confirm this result as shown in Figure 27. If the e-folding energy is as large as 5 MeV, the second and third peak become unacceptably long due to the dispersion in drift period with energy.

Figure 25 explores the longitude interval of injection and compares the simulation results with the width of the initial electron peak. It is apparent that with these assumptions the injection region can have a longitude spread of no more than about 10 degrees. Otherwise the first peak would have had too long a time duration.

The shape of the electron pulses are not sensitive to the pitch angle distribution as shown in Figure 26. In Figure 27 the initial flux was assumed to be spread uniformly in equatorial pitch angle between 60 and 90 degrees. The simulated electron bursts are not significantly different from those with the flux concentrated at 90 degrees.

### **3.5 Radiation Belt Acceleration and Transport**

Before the CRRES measurements, the very strong response of the radiation belts at  $L=2.5$  to a sudden commencement (SC) was not expected. The CRRES data suggest that the radiation belt fluxes and energies are affected within minutes of initiation of the SC magnetic shock in the magnetosphere. To properly model and predict the radiation belt effects the algorithms must take into consideration the recent or expected magnetic activity factors.

In this section an initial attempt is made to explain the CRRES data for the surprisingly rapid injection of MeV particles in the inner radiation belt. Various mechanisms have been suggested such as solar MeV particle penetration, inner belt expansion during the storm, electric-field drift accelerations (Pfitzer, 1992), and direct magnetic compression (Voss, 1992d) as discussed in this report. The important requirement of the theory is that it should explain the following key data: 1) The narrow 5 second pulse width of the electron bursts indicate a narrow longitude spread and a short time interval of injection. 2) The preferential acceleration of only MeV energy particles. 3) The greater injected particle energy at lower L shells.

## TSYGANENKO MODEL

FIELD LINE TRACE (TSYGANENKO) 1987 SHORT MODEL

TIME=14:38:51, DATE= 8-JUN-92

THE X,Y,Z COORDINATE SYSTEM IS: MAGNETOSPHERIC

KP= > 5 , EPOCH(Y:M:D:H:M:S)=91: 3:24: 3:42: 0:

FIELD LINE IN (X,Z) PLANE, DIPOLE TILT= -9.1 DEG.

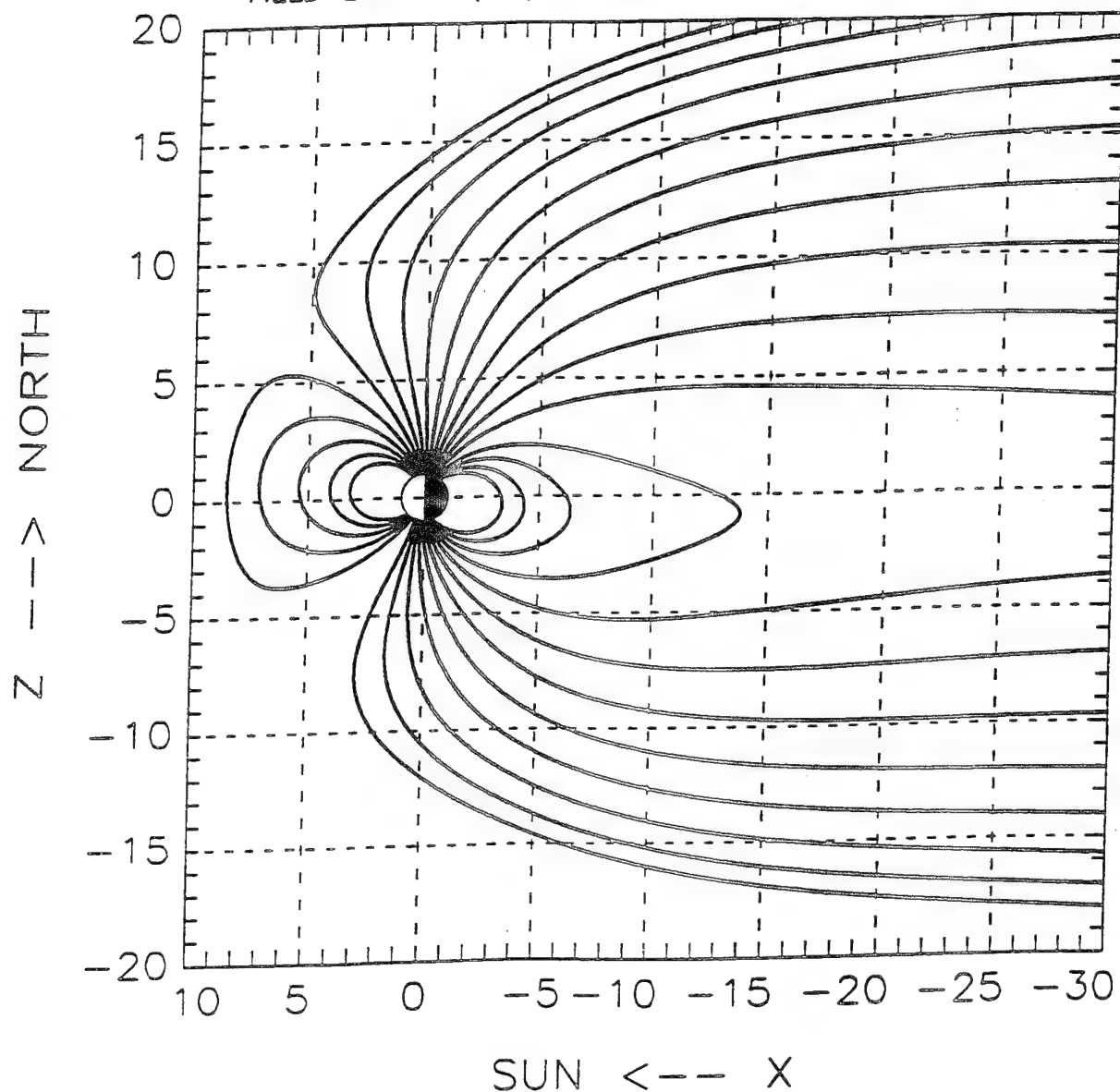


Figure 28 Tsyganenko model for  $K_p > 5$  during the CRRES injection event

4) The apparent dusk-noon location of the injection region (or the relative delay between the proton and electron peaks). 5) The simultaneous injection/acceleration of MeV electrons, protons, and alpha particles. 6) The nearly simultaneous injection of particles with the magnetic compression (150  $\gamma$  at CRRES) during the SC.

The magnetic field configuration at the time of the SC is shown in the field line traces of Figure 28, using the Tsyganenko (1987) short model for  $K_p > 5$ . The dipole tilt is  $-9.1$  degrees. For this case the standoff distance is about 8  $R_e$ , much greater than what is inferred during a SC shock impulse. To understand the impact of a shock on the magnetosphere and radiation belt a simple model was formulated using a dipole field and a parallel shock front. The parallel shock was constructed using an image dipole. The algorithms were also set up to vary the strength of the image dipole so that earth's dipole field would form a magnetosphere cavity (Hones, 1963). An example of the image dipole field line trace is shown in Figure 29 for a standoff distance of 5  $R_e$ .

The objective of this simple model is to represent the first order physics for explaining the acceleration and transport of particles within the radiation belts during a shock compression. The large 120 gamma field increase observed at the CRRES location at 03 MLT (Figure 30) is thought to be the result of the magnetosphere compressing, i.e. the sum of the earth's dipole and image dipole in our simple model. On the front side of the magnetosphere the compression is much greater because that region is much closer to the image dipole ( $r^{-3}$  dependence). The drifting of particles along constant B results in the rapid transport of high energy particles to lower L shells and the violation of the third invariant. Following Parker (1960) the perturbation fields of an image dipole are:

$$B'_x = 3B_o \left(\frac{a}{r}\right)^3 \cdot z \left(\frac{1}{r^2}\right)$$

$$B'_y = 3B_o \left(\frac{a}{r}\right)^3 \cdot z (y + 2L) \left(\frac{1}{r^2}\right)$$

$$B'_z = B_o \left(\frac{a}{r}\right)^3 \cdot \left(\frac{3z^2}{r^2} - 1\right)$$

where  $r = x^2 + (y + 2L)^2 + z^2$  and  $2L$  is the dipole separation distance. For small changes in the magnetosphere the drift orbit of particles may be represented as circles that are offset from the center of the earth. During rapid compression the ring of particles are "frozen" to the field lines (Parker, 1963, Birmingham and Jones, 1968) and move in the anti solar direction as illustrated in Figure 31. However, because of the higher magnetic field strength on the day side during

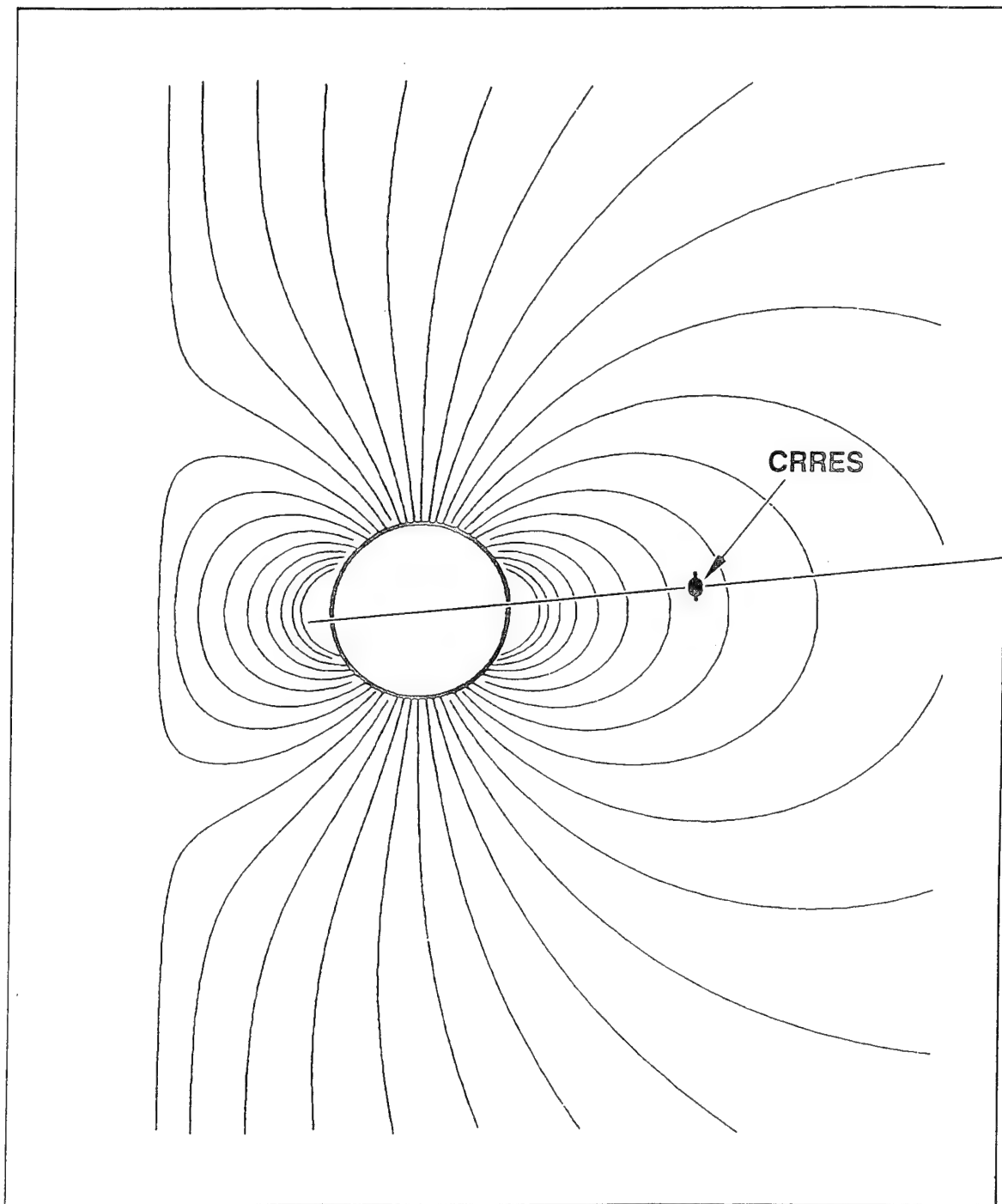


Figure 29 Field line trace of a dynamic magnetosphere using an image dipole

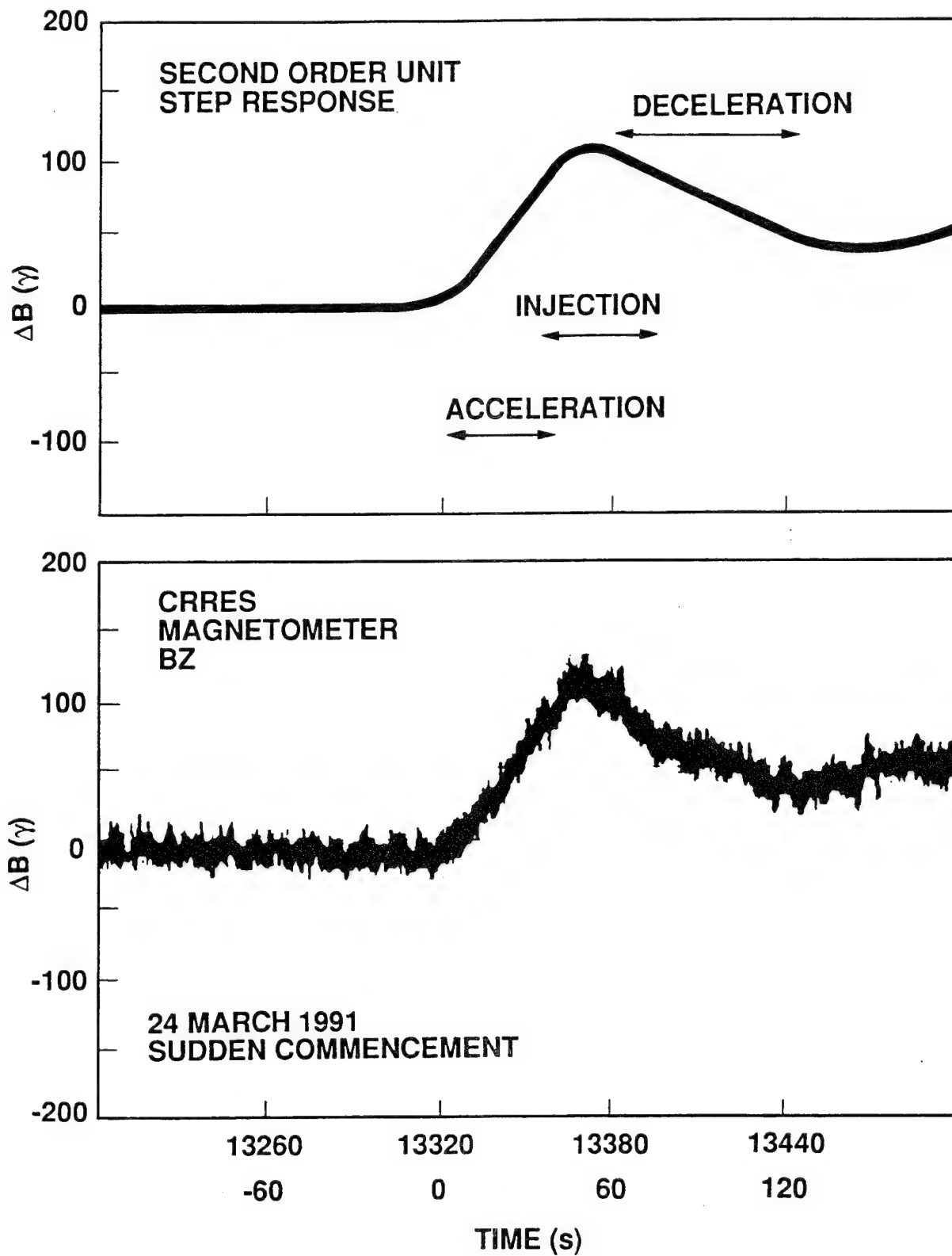


Figure 30 CRRES magnetic field data during the 25 March 1991 sudden commencement

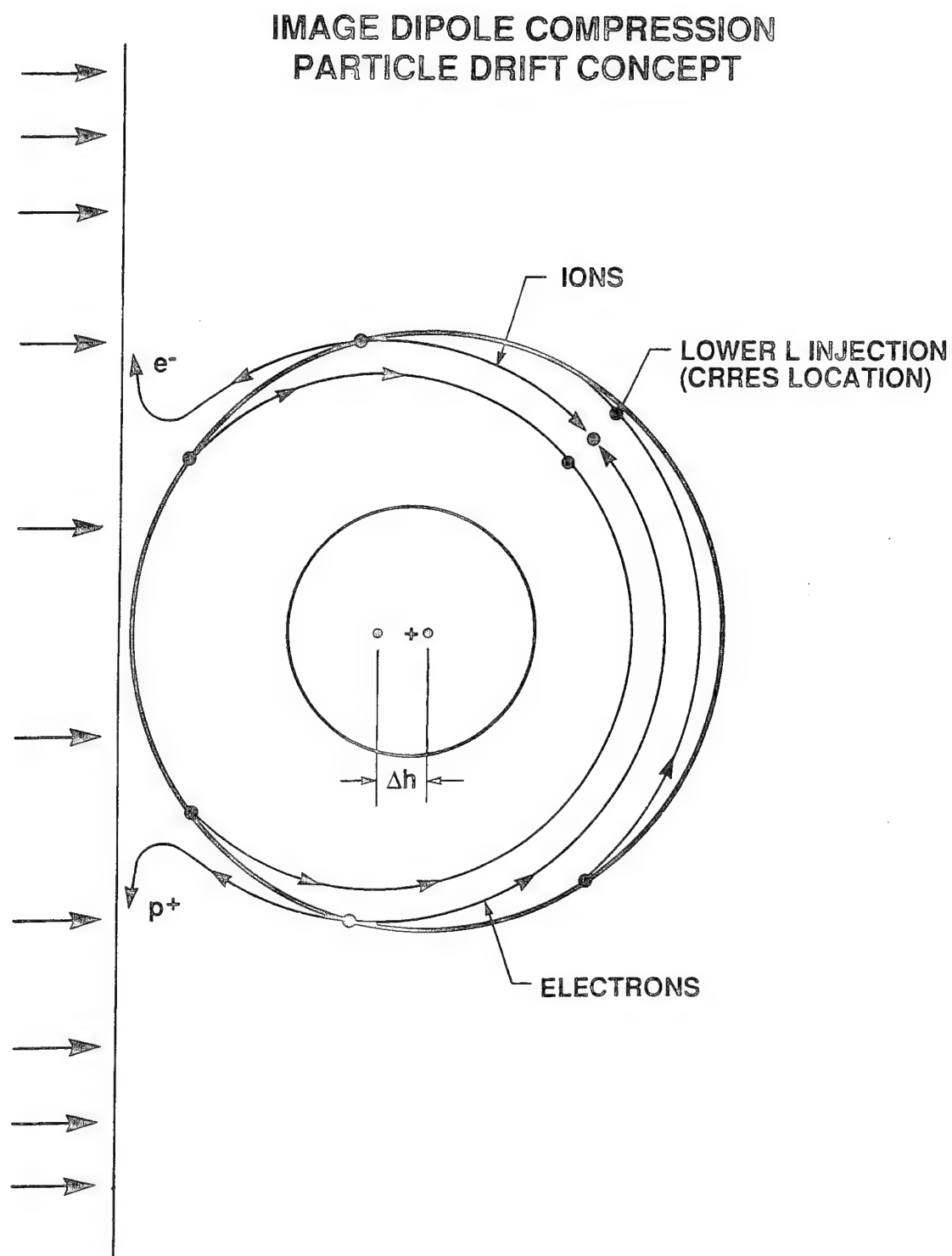


Figure 31 Approximate shift of particle drift orbits during a magnetic compression due to an image dipole

compression, the subsequent drift circles of undisturbed particles have centers in the solar direction from the earth's center.

Using the magnetic observations at the CRRES satellite ( 100 gamma increase) and the image dipole model the standoff distance varies with time as shown in Figure 32 for a minimum standoff distance of 3 Re. Although this low penetration of the magnetopause in L to 2.5 to 3.0 is surprising, much of the data can be explained with such an interpretation. After the initial penetration to low L (at 35 seconds) the magnetic field relaxes and the standoff distance backs off to L shells near 5. Following Henrick (1963) the magnetic line displacement during a compression event is given in Figure 33 assuming a final standoff distance of 3.0 and an initial standoff distance of 6.0. The resulting compression factor (an acceleration) is given in Figure 34. For a 6 Re particle that is compressed to 3 Re the acceleration would be about a factor of eight . A particle at 4 Re initially would move to 2.7 Re and have an acceleration of 4.5 times. On the night side the particles are only slightly affected in agreement with the data.

In this view the shock front compresses the frontside radiation belts to low L shells in about 30 seconds. The particles at noon ( $3 < L < 10$ ) are transported to L shells below 3 and are accelerated because of the increased magnetic flux from the adiabatic compression event (first invariant conserved). Using equation 2 for the dipole image model, the contours of constant B are shown in Figure 35 for standoff distances of 5, 3 and 2.5 Re. As the compression event proceeds the lower L shell contours shift towards the sunward direction, become tear shaped and then open up to give direct access from the magnetopause region to the radiation belt inner slot. For  $10 > \text{MeV}$  electrons, protons, and heavier ions the drift periods are short enough ( $< 3$  minutes) so that these particles can drift to the nightside before the magnetosphere is partially decompressed. A simplified diagram illustrating the important features of the magnetic compression and acceleration model is shown in Figure 36.



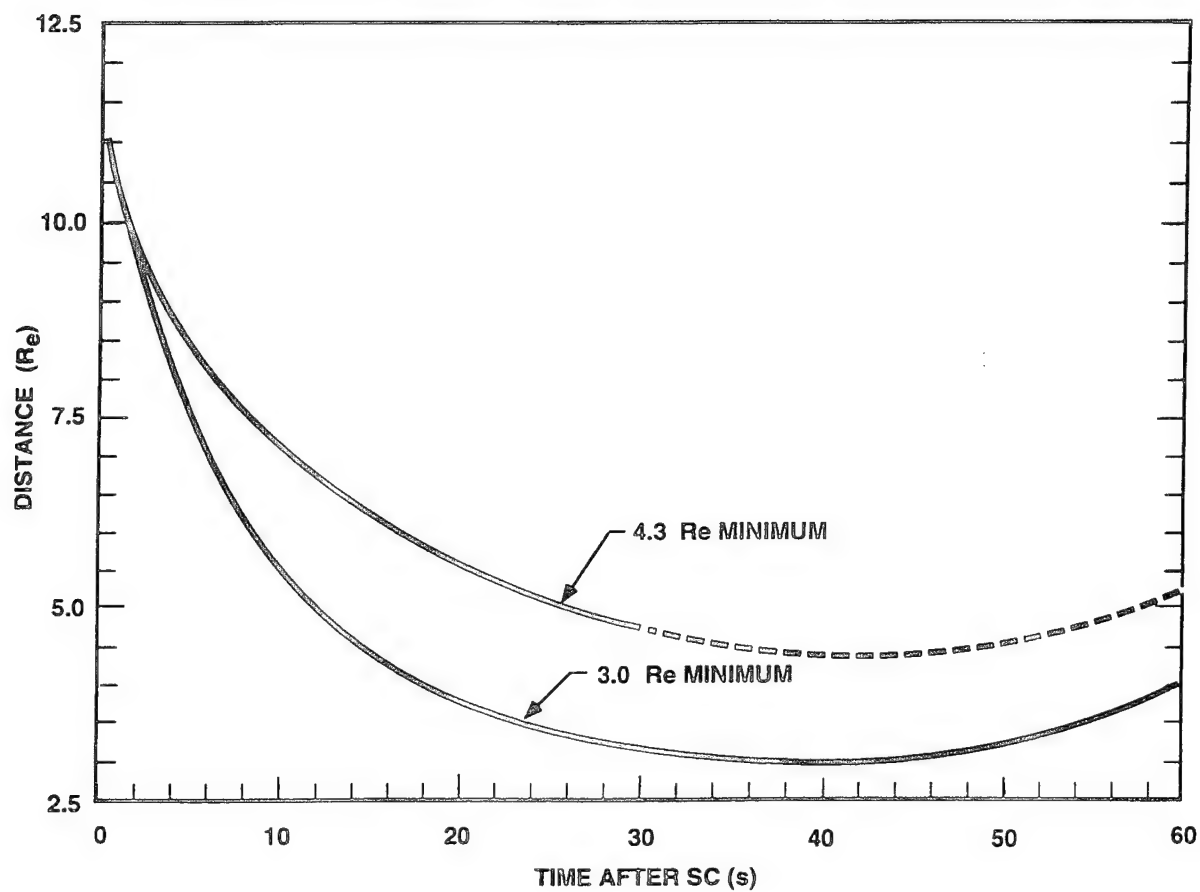


Figure 32 Standoff distance vs. time based on the image dipole compression of the magnetosphere

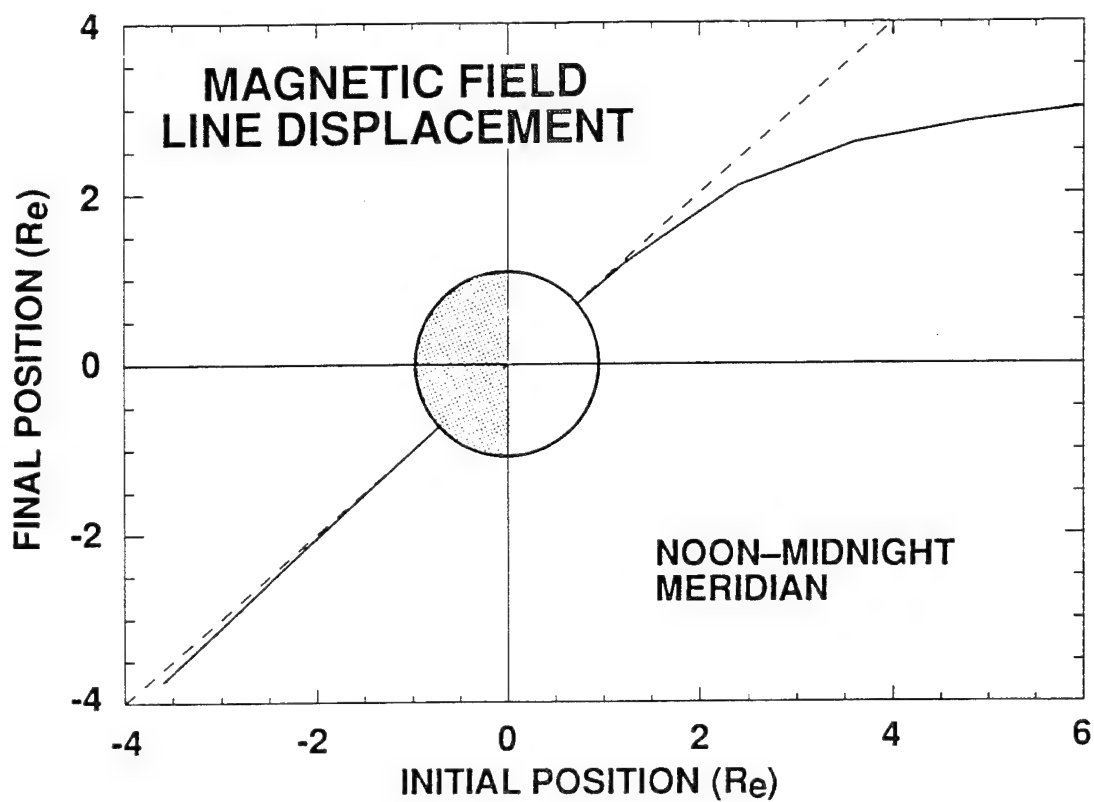


Figure 33 Magnetic field line displacement during a sudden commencement

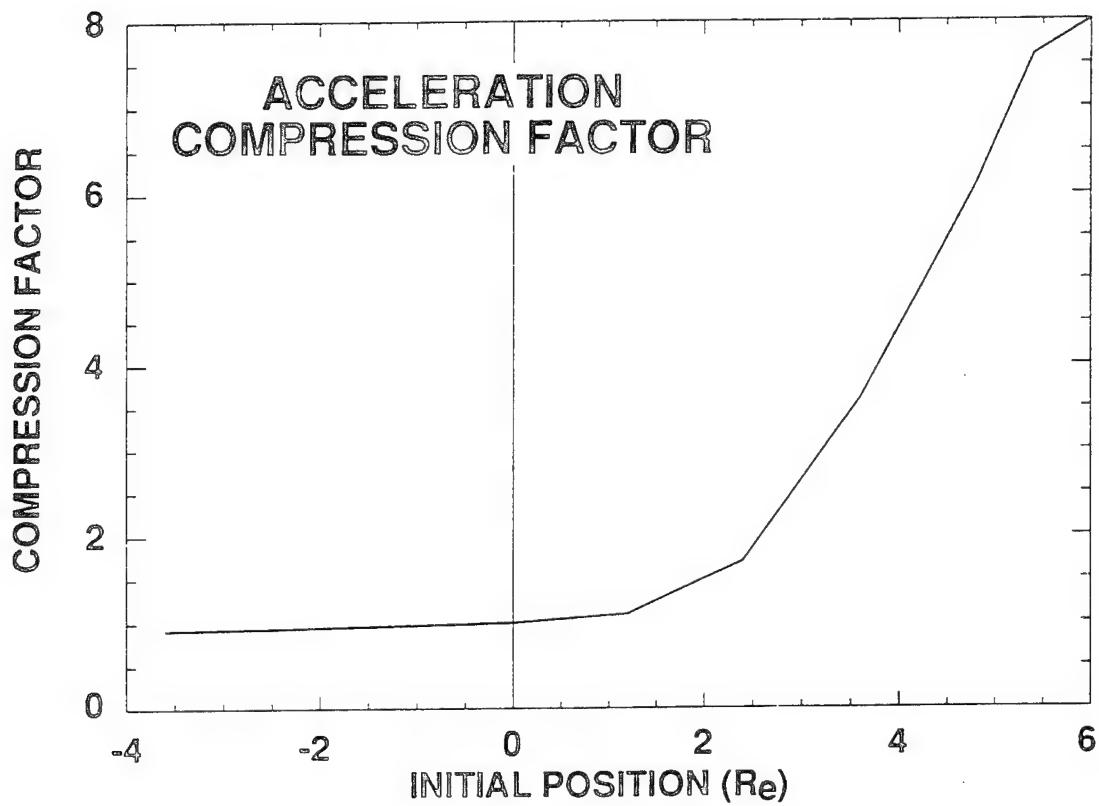


Figure 34 Magnetic field compression (acceleration) factor during a large sudden commencement

# PARTICLE DRIFT CONTOURS DURING INJECTION

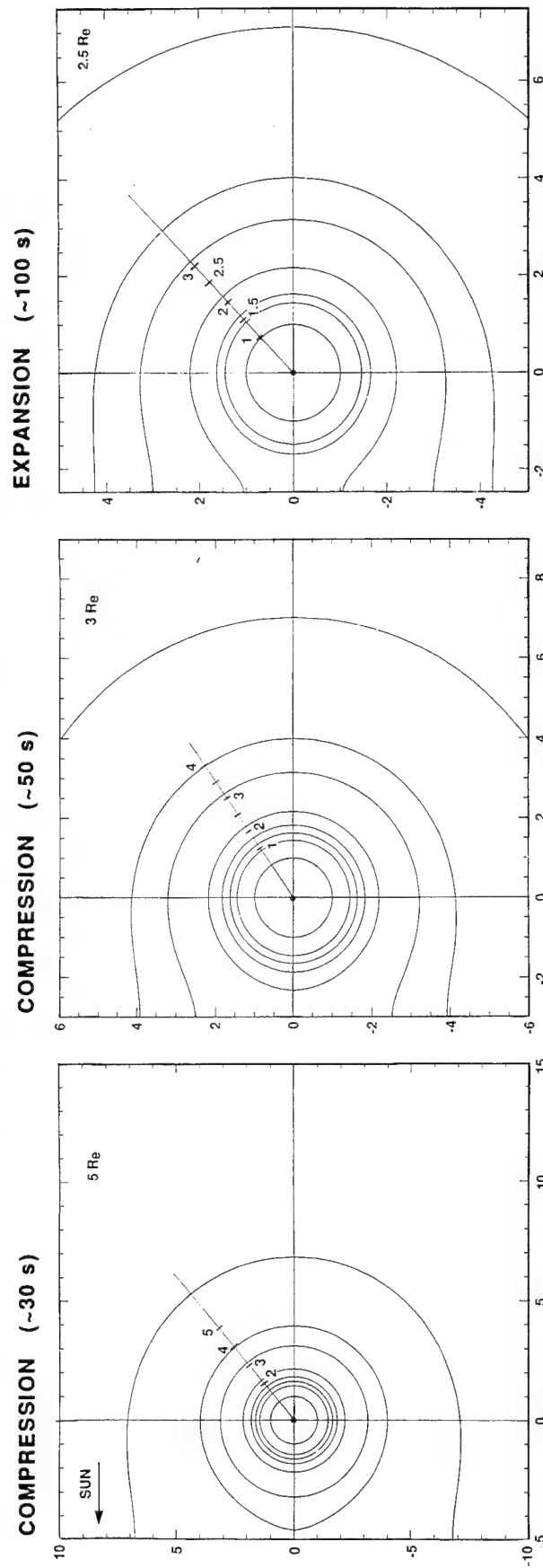


Figure 35 Constant B drift contours for particles during various stages of the compression event

# RADIATION BELT ACCELERATION-DIRECT ACCESS MODEL

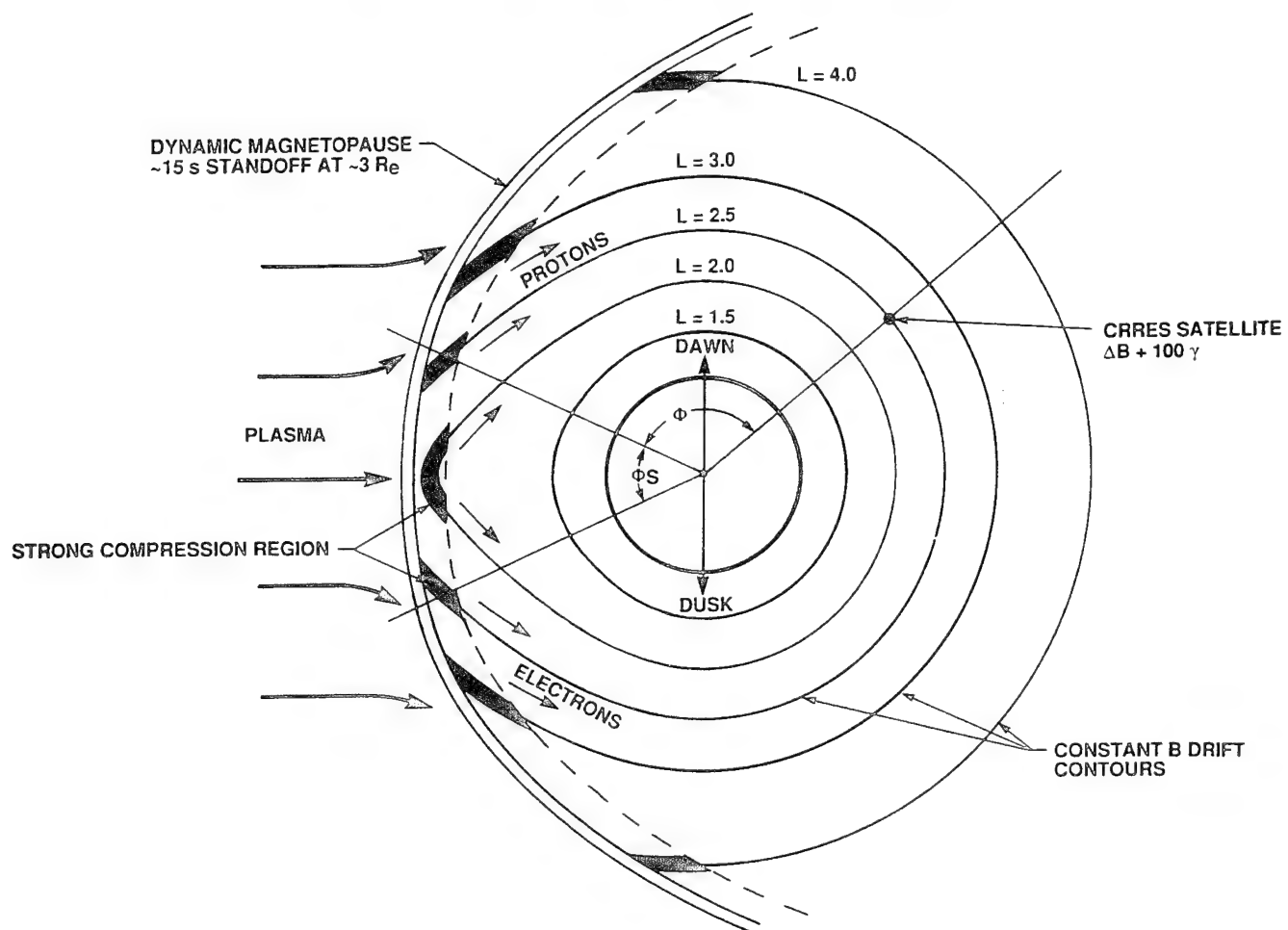


Figure 36 Model of acceleration and injection of  $> 10$  MeV electrons, protons, and alphas into the radiation belt slot region during a sudden commencement

CRRES IMS-HI (ONR 307-8-3) Rev 587 Day 82

He<sup>+</sup>

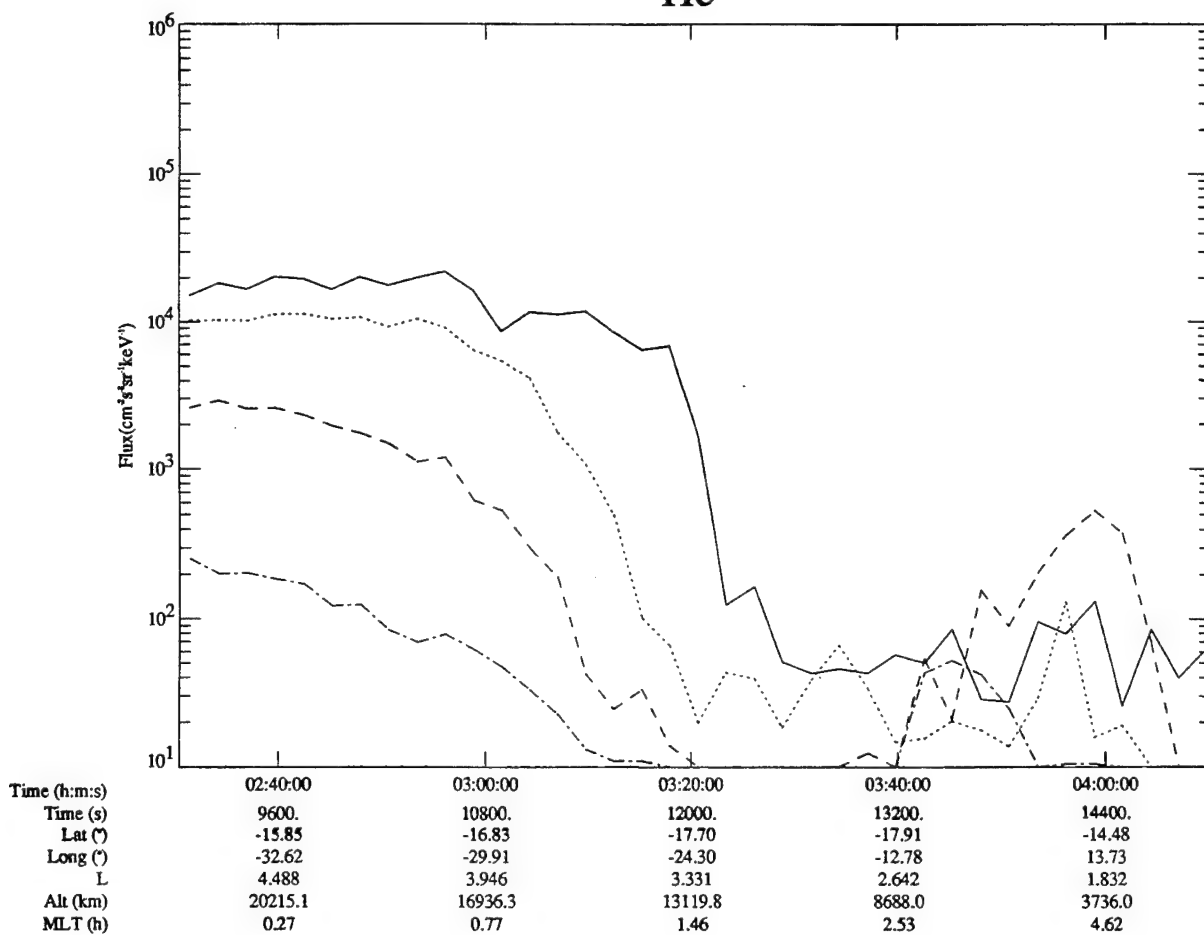


Figure 37 Inner edge ring current ion flux

# CRRES IMS-HI (ONR 307-8-3) Rev 590 Day 83

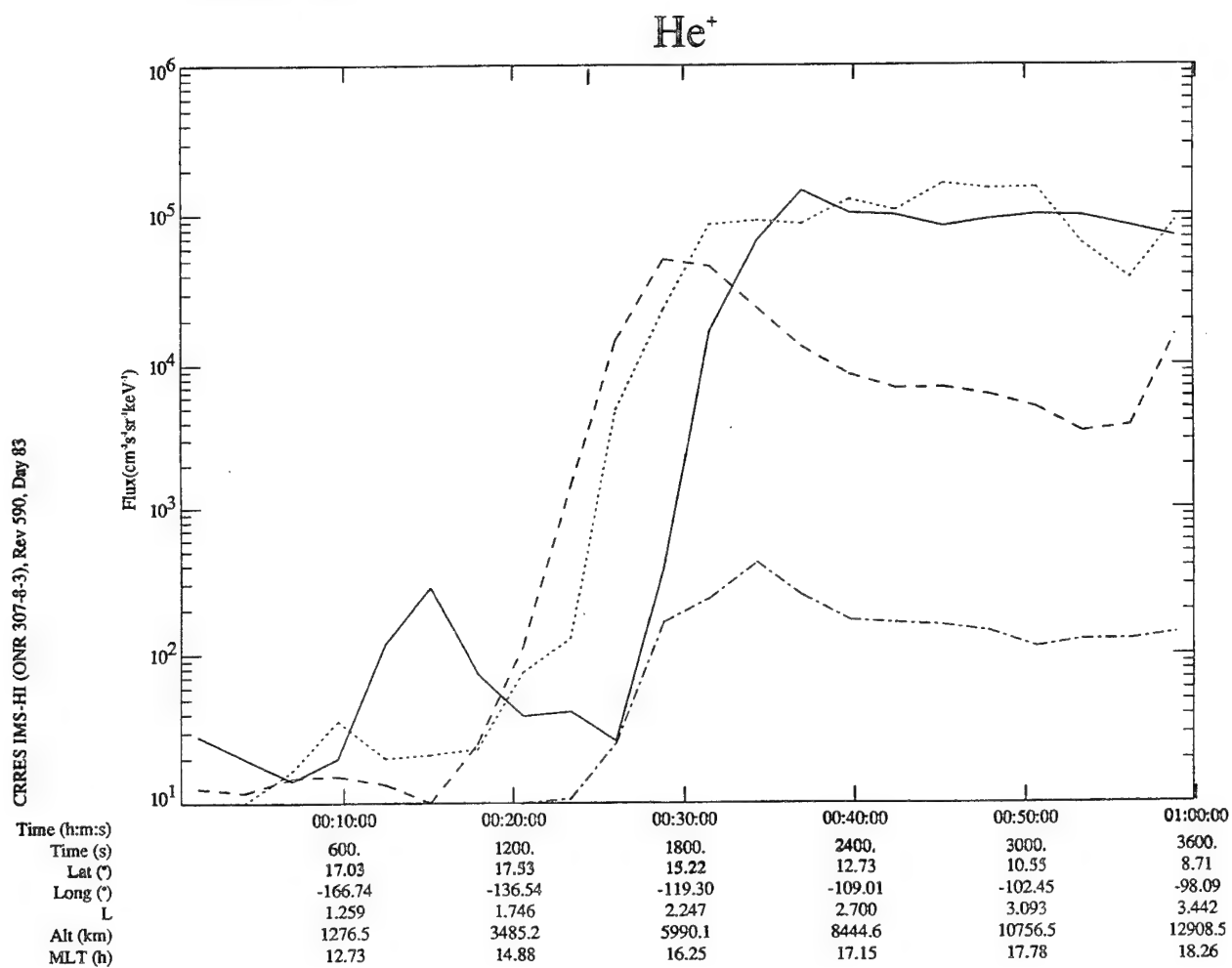
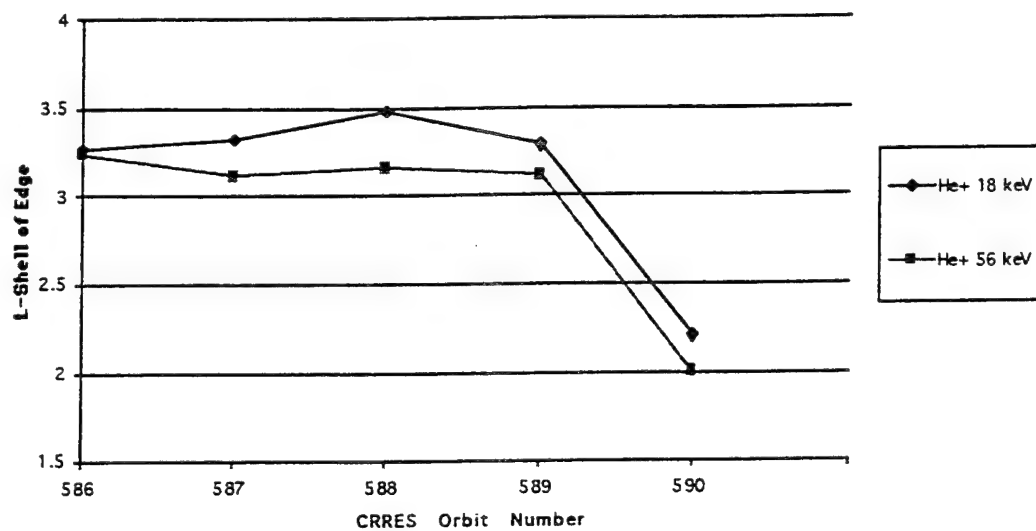


Figure 38 Inner edge ring current ion flux

L-Shell of He+ Ring Current Edge vs. Orbit Number  
(Toward Apogee)



L-Shell of Ring Current Edge vs. Orbit Number  
(Toward Perigee)

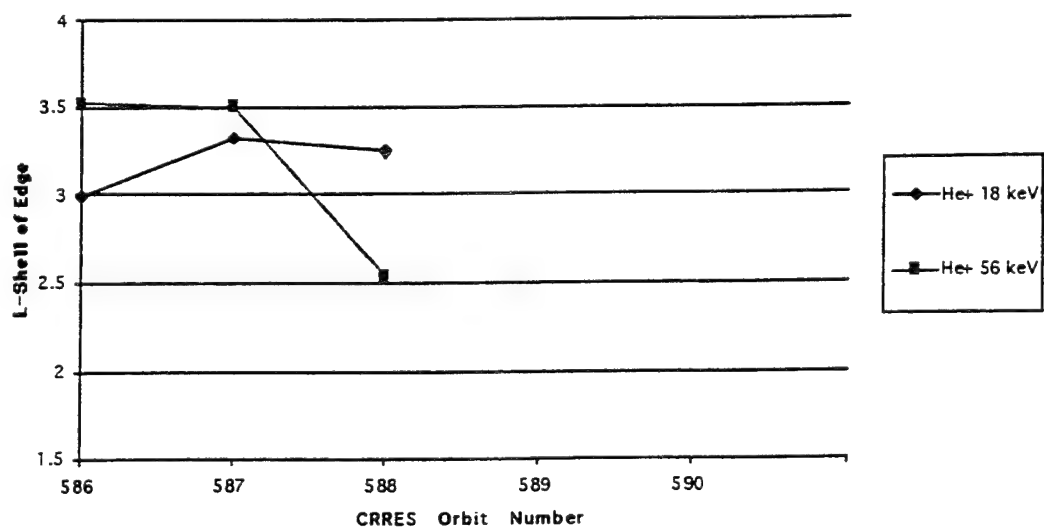


Figure 39 Inner edge ring current ion flux



### **3.6 Rapid drop-off in ion flux in the ring current**

#### **3.6.1 Rapid drop-off in flux at the inner edge of the ring current**

While past observations have revealed the general structure of the ion ring current region, the details of the inner edge are poorly understood because of low sensitivity ion composition measurements and sensitivity of instruments to radiation belt backgrounds. The data collected by IMS-HI clearly show that the hydrogen and helium flux can abruptly drop-off by several orders in less than 0.5 L-shell. Some examples of this lower edge drop-off are shown in figures 37 and 38 for helium ions. The movement of the inner edge during the 24 March magnetic storm is given in Figure 39 and indicates that the inner edge moves down to an L-shell of about 2 for 56 keV He<sup>+</sup> on orbit 590; about one day after the magnetic storm SC. The exact location of the boundary varies with ion species, energy, and magnetic conditions. The data suggest that strong loss processes are active that precipitate ions out of the lower ring current such as ion cyclotron waves, other wave-particle interactions, and charge exchange. The inner edge profiles of the ion ring current are crucial to the elucidation of the transport and loss mechanisms and to the development of proper radiation belt models.

#### **3.6.2 Narrow Flux Drop-offs and Enhancements in the Outer Radiation Belt**

An investigation has been made of localized decreases in the trapped particles, some at positions deep within the trapped population of the radiation belt (see paper in appendix 4; Imhof et al. 1995). The study was performed with the measurements of electrons, protons and helium particles at near equatorial position from the CRRES satellite. Electric field wave and magnetic field strength data recorded on CRRES were also used. Narrow observation time drop-offs well within the trapped population occurred at L shells low as 5.4. Other drop-offs typically at higher L shells had slow decreases in particle flux followed by rapid increases, consistent with those often observed from synchronous orbit satellites. Simultaneous measurements of the flux variations with radial distance can be used to evaluate whether the cause of the infrequent pronounced drop-offs might be attributed to a shift of the particle population, as hypothesized by various investigators. Additional data bearing on this subject were obtained during certain satellite orbits. On one satellite pass at least ten narrow flux drop-offs and several sharp enhancements were observed within four hours surrounding and with a much broader flux drop-off with a slow decrease followed by a rapid recovery. For the flux drop-offs being produced by the motion of flux gradients past the satellite observations indicate a large scale movement of a flux profile with fine structure. Drop-offs were observed in both electrons and protons, on some

occasion with very similar flux profiles whereas in other cases there were major differences such as no proton flux decreases at times of major drop-offs in the electrons.

At synchronous or near-synchronous orbit slow decreases in the fluxes of energetic electrons and protons have been observed followed by very rapid increases (e.g. Walker et al., 1976, Baker and McPherron, 1990, Baker et al., 1993, Nakamura et al., 1994, Nagai, 1982, Erickson et al., 1979). Many of these decreases have been interpreted as resulting from motion of the trapped particle outer boundary whereas the subsequent flux recoveries have been found to be associated with the expansion phase onset of magnetospheric substorms. Most of these observations have been made from a satellite that remains at the same L shell,  $\sim 6.6$ . Narrow flux drop-offs have been observed both at synchronous altitude (Su et al., 1976, Sergeev et al., 1992) and on lower L shells (Yeager and Frank, 1969; Kaufmann et al., 1976; Korth et al., 1994).

Our knowledge of flux drop-offs can be improved by examining the measurements from a satellite such as CRRES which has a highly eccentric nearly equatorial orbit and a variety of particle, wave, and magnetic field instruments. Such an orbit provides one the opportunity to investigate the radial flux profiles of drop-offs as well as to survey their occurrence over a wide range of L shells.

From the CRRES satellite we have found both narrow drop-offs in addition to the commonly observed wider ones which often have a slow flux decrease followed by a rapid recovery. Generally, the flux versus latitude profiles were monotonic in nature with no pronounced structure. On many satellite passes indications of weak drop-offs were found: shells as low as 5.4.

#### **4.0 Summary**

Most of the effort of this contract has been devoted to 1) understanding the new IMS-HI instrument medium energy ion and neutral data (i.e. intercalibration), 2) understanding the fundamental dynamics of the radiation belts, 3) the rapid drop-off in ion flux near the inner edge of the ring current, and 4) investigations regarding the establishment of rapid acceleration using impulse  $dB/dt$  and transport to low L-shell during a sudden commencement. This contract was greatly reduced in original scope due to reduction in available funds; however, we are very thankful for the support and hope to continue studying the IMS-HI using the information acquired in this investigation.

## 5.0 References

- Baker, D.N. and R.L. McPherron, "Extreme Energetic Particle Decreases Near Geostationary Orbit: a Manifestation of Current Diversion within the Inner Plasma Sheet", *J. Geophys. Res.*, 95, 6591-6599, 1990.
- Baker, D.N., T.I. Pulkkinen, R.L. McPherron, J.D. Craven, L.A. Frank, R.D. Elphinstone, J.S. Murphree, J.F. Fennell, R.E. Lopez, and T. Nagai, "CDAW 9 Analysis of Magnetospheric Events on May 3, 1986: Event C", *J. Geophys. Res.*, 98, 3815-3834, 1993.
- Birmingham, T.J. and F.C. Jones, "Identification of Moving Magnetic Field Lines", *J. Geophys. Res.*, 73, 5505, 1968.
- Blake, J.B., W.A. Kolasinski, R.W. Fillius, and E.G. Mullen, "Injection of Electrons and Protons with Energies of Tens of MeV into  $L < 3$  on 24 March 1991", *Geophys. Res. Lett.*, 19, 821-824, 1992.
- Collin, H.L., J.B. Cladis, and J.M. Quinn, "Investigation of Ring Current/Storm Dynamics", PL-TR-92-2161, 1992, ADA256688.
- Erikson, K.N., R.L. Swanson, R.J. Walker, and J.R. Winckler, "A Study of Magnetosphere Dynamics During Auroral Electrojet Events by Observations of Energetic Electron Intensity Changes at Synchronous Orbit", *J. Geophys. Res.*, 84, 931-942, 1979.
- Gloeckler, F., B. Wilken, W. Studemann, F.M. Ipavich, D. Hovestadt, D.C. Hamilton, and G. Kremser, "First Composition Measurement of the Bulk of the Storm-time Ring Current (1-300 keV/e) with AMPTE/CCE", *Geophys. Res. Lett.*, 12, 325, 1985.
- Gussenhoven, M.S., E.G. Mullen, D.H. Brautigam, E. Holeman, C. Jordan, F. Hanser, B. Dichter, "Preliminary Comparison of Dose Measurements on CRRES to NASA Model Predictions", *IEEE Trans. on Nuclear Science*, NS-38, 1655-1662, 1991.
- Henrich, L.R., "A Note on the Compression of the Earth's Magnetic Field and Hypothetically Related Phenomena", *J. Geophys. Res.*, 68, 1295-1302, 1963.
- Hones, E.W., "Motion of Charged Particles Trapped in the Earth's Magnetosphere", *J. Geophys. Res.*, 68, 1209-1219, 1963.
- Hsieh K.C., C.C. Curtis, C.Y. Fan, and M.A. Gruntman, "Techniques for the Remote Sensing of Space Plasma in the Heliosphere Via Energetic Neutral Atoms: a Review", in *Solar Wind Seven*, eds. E. Marsch and R. Schwenn, Pergamon Press, 1992, 357.
- Kauffman, R.L., J.T. Horng, and A. Konradi, "Trapping Boundary and Field-line Motion During Geomagnetic Storms", *J. Geophys. Res.*, 77, 2780-2798, 1972.
- Korth, A., R. Friedal, D.N. Baker, H. Luhr, S.L. Ullaland, J.F. Fennell, and G.D. Reeves, "Dynamics of the Plasma Sheet in the Dawn Sector of the Magnetosphere: Observations from CRRES", Submitted to the proceedings of ICS-2 Fairbanks Alaska, April 19, 1994.

- McEntire, R.W. , Lui, A.T.Y. , Krimigis, S.M., and Keath, E.P. , "AMPTE/CCE Energetic Particle Composition Measurements During the September 4, 1984 Magnetic Storm", *Geophys. Res. Lett.*, 12, 1985, 317-320.
- Mead, G.D., "Deformation of the Geomagnetic Field by the Solar Wind", *J. Geophys. Res.*, 69, 1181, 1964.
- Moritz, J., "Energetic Protons at Low Altitudes: A Newly Discovered Radiation Belt Phenomenon and its Explanation", *Z. Geophys.*, 38, 701, 1972.
- Mullen, E.G, M.S. Gussenhoven, K. Ray, and M. Violet, "A Double-peaked Inner Radiation Belt: Cause and Effect as Seen on CRRES", *IEEE Trans. on Nuclear Science*, NS-38, 1713-1717, 1991.
- Nakamura, Rumi, Daniel N. Baker, Tatsundo Yamamoto, Richard D. Belian, Edgar A. Bering III, James R. Benbrook, and Jeffrey R. Theall, "Particle and Field Signatures During Pseudobreakup and Major Expansion Onset", *J. Geophys. Res.*, 99, 207-221, 1994.
- Nagai, Tsugunoby, "Local Time Dependence of Electron Flux Changes During Substorms Derived from Multi-satellite Observations at Synchronous Orbit", *J. Geophys. Res.*, 87, 3456-3468, 1982.
- Nightingale, R.W., R.R. Vondrak, E.E. Gaines, W.L. Imhof, R.M. Robinson, S.J. Battel, D.A. Simpson, and J.B. Reagan, "CRRES Spectrometer for Electrons and Protons", *J. Spacecraft and Rockets*, 29, 614-617, 1992.
- Parker, E.N., "Geomagnetic Fluctuations and the Form of the Outer Zone of the Van Allen Radiation Belt", *J. Geophys. Res.*, 65, 3117-3130, 1960.
- Pfitzer, K.A., "Acceleration Mechanisms in the Inner Magnetosphere", *EOS Trans. Amer. Geophys. Union*, 73, no. 14, (abstract), 1992.
- Reagan, J.B., R.W. Nightingale, E.E. Gaines, W.L. Imhof, and E.G. Stassinopoulos, "Outer Zone Energetic Electron Spectral Measurements", *J. of Spacecraft and Rockets*, 18, 83-88, 1981.
- Roeloff, E.C., D.G. Mitchell, and D.J. Williams, "Energetic Neutral Atoms (5-50 keV) from the Ring Current, Imp 7/8 and ISEE-1", *J. Geophys. Res.*, 90, 10991-11008, 1985.
- Sergeev, V.A., T. Bosinger, R.D. Belian, G.D. Reeves, and T.E. Cayton, "Drifting Holes in the Energetic Electron Flux at Geosynchronous Orbit Following Substorm Onset", *J. Geophys. Res.*, 97, 6541-6548, 1992.
- Tinsley, B.A., "Neutral Atom Precipitation- a Review", *J. Atmos. Terr. Phys.*, 43, 617, 1981.
- Tsyganenko, N.A., "Global Quantitative Models of the Geomagnetic Field in the Cislunar Magnetosphere for Different Disturbance Levels", *Planet. Sp. Sci.*, 35, 1347-1358, 1987.
- Vampola, A.L. and A.Korth, "Electron Drift Echoes in the Inner Magnetosphere", *Geophys. Res. Lett.*, 19, 625-628, 1992.
- Voss, H.D., "Energy and Primary Mass Determination Using Multiple Solid State Detectors", *IEEE Trans. on Nuclear Science*, NS-29, 178-181, 1982.

- Voss, H.D., W.L. Imhof, M.Walt, J. Mobilia, R.M. Robinson, and R.W. Nightingale, "Intense > 10 MeV particle Injection Near L=2.5 During the 24 March 1991 Magnetic Shock", Eos Trans. Amer. Geophys. Union, 73, no. 14, (abstract), 1992a.
- Voss, H.D., E. Hertzberg, A.G. Ghielmetti, S.J. Battel, K.A. Appert, B.R. Higgins, D.O. Murray, and R.R. Vondrak, "The Medium Energy Ion Mass and Neutral Atom Spectrometer (ONR-307-8-3)", J. Spacecraft and Rockets, 29, 566-569, 1992b.
- Voss, H.D., J. Mobilia, H.L. Collin, and W.L. Imhof, "Satellite Observations and instrumentation for Imaging Energetic Neutral Atoms", SPIE, 1744, Instrumentation for Magnetospheric Imagery, 79-90, 1992c.
- Voss, H.D., "Acceleration of Particles to >10 MeV at L=2.5 During a Sudden Commencement", EOS Trans. Amer. Geophys. Union, (abstract), Fall, 1992d.
- Walker, R.J., K.N. Erikson, R.L. Swanson, and J.R. Winckler, "Substorm- associated Particle Boundary Motion at Synchronous Orbit", J. Geophys. Res., 81, 5541-5550, 1976.
- Yeager, D.M. and L.A. Frank, "Large Temporal Variations of Energetic Electron Intensities at Midlatitudes in the Outer Radiation Zone", J. Geophys. Res., 74, 5697-5708, 1969.

## **Appendix 1**

### **IMS-HI Instrument Paper**

# Medium Energy Ion Mass and Neutral Atom Spectrometer

H. D. Voss,\* E. Hertzberg,† A. G. Ghielmetti,‡ S. J. Battel,§ K. L. Appert,† B. R. Higgins,†  
D. O. Murray,\* and R. R. Vondrak¶  
Lockheed Palo Alto Research Laboratory, Palo Alto, California 94304

The primary objective of the medium energy ion mass spectrometer (ONR 307-8-3) on the CRRES is to obtain the necessary data to construct models of the energetic ion (10–2000 keV- $\text{amu}/q^2$ ) and neutral atom (10–1500 keV) environment of the Earth's radiation belts. The spectrometer measures the energetic ion composition, energy spectrum, charge, and pitch angle distribution with good mass, temporal, and spatial resolution. The ion rejection in the neutral detector is  $< 100 \text{ MeV-}\text{amu}/q^2$ . The instrument principle of operation is based on ion momentum separation in a 7000-G magnetic field followed by energy and mass defect analysis using an array of cooled silicon solid-state detectors. The architecture is parallel with simultaneous mass and energy analysis at relatively high sensitivity (100% duty cycle). The instrument performed as designed in orbit with the major groups of hydrogen, helium, oxygen, and neutrals clearly resolved. The energetic ion composition during the August 26, 1990, storm illustrates the instrument performance.

## I. Introduction

THE medium energy ion mass spectrometer (IMS-HI) on the Combined Release and Radiation Effects satellite (CRRES) measures the energy spectra and pitch angle distributions of magnetospheric ions and neutral particles. The instrument is designed specifically to measure the highly variable fluxes of ions in the energy range from a few tens of kiloelectron volts to a few hundred kiloelectron volts that populate the ring current and produce the variations seen in the magnetic Dst index associated with magnetic storms.

Ring-current studies based on data from the Explorer 45 spacecraft<sup>1</sup> were hampered because the detectors did not distinguish between protons and higher mass ions. Other researchers<sup>2–5</sup> have demonstrated the importance of including neutrals and ions other than protons to explain the decay rates observed in the ring current. By charge exchange with thermal hydrogen atoms, energetic ions become neutrals and can escape from the Earth's environment. This is a significant loss process for the medium-energy ring current ions. More recent measurements obtained by the medium-energy plasma analyzer on the AMPTE/CCE spacecraft have demonstrated the advantages of comprehensive ion composition measurements for the study of ring current processes.<sup>6</sup>

On CRRES, ring-current ion composition and neutral atom measurements are provided in part by the IMS-HI instrument. This instrument is one of four instruments that comprise the Office of Naval Research (ONR-307) energetic particles and ion composition (EPIC) experiment. The contiguous mapping of the particle distribution over the radial distance range from 400 km to 5.5 Earth radii ( $R_E$ ) near the equatorial plane provides a comprehensive data base that can be used for studies of radiation belt and ring-current energization, injection, and loss processes.

## II. Measuring Techniques

The IMS-HI instrument is based on ion momentum separation in a magnetic field followed by energy and mass defect analysis using an array of cooled silicon solid-state sensors as shown in Fig. 1. The entrance collimator consists of a series of rectangular baffles that define the ion beam angular resolution and a broom magnet to reject electrons with energy less than 1 MeV.

After exiting the collimator ions enter a 7000-G magnetic field where they are deflected ( $mv/qB$ ) onto a set of six passively cooled ( $-50^\circ\text{C}$ ) silicon surface-barrier detectors. The technique of cooling solid-state detectors for high-resolution [ $< 2 \text{ keV}$  full width at half maximum (FWHM)] energetic ion measurements in spacecraft instruments was discussed by Voss et al.<sup>7</sup> and was successfully demonstrated in the stimulated emission of energetic particles (SEEP) experiment on the S81-1 satellite.<sup>8</sup> The energy range covered varies with ion species and is approximately  $\text{em}/q^2 = 10\text{--}2000 \text{ keV-}\text{amu}/q^2$ . A seventh sensor, located directly in line with the collimator, measures energetic neutrals and has an ion rejection of approx-

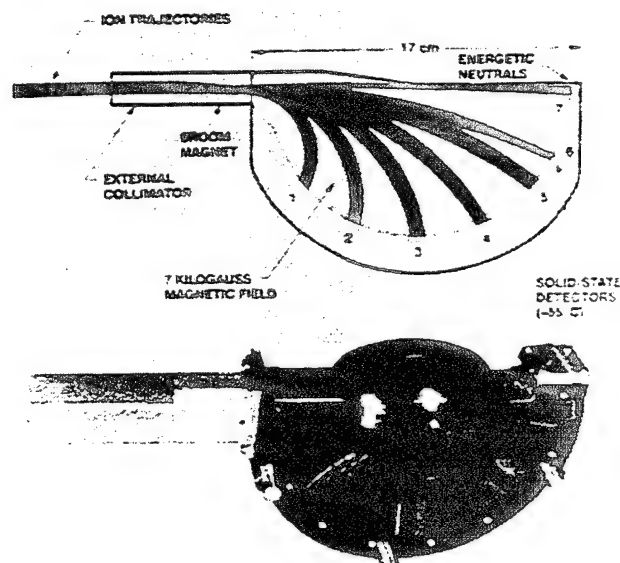


Fig. 1 Principle of operation for IMS-HI is based on ion momentum, mass defect, and energy analysis using an array of cooled solid-state detectors. Magnet is shown in the upper portion of the figure and the ion optics in the lower portion.

Received July 12, 1991; revision received Oct. 11, 1991; accepted for publication Oct. 11, 1991. Copyright © 1992 by the American Institute of Aeronautics and Astronautics, Inc. All rights reserved.

\*Staff Scientist, Space Sciences Laboratory, Dept. 91-20, B/255, 3251 Hanover Street.

†Research Engineer, Space Sciences Laboratory, Dept. 91-20, B/255, 3251 Hanover Street.

‡Research Scientist, Space Sciences Laboratory, Dept. 91-20, B/255, 3251 Hanover Street.

§Space Sciences Laboratory, Dept. 91-20, B/255, 3251 Hanover Street; currently, Consultant, Battel Engineering. Member AIAA.

¶Manager, Space Sciences Laboratory, Dept. 91-20, B/255, 3251 Hanover Street. Associate Fellow AIAA.



**Table 1** Medium energy ion mass spectrometer (IMS-HI) specifications

Analyzer	7 kg magnet (m/q <sup>2</sup> ) and mass defect
Sensors	Silicon surface barrier (-55°C)
Number of imaging sensors	7 at 0.5 cm <sup>2</sup> each
Look direction from spin axis	75 deg
Particles and energy range:	
Neutrals	10–1500 keV
Protons	15–2000 keV
Helium	4–500 keV
Oxygen	20–130 keV
Oxygen + +	20–500 keV
Other ions	E > 20 keV
Number of differential mass channels	64
Number of high rate mass channels	4
Number of differential energy channels	6
Pitch angle resolution	4 deg FWHM
Geometrical factor	10 <sup>-2</sup> –10 <sup>-3</sup> cm <sup>2</sup> sr
Duty cycle	100%

imately 100 MeV-amu/q<sup>2</sup>. Detailed instrument specifications are given in Table 1.

The instrument features simultaneous mass and energy analysis at relatively large geometrical factors (10<sup>-3</sup> to 10<sup>-2</sup> cm<sup>2</sup> sr). Simultaneous measurements of charge states can be identified for each m/q<sup>2</sup> and for the same m/q<sup>2</sup>, in some cases, within the solid-state detector due to dead zone and mass defect energy losses for equal m/q<sup>2</sup> (e.g., O<sup>++</sup> and He<sup>+</sup>). Because of the multisensor design and parallel processing electronics, the dynamic range in flux covered is approximately six orders of magnitude.

A simulation of the ion separation in a 7000-G magnetic field is shown in the position-energy diagram of Fig. 2. The image surface *S* is defined as the arc length, beginning at the collimator, for a radius *R* = 8 cm. Solid-state detectors 1–7 are located at angles  $\theta$  of 40, 65, 90, 115, 140, 162.5, and 180 deg, respectively. Solid-state detectors 1–6 are *n*-type silicon having either 20 or 40  $\mu\text{g cm}^{-2}$  of gold surface deposit. The neutral detector is of *p*-type silicon to improve light rejection and radiation damage sensitivity and has 20  $\mu\text{g cm}^{-2}$  of aluminum surface deposit. The energy loss in surface-barrier windows for H, He, and O is discussed by Voss.<sup>9</sup> The mass defect in solid-state detectors results from energy loss of nonionizing nuclear collisions within the solid that reduce the efficiency of electronic signal generation. The mass defect increases with atomic weight of the nuclei in a well-understood way<sup>10</sup> and causes further mass separation, with commensurate energy scatter, for the heavier nuclei.

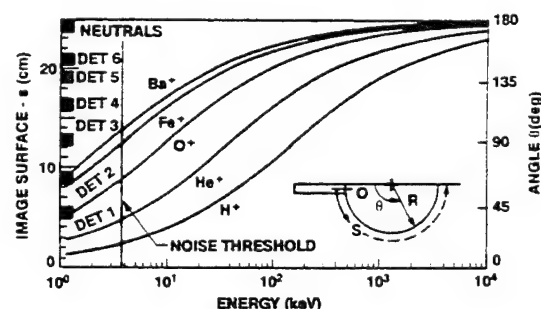
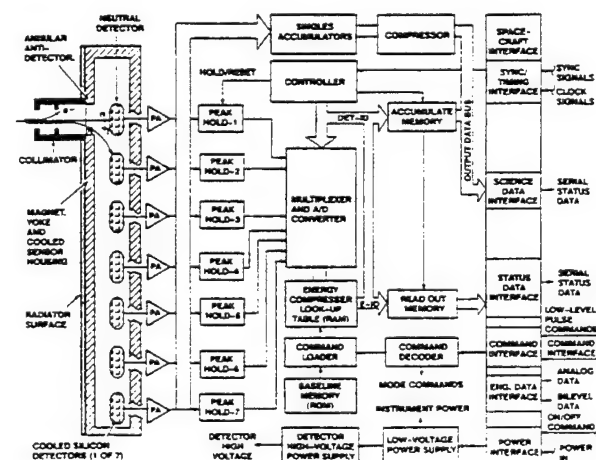
The magnet section consists of a yoke, pole pieces, and a SmCo permanent magnet. To produce a homogeneous magnetic field with high inducton (~7 kG) in a 5-mm gap and with minimized weight, the best available magnetic material (SmCo Recoma 25, with 25 MGOe energy product) was selected. The yoke completely surrounds the magnetic field except for the entrance aperture, permitting one to reduce the magnetic resistivity in the return flux section and to minimize the magnetic stray fields. Shape and dimensions of the yoke are optimized to reduce weight and are designed for a uniform magnetic induction of 19 kG anywhere within the yoke. The resultant complex shape necessitates the use of numerical computer-aided machining methods to meet the weight requirement and design goal of  $\leq 100$  nT magnetic stray field at a distance of 1 m. A yoke material (Hyperco 50) that possesses relatively high permeability (2000–4000) at high-induction levels (20 kG) was chosen. The mass of the flight yoke and magnet assembly is about 5.7 kg.

A functional system diagram of the IMS-HI is shown in Fig. 3. Variable pulse-height signals from the ion sensors are each routed for analysis to a peak detector circuit and analog multiplexer. Each peak detector circuit is allowed to track and

hold the highest peak value for input pulses below the programmable low level threshold  $V_T$  and to hold and stop sampling for input pulses above  $V_T$ . This allows signals to be processed well into the noise level for added in-orbit performance. The sample interval for each detector is 45  $\mu\text{s}$ . The read and reset of each peak detector circuit is controlled by strobes from a master clock so that a continuous and sequential scan is made of each detector.

Simultaneous with the reset command, a 256-channel analog-to-digital converter is activated, and the resulting digital pulse height (8 bits) is placed on the address bus of an energy lookup table. Also placed on the address bus of this RAM are the 3 bits that specify which detector is being processed. The content of this memory cell (16 bits) is read into an accumulator, incremented by one, and then read back into the memory cell. An address counter is then used to sequentially step through the entire RAM for telemetry readout. A data compressor packs the 16-bit sum into an 8-bit byte for serial interface with the satellite telemetry.

The instrument operates in two basic modes; mass lock and mass scan. In the mass scan mode, each of the seven solid-state sensors is pulse-height analyzed into 256 levels of which 64 intervals are accumulated in memory and read out every 8 s. This mode is used to scan all mass peaks within the range of the sensor relative to the background continuum. In the mass lock mode, each of the seven solid-state sensors is pulse-height analyzed into 256 levels, of which four intervals (typically, four ions) are accumulated in memory and read out every half-second. This mode is used for making rapid spectral snapshots of four ions as a function of pitch angle. Baseline operation of the instrument will be to toggle every 32.768 s between the mass lock mode and the mass scan mode.

**Fig. 2** Energy of various ions that are mapped onto the detector focal surface *S* is shown for a 7000-G magnetic field.**Fig. 3** Functional block diagram of the IMS-HI instrument.



### III. Calibration

The IMS-HI instrument was calibrated at Goddard Space Flight Center (GSFC) using the low-energy accelerator for ions up to 150 keV. The instrument was mounted on a scan platform in a vacuum chamber at the output end of the accelerator beam line. At a bend in the beam line, an electromagnet was used to select the desired mass after the electrostatic acceleration. A solid-state detector at the entrance to the vacuum test chamber was used to monitor the beam stability. The instrument was calibrated using  $H^+$ ,  $He^+$ ,  $He^{++}$ ,  $N^+$ ,  $N^{++}$ ,  $O^+$ , and  $O^{++}$  ions. The neutral detector was calibrated using energetic neutral hydrogen atoms.

To illustrate the instrument performance during calibration, an energy scan for protons impinging on detector 2 is shown in Fig. 4. The calibration data are currently being compared to the instrument computer model and to the flight data to arrive at the best-fit calibrations. The energy passbands are very clean as indicated in Fig. 4 and scattering from the pole pieces is less than 0.2%. The background rate can be subtracted using an algorithm based on the differential pulse-height spectrum in each of the seven detectors and the omnidirectional megaelectron volt electron flux.

In addition to the accelerator calibrations, the instrument was tested with radioactive sources at  $-30^\circ\text{C}$  in its final flight configuration. Six Tl-204 sources of varying intensities were used to saturate the sensors in a known fashion to calibrate flux rate effects. An internal electronic pulser was also included in the instrument to give several pulse heights at the detector front end to calibrate gain, linearity, and resolution in orbit. It has also been observed in orbit that, when the instrument is illuminated with high fluxes of megaelectron volt electrons in the outer belt, K-alpha lines are present and associated with high-atomic-number materials near the sensors.

### IV. Preliminary Flight Results

The instrument design temperatures were achieved:  $-55^\circ\text{C}$  for the magnet and sensors,  $-12^\circ\text{C}$  for the preamps, and  $0^\circ\text{C}$

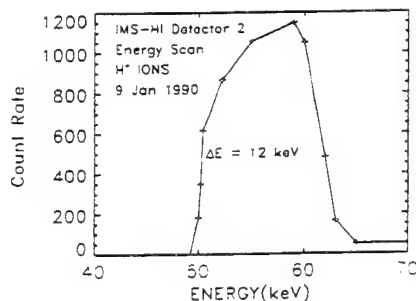


Fig. 4 Energy passband for protons in detector 2 obtained during preflight calibrations.

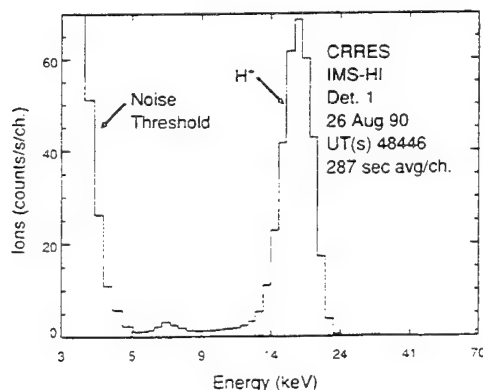


Fig. 5 In-flight data from detector 1 indicates a noise threshold of about 4 keV and a hydrogen ion peak resolution of 2 keV FWHM.

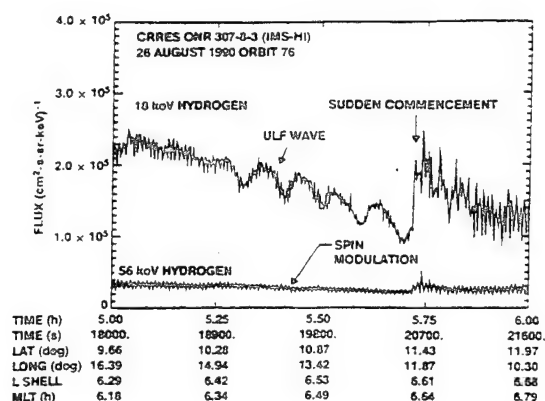


Fig. 6 Example of scalar data from detector 1 and 2 for protons during the August 26, 1990, sudden commencement.

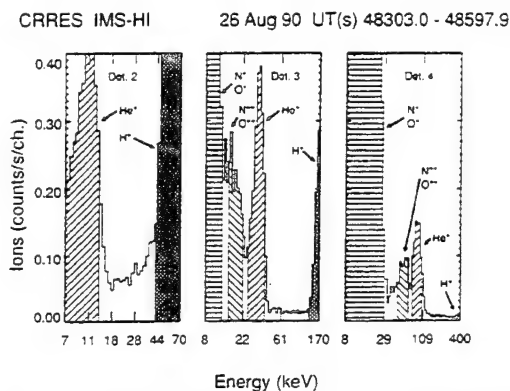


Fig. 7 Ion mass peaks observed in detectors 2, 3, and 4 during the August 26, 1990, storm.

for the electronics box. The sensors' noise thresholds were therefore well within specifications. This is shown in Fig. 5 for detector 1 during orbit 77. Here the primary hydrogen peak is at 18 keV with a noise threshold of about 4 keV and a noise resolution of about 2 keV FWHM.

The scalar data for 18- and 56-keV protons during the sudden commencement on August 26, 1990, is illustrated in Fig. 6. The major ultra lower frequency (ULF) wave-particle interaction is at 18 keV and nearly absent at 56 keV.

The final example of instrument performance is shown in Fig. 7 for the 64-channel mass spectrum of detectors 2, 3, and 4. These data were obtained on August 26, 1990 over a 5-min interval near  $L = 5.0$ . The distributions shown are for the raw count rates and do not have noise filtering, efficiencies, and other corrections included. The energy scale is preliminary and represents the deposited energy of the ions in the solid-state detectors.

The  $H^+$  and  $He^+$  peaks are conspicuous in each of the detectors as noted. The importance of mass defect in the solid-state detector is illustrated well in detector 4 for  $He^+$  and  $O^{++}$ . Both ions have the same  $m/q^2$  and thus the same energy incident on the detector (95 keV). Because the oxygen ion is less efficient at generating electron hole pairs, its peak is shifted down from the  $He^+$  peak by about 30 keV. It is well separated from the  $He^+$  and  $N^+/O^+$  peaks. Thus, over certain energy and mass intervals the mass defect is an effective method of separating ion beams in a magnetic spectrometer. To obtain the ion flux, the penetrating backgrounds and skirts of the strong ion peaks must be properly subtracted using peak-analysis software.

### V. Summary

The IMS-HI experiment on CRRES operated successfully since launch. Preliminary results show that the instrument is

able to distinguish all of the major ion species and a few minor species with good time resolution. These measurements will comprise an important data base for studies of radiation belt and ring-current energization, injection, and decay rates.

### Acknowledgments

This effort was supported by the Office of Naval Research under Contract N00014-83-C-0476 and by the Lockheed Independent Research Program. The authors wish to thank F. Hilsenrath, L. A. Hooker, T. C. Sanders, D. A. Simpson, and V. F. Waltz for their efforts in the design, development, and fabrication of this instrument. We wish to thank R. M. Robinson and J. Mobilia for comments on the manuscript, and R. A. Baraze and R. McDonald for their efforts in data analysis. Appreciation is extended to R. G. Joiner for his program management role of our instruments at ONR. We also deeply appreciate the assistance of W. L. Imhof, J. M. Quinn, J. B. Reagan, R. D. Sharp, and E. G. Shelley. The assistance of S. Brown of GSFC was critical to the final calibration of this instrument.

### References

- <sup>1</sup>Smith, P. H., and Hoffman, R. A., "Ring Current Particle Distributions During the Magnetic Storms of December 16-18, 1971," *Journal of Geophysical Research*, Vol. 78, No. 22, 1973, pp. 4731-4737.
- <sup>2</sup>Lyons, L. R., and Evans, D. S., "The Inconsistency Between Proton Charge Exchange and the Observed Ring Current Decay," *Journal of Geophysical Research*, Vol. 81, No. 34, 1976, pp. 6197-6200.
- <sup>3</sup>Spjeldvik, W. N., and Fritz, T. A., "Energetic Ionized Helium in the Quiet Time Radiation Belts: Theory and Comparison with Observations," *Journal of Geophysical Research*, Vol. 83, No. A2, 1978, pp. 654-662.
- <sup>4</sup>Tinsley, B. A., "Effects of Charge Exchange Involving H and H<sup>+</sup> in the Upper Atmosphere," *Planetary and Space Science*, Vol. 26, 1978, p. 847.
- <sup>5</sup>Williams, D. J., "Dynamics of the Earth's Ring Current: Theory and Observation," *Space Science Review*, Vol. 42, 1985, p. 375.
- <sup>6</sup>McEntire, R. W., Lui, A. T. Y., Krimigis, S. M., and Keath, E. P., "AMPTE/CCE Energetic Particle Composition Measurements During the September 4, 1984 Magnetic Storm," *Geophysical Research Letters*, Vol. 12, No. 5, 1985, pp. 317-320.
- <sup>7</sup>Voss, H. D., Reagan, J. B., Imhof, W. L., Murray, D. O., Simpson, D. A., Cauffman, D. P., and Bakke, J. C., "Low Temperature Characteristics of Solid State Detectors for Energetic X-ray, Ion and Electron Spectrometers," *IEEE Transactions on Nuclear Science*, Vol. NS-29, 1982, pp. 164-168.
- <sup>8</sup>Imhof, W. L., Reagan, J. B., Voss, H. D., Gaines, E. E., Datlowe, D. W., Mobilia, J., Helliwell, R. A., Inan, U. S., Katsufakis, J., and Joiner, R. G., "The Modulated Precipitation of Radiation Belt Electrons by Controlled Signals from VLF Transmitters," *Geophysical Research Letters*, Vol. 10, No. 8, 1983, pp. 615-618.
- <sup>9</sup>Voss, H. D., "Energy and Primary Mass Determination Using Multiple Solid State Detectors," *IEEE Transactions on Nuclear Science*, Vol. NS-29, 1982, pp. 178-181.
- <sup>10</sup>Forcinal, G., Siffert, P., and Coche, A., "Pulse Height Defects due to Nuclear Collisions Measured with Thin Window Silicon Surface Barrier Detector," *IEEE Transactions on Nuclear Science*, Vol. NS-15, 1968, p. 475.

## Appendix 2

### SEP Instrument Paper

The U.S. Government is authorized to reproduce and sell this report. Permission for further reproduction by others must be obtained from the copyright owner.

## CRRES Spectrometer for Electrons and Protons

R. W. Nightingale,\* R. R. Vondrak,† E. E. Gaines,\*  
W. L. Imhof,‡ R. M. Robinson,§ S. J. Battel,¶  
D. A. Simpson,\*\* and J. B. Reagan††  
Lockheed Palo Alto Research Laboratory,  
Palo Alto, California 94304

### Introduction

**I**MPORTANT components of the magnetospheric plasma to be explored by the CRRES are the energetic electrons and protons that populate the Earth's radiation belts. The fluxes of these particles depend critically on the production and loss mechanisms in the radiation belts and exhibit dynamic behavior in response to solar and geomagnetic activity.<sup>1,2</sup> The understanding of these processes requires detailed measurements of the particle distribution functions including the pitch angle. Previous measurements of energetic electrons and protons have been made by instruments on satellites such as Ogo 5,<sup>3</sup> SCATHA,<sup>4</sup> (S/C) 1979-053, and (S/C) 1982-019,<sup>1,2</sup> but the unique CRRES orbit offers exciting new possibilities for developing improved models of the inner and outer radiation belts.<sup>5,6</sup> For example, the particle distributions measured along the spacecraft trajectory can be used to map the two-dimensional radiation belt morphology in the orbit plane for  $1.05 < L \leq 7$  near the geomagnetic equator.

The ONR 307-3 Spectrometer for Electrons and Protons (SEP) is one component of the ONR 307 Energetic Particles and Ion Composition experiment. SEP measures the energy and pitch angle distributions of energetic electrons and protons throughout the CRRES orbit. The specific science objectives of the SEP experiment are 1) to understand the physics of the sources, losses, energization, transport, and lifetimes of energetic particles in the Earth's radiation belts; 2) to understand the details of wave-particle interactions (WPI), both natural and man made, that result in precipitation of radiation belt particles; and 3) to utilize this experimental data base to greatly improve the accuracy of trapped radiation belt models.

### Experiment Description and Operations

The SEP design is based heavily on the successful SC-3 spectrometer<sup>4,7</sup> flown on the SCATHA mission. Unlike the single-detector system used on SCATHA, SEP consists of three solid-state particle spectrometers oriented at 40, 60, and 80 deg from the spacecraft spin axis. A cross-sectional view of one of the telescopes is shown in Fig. 1. Each spectrometer has four detector elements labeled A, D, E, and E'. Various logic combinations of the four detector elements in each spectrometer are used to determine the particle types and energy ranges, which are measured sequentially. The operational modes of each telescope are individually commandable.

The D detector, which is 200- $\mu\text{m}$ -thick intrinsic silicon, is used to measure both the rate of energy loss of the higher-energy particles and to directly stop and measure the low-energy particles. The E detector, which consists of a stack of five 2-mm-thick silicon surface-barrier detectors in parallel, is located behind the D detector to stop the higher-energy particles and to measure their total energy loss. The E' detector, which is a 1000- $\mu\text{m}$ -thick piece of silicon, is located behind the E detector and is used as an active collimator. Following it is a tungsten absorber that sets the upper energy limit for analysis. The entire telescope-configured stack is surrounded by the anticoincidence A detector, which consists of a plastic scintillator viewed by a photomultiplier tube. The A detector senses and rejects energetic particles and bremsstrahlung that penetrate either the outer shielding walls of aluminum and tungsten or the silicon detector stack and tungsten absorber. The detector stack is located behind a long, narrow collimator that defines the 3-deg angular field of view full width at half maximum (FWHM). The aluminum and tungsten effectively stop electrons with energy up to 5 MeV and bremsstrahlung photons with energy up to about 150 keV.

Each of the three identical SEP particle telescopes has a high-resolution, 3-deg (FWHM) field of view provided by a long collimator (20 cm) containing 10 baffles. The collimators are identical to the ones used on the SC-3 instrument,<sup>4</sup> providing an instrument geometric factor of  $\sim 3 \times 10^{-3} \text{ cm}^2\text{-sr}$ . For the 80- and 60-deg telescopes, measurements over 12 energy channels are obtained every 0.25 s with a dead time of 2 ms. Because of telemetry restrictions, the 40-deg telescope accumulates for 0.5 s with a dead time of 4 ms.

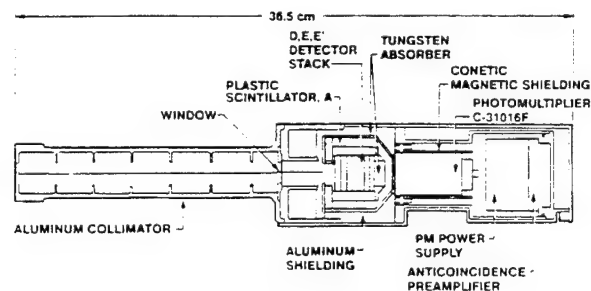


Fig. 1 Cross-sectional view of one of the SEP telescopes.

Received June 18, 1991; revision received Sept. 3, 1991; accepted for publication Sept. 3, 1991. Copyright © 1992 by the American Institute of Aeronautics and Astronautics, Inc. All rights reserved.

\*Research Scientist.

†Manager, Associate Fellow AIAA.

‡Consulting Scientist.

§Staff Scientist.

¶Consultant, Battel Engineering, Member AIAA.

\*\*Senior Staff Research Engineer.

††General Manager, Fellow AIAA.

The three SEP spectrometer heads and the analyzer package are shown in Fig. 2. The two units are mounted on the bottom of the spacecraft and are separated to achieve a lower temperature in the silicon detectors for improved low-energy electron detection.<sup>8,9</sup>

Each sensor operates from its own 256, 8-bit word CMOS memory, which is individually addressable and loadable via a 16-bit serial-digital command. Four of these words completely define one operating mode (32-bit control register) for an individual sensor. A mode is defined by specifying the logic conditions (coincidence/anticoincidence), gain, detector for pulse-height analysis, and energy thresholds required between the four detector elements to uniquely establish a particular type and energy range for analysis.<sup>4</sup>

Several modes can be programmed in sequence to emphasize one particle type, to obtain comprehensive measurements for special events such as solar flares, or to dwell on a narrow energy range for any particle type. A hard-wired backup mode that measures the higher-energy electrons (215–5100 keV) is independent of the memory and is used automatically at turn-on and whenever the memory is being loaded or disabled. The basic programmable mode parameters are the energy range and energy channel widths for the electrons and for the protons. Typical modes that may be used during the CRRES mission are shown in Table 1.

### Calibration

The SEP sensor heads were calibrated using electron and proton beams from accelerators at the Goddard Space Flight Center (GSFC) in Greenbelt, Maryland, and at Harvard University in Cambridge, Massachusetts. Two accelerators were utilized at GSFC, a low-energy electron machine for energies up to 150 keV and a Van de Graaff accelerator with a maximum energy of 1.5 MeV for both electrons and protons. The sensors were in vacuum at room temperature for these runs. The beam rate of the low-energy accelerator was stable to about 25% at a few thousand counts per second for electrons between 25 and 150 keV. The Van de Graaff accelerator

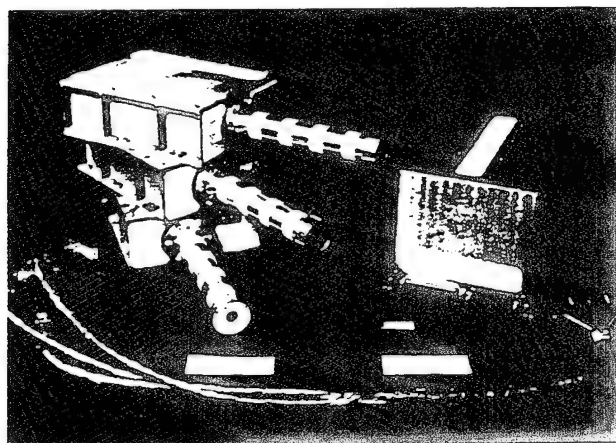


Fig. 2 Photograph of the three SEP telescopes mounted together and the electronics analyzer package.

extended the electron measurements to 1500 keV in 10 steps and started the proton range from 500 to 1500 keV in five energy steps.

High-energy proton calibrations were done in air at the Harvard Cyclotron Laboratory for eight energy steps between 35 and 100 MeV. The 159-MeV proton beam was reduced in energy by absorbers that produce a beam energy spread of less than 6% at 90 MeV and above, whereas the spread is about 40% at the lowest energies. The measured energy deposition from higher-energy protons penetrating the detectors was within 1 MeV of calculated values.

Figure 3 shows examples of calibration data for electrons and protons. The spectra of monoenergetic beams were obtained with a laboratory multichannel analyzer and were related to the 12 channels of the flight pulse-height analyzers by voltage levels. The calibration data were used to specify the energy ranges for each mode of each sensor as shown in Table 1. The mode ranges are electronically divided into 12 channels, each approximately having the channel width shown in the table. The energy ranges in Table 1 show some overlap between modes. The particle collimation, the D detector absorption, and the sensor coincidence circuitry combine to significantly reduce the overlap.

### Results

SEP commenced normal operations on August 7, 1990, after a successful instrument activation period. Preliminary results are shown in Figs. 4 and 5. Figure 4 shows pitch angle spectrograms for electrons and protons measured during orbit 79 by the sensor that is 80 deg from the spin axis. This orbit occurred several days after the commencement of a moderate magnetic storm ( $Dst = -116$ ). Each panel shows the relative flux of electrons or protons integrated over the energy ranges

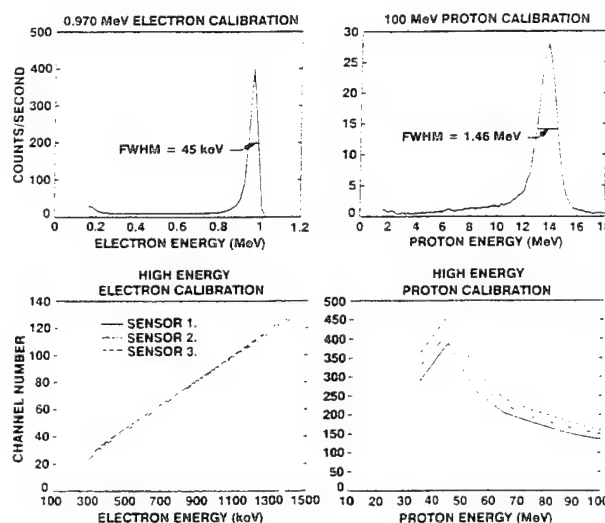


Fig. 3 Examples of calibration data showing typical spectra of the particle beams and the pulse-height responses vs energy in all three sensors for high-energy electrons and protons.

Table 1 SEP initial energy range and channel width

Mode	Sensor A		Sensor B		Sensor C	
	Energy range, MeV	Width, MeV	Energy range, MeV	Width, MeV	Energy range, MeV	Width, MeV
Electron 1	0.042–0.324	0.0235	0.042–0.336	0.0245	0.041–0.313	0.0227
Electron 2	0.164–4.93	0.397	0.171–5.12	0.413	0.170–5.11	0.412
Proton 1	0.875–6.60	0.478	0.916–6.70	0.482	0.920–6.80	0.490
Proton 2	2.5–38.7	3.01	2.2–33.7	2.62	2.0–30.4	2.37
Proton 3	35.8–80.2	3.7	31.2–69.9	3.22	28.2–63.1	2.91
Proton 4	45–94	4.08	45–105	5.00	45–110	5.42
Alphas	6.8–24	1.43	6.90–24.3	1.45	7.00–24	1.47

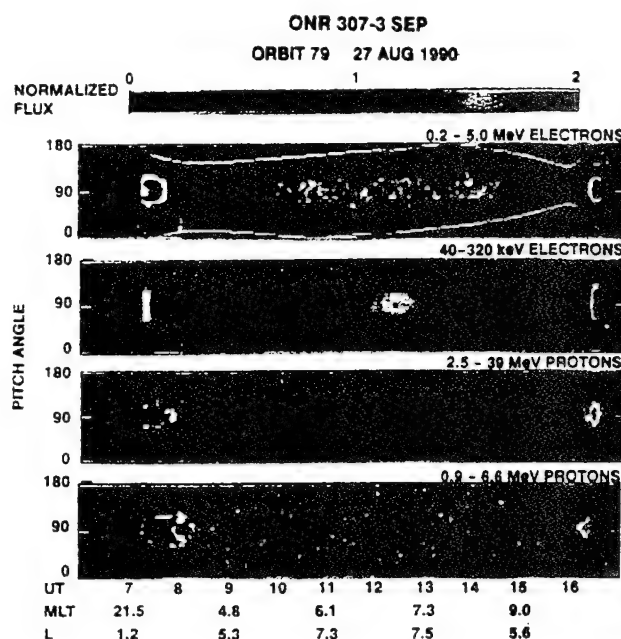


Fig. 4 Pitch angle spectrograms showing relative intensities of electrons and protons measured during orbit 79. The intensities are normalized to the average differential, directional flux measured during the 64-s sampling interval.

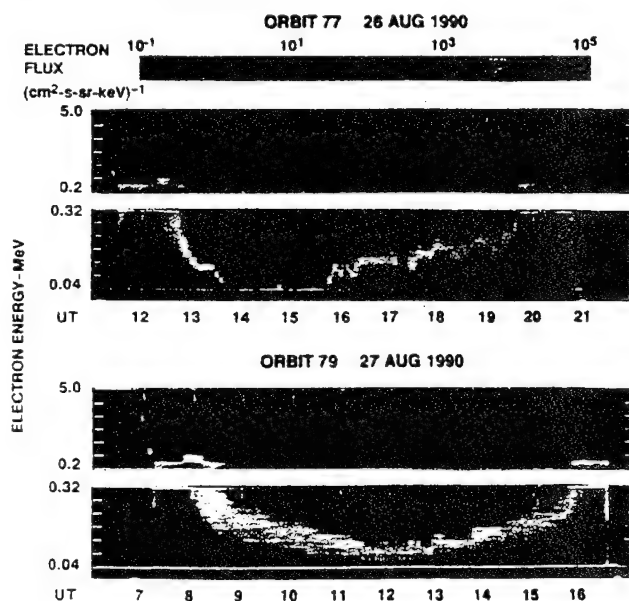


Fig. 5 Energy time spectrograms showing approximately spin-averaged fluxes of electrons during orbits 77 and 79.

indicated in the upper right-hand portion. The intensity is color coded according to the flux in 4-deg-wide pitch angle bins normalized to the average differential, directional flux measured during each sampling interval. A full energy and pitch angle distribution is obtained in 64 s in the normal SEP operating mode. The time axis in the plot is arranged with perigee near the beginning and end and apogee at the center. Note how the pitch angle coverage for this detector varies during the orbit. Depending on the orientation of the magnetic field, data from the other two sensors can extend the pitch angle coverage achievable with a single telescope. Evidence for both pancake and butterfly pitch angle distributions are apparent in this display.

Figure 5 shows energy time spectrograms for electrons measured during orbits 77 and 79. The differential number fluxes

are averaged over 32 s; because the satellite spin is about 29 s, these are approximately spin-averaged fluxes. The data for each orbit are shown in two panels corresponding to the low- and high-energy electron ranges. The large dropout in fluxes in the first half of the orbit is a result of the magnetic storm that commenced one orbit earlier. Two orbits later, the energetic particle fluxes have recovered. Just after 12 UT in orbit 79 there are three dispersive-like electron events possibly associated with substorm activity.

To obtain the differential particle flux from the SEP data, the counts in each sampling interval are divided by the product of the live time, the spectrometer geometric factor, the energy width of the channel for the particular mode, and the sensor particle detection efficiency for the channel. Pitch angle distributions for each sensor are calculated using the sensor look directions and the magnetic field direction determined from the onboard magnetometer.

## Conclusions

The SEP experiment on CRRES operated almost continuously throughout the lifetime of the spacecraft. The data obtained in the CRRES orbit allows the computation of the particle distribution functions in phase space for energetic electrons and protons throughout the radiation belts. These distributions can be used for developing models of both the static and dynamic radiation belt populations. Preliminary work toward a dynamic model has been completed using SCATHA outer-belt electron distributions together with a general solution to a simple form of the simultaneous bimodal (radial and pitch-angle) diffusion equation.<sup>10,11</sup> The SEP data are especially suited for these types of studies because of the good angular resolution and extended pitch angle coverage provided by the three telescopes.

## Acknowledgments

This work was primarily supported by the Office of Naval Research under Contract N00014-83-C-0476 and in part by the Lockheed Independent Research Program. The authors wish to thank J. C. Bakke, L. A. Hooker, and V. F. Waltz for their efforts in the design, development, and fabrication of this instrument. We also deeply appreciate the contributions provided at Lockheed by H. D. Voss and J. M. Quinn. Special appreciation goes to the Ball Aerospace Systems Division who built the CRRES satellite; to the USAF Space Test Program and the NASA Marshall Space Flight Center, who shared in the management of the project; to General Dynamics for the successful launch of Atlas-Centaur rocket; and to the USAF Consolidated Space Test Center, which operated the satellite.

## References

- <sup>1</sup>Baker, D. N., Blake, J. B., Klebesadel, R. W., and Higbie, P. R., "Highly Relativistic Electrons in the Earth's Outer Magnetosphere, I. Lifetimes and Temporal History, 1979-1984," *Journal of Geophysical Research*, Vol. 91, No. A4, 1986, pp. 4265-4276.
- <sup>2</sup>Baker, D. N., Blake, J. B., Callis, L. B., Belian, R. D., and Cayton, T. E., "Relativistic Electrons Near Geostationary Orbit: Evidence for Internal Magnetospheric Acceleration," *Geophysical Research Letters*, Vol. 16, No. 6, 1989, pp. 559-562.
- <sup>3</sup>West, H. I., Jr., Buck, R. M., and Walton, J. R., "Electron Pitch Angle Distributions Throughout the Magnetosphere as Observed on Ogo 5," *Journal of Geophysical Research*, Vol. 78, No. 7, 1973, pp. 1064-1081.
- <sup>4</sup>Reagan, J. B., Nightingale, R. W., Gaines, E. E., Imhof, W. L., and Stassinopoulos, E. G., "Outer Zone Energetic Electron Spectral Measurements," *Journal of Spacecraft and Rockets*, Vol. 18, No. 1, 1981, pp. 83-88.
- <sup>5</sup>Teague, M. J., and Vette, J. I., "The Inner Zone Electron Model AE-5," National Space Science Data Center/World Data Center A for Rockets and Satellites, Rept. 72-10, Nov. 1972.
- <sup>6</sup>Singley, G. W., and Vette, J. I., "The AE-4 Model of the Outer Radiation Zone Electron Environment," NSSDC 72-06, Aug. 1972.
- <sup>7</sup>Stevens, J. R., and Vampola, A. L., "Description of the Space Test Program P78-2 Spacecraft and Payloads," Space and Missile Systems Organization, Air Force Systems Command, TR-78-24, Los

Angeles Air Force Station, Los Angeles, CA, Oct. 1978.

<sup>8</sup>Voss, H. D., Reagan, J. B., Imhof, W. L., Murray, D. O., Simpson, D. A., Cauffman, D. P., and Bakke, J. C., "Low Temperature Characteristics of Solid State Detectors for Energetic X-ray, Ion and Electron Spectrometers," *IEEE Transactions on Nuclear Science*, Vol. NS-29, No. 1, 1982, pp. 164-168.

<sup>9</sup>Voss, H. D., Bakke, J. C., and Roselle, S. N., "A Spacecraft Multichannel Analyzer for a Multidetector Solid State Detector Array," *IEEE Transactions on Nuclear Science*, Vol. NS-29, No. 1, 1982, pp. 173-177.

<sup>10</sup>Chiu, Y. T., Nightingale, R. W., and Rinaldi, M. A., "Simultaneous Radial and Pitch Angle Diffusion in the Outer Electron Radiation Belt," *Journal of Geophysical Research*, Vol. 93, No. A4, 1988, pp. 2619-2632.

<sup>11</sup>Chiu, Y. T., Rinaldi, M. A., and Nightingale, R. W., "Toward Dynamic Modeling of the Outer Electron Radiation Belt," *Journal of Geophysical Research*, Vol. 95, No. A8, 1990, pp. 12,069-12,074.

---

## **Appendix 3**

### **Neutral Atom Imaging Paper**



## Satellite observations and instrumentation for imaging energetic neutral atoms

H. D. Voss, J. Mobilia, H. L. Collin, and W. L. Imhof

Space Sciences Laboratory, 0/91-20 B/255  
Lockheed Palo Alto Research Laboratory  
3251 Hanover Street, Palo Alto, CA 94304

### ABSTRACT

Direct measurements of energetic neutral atoms (ENA) and ions have been obtained with the cooled solid state detectors on the low altitude (220 km) three-axis stabilized S81-1/SEEP satellite and on the spinning 400 km  $\times$  5.5 Re CRRES satellite. During magnetic storms ENA and ion precipitation ( $E > 10$  keV) is evident over the equatorial region from the LE spectrometer on the SEEP payload (ONR 804). The spinning motion of the CRRES satellite allows for simple mapping of the magnetosphere using the IMS-HI (ONR 307-8-3) neutral spectrometer. This instrument covers the energy range from 20 to 1000 keV and uses a 7 kG magnetic field to screen out protons less than about 50 MeV. ENA and the resulting low-altitude ion belt have been observed with the IMS-HI instrument. Recently, an advanced spectrometer (SEPS) has been developed to image electrons, ions, and neutrals on the despun platform of the POLAR satellite ( $\sim 1.8 \times 9$  Re) for launch in the mid-90's as part of the NASA ISTP/GGS program. For this instrument a 256 element solid state pixel array has been developed that interfaces to 256 amplifier strings using a custom 16 channel microcircuit chip. In addition, this instrument features a motor controlled iris wheel and anticoincidence electronics.

### 2. INTRODUCTION

Energetic neutral atoms are an important tracer of energetic ion collisions with neutrals in solar and planetary plasmas<sup>1</sup>. Global scale images of the earth's ring current ( $2 < L < 4$ ) may be remotely sensed from either above the earth's radiation belt<sup>2</sup> or from below the radiation belt at low altitude<sup>3</sup>. Neutral atoms can therefore provide a mapping of the internal composition, spatial geometry, and temporal changes of the ring current, weighted by the appropriate cross sections and neutral hydrogen density; it provides a powerful method of studying the magnetosphere.

The source of energetic neutral atoms (ENA) is believed to be a double-charge-exchange process of ions originating in the ring current<sup>4,5</sup> as shown in

Figure 1. The trapped ions of the ring current, by charge exchange with thermal hydrogen atoms of the geocorona, become high velocity neutral atoms which are focused, for those directed toward the earth, in the equatorial atmosphere where they again become ions by ionization collisions. The injected energetic neutrals at low altitudes produce the equatorial precipitation zone and a temporary low altitude ion belt between 200 and 1000 km as illustrated in Figure 1.

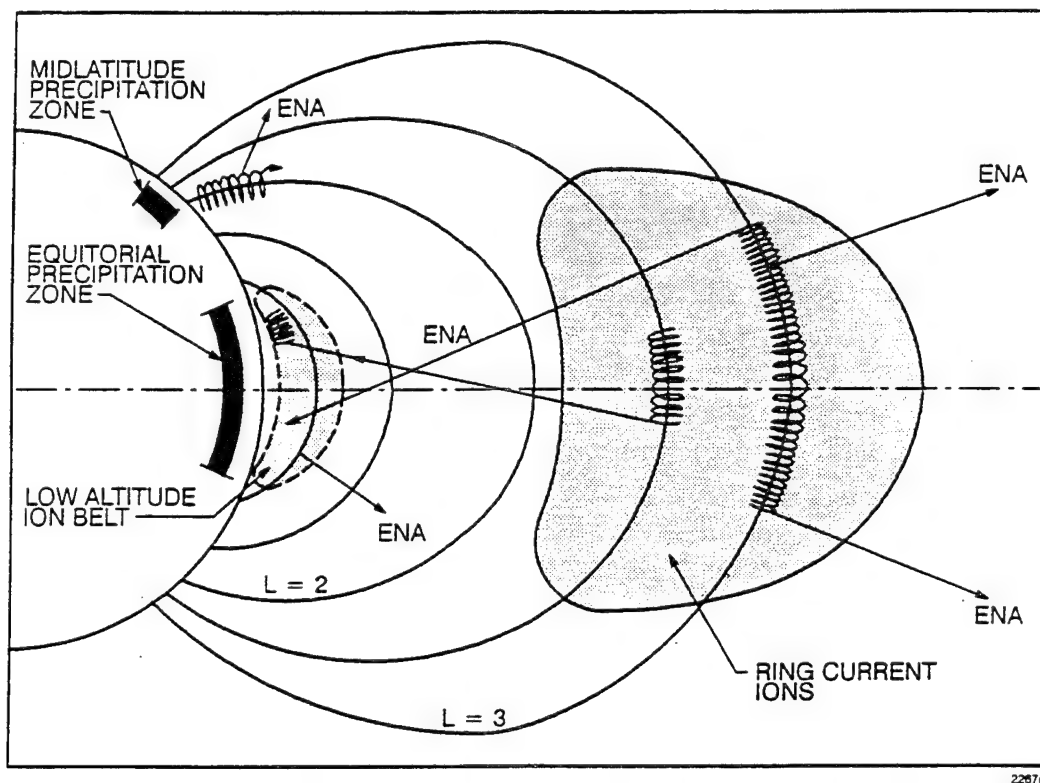


Fig. 1. Schematic representation of the ENA and resulting low altitude ion belt and precipitation.

### 3. RING CURRENT NEUTRALS AT LOW-ALTITUDE

The low-altitude ion belt cannot be the result of stably trapped particles since the ion lifetime is much less than the drift period. Figure 2 shows the equatorial zone of particle precipitation<sup>6</sup> as it appears in satellite measurements of particles by Hovestadt et al.<sup>7</sup>, Moritz<sup>4</sup>, Mizera and Blake<sup>8</sup>, Butenko et al.<sup>9</sup>, Scholer et al.<sup>10</sup>, and Meier and Weller<sup>11</sup>. The intensities have been normalized to unity at the maximum. The data were taken during moderately disturbed times. The zone typically covers the region of  $\pm 20$  degrees in latitude from the geomagnetic equator.

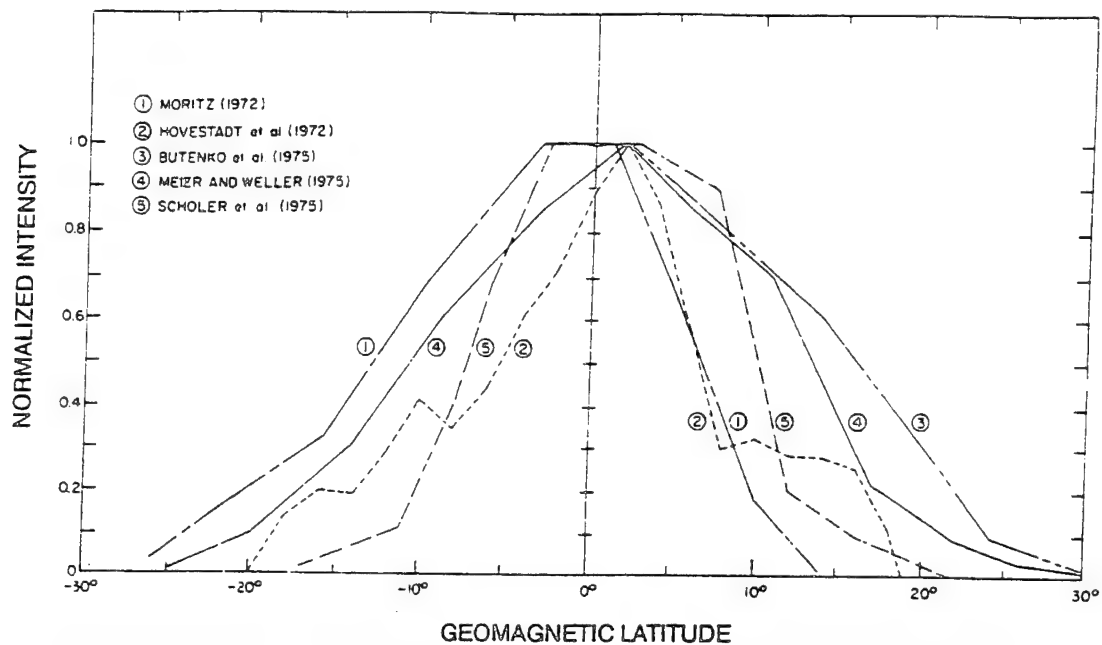


Fig. 2. The nighttime equatorial zone as it appears in satellite observations of particle flux and UV airglow. The intensity is normalized to the maximum value [6].

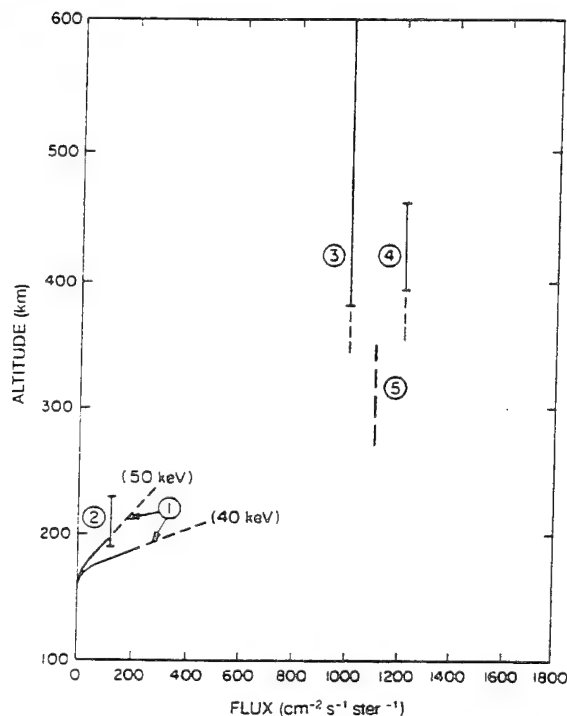


Fig.3. Rocket and satellite data of ions and neutrals at the equator. 1 is from Voss and Smith<sup>12</sup>, 2 is from Butenko et al.<sup>9</sup>, 3 is from Moritz<sup>4</sup>, 4 is from Mizera and Blake<sup>8</sup> and 5 is based on the S81-1/SEEP data after the 13 July 1982 magnetic storm.

Low altitude rocket<sup>12</sup> and satellite measurements<sup>4</sup> at the equator (Figure 3) indicate that the ions are concentrated at 90° pitch angle with an altitude profile which increases rapidly in intensity between 180 and 260 km and becomes nearly independent of altitude thereafter. Because the loss process for ions increases with atmospheric density the source must also increase with atmospheric density to maintain a constant flux profile between 300 and 1000 km. The inferred source mechanism is the charge exchange process of ring current ions which is illustrated in Figure 1. The low altitude energy spectrum is similar to that of the ring current, with most of the particles having energies between  $10 < E < 100$  keV and with the spectrum extending above 1 MeV. The precipitation rate is on the order of  $10^{-3}$  ergs  $\text{cm}^{-2} \text{s}^{-1}$ .

#### 4. S81-1 SATELLITE OBSERVATIONS

From May to December 1982, the SEEP payload on the three axis stabilized S81-1 polar satellite made high sensitivity measurements of precipitating energetic electrons and ions in the altitude region 170 to 270 km. The payload included an array of passively cooled solid-state detectors<sup>13</sup> covering the energy range from 2 to 1000 keV in 256 channels. The sensors had a geometrical factor of 0.17 cm<sup>2</sup>ster and a field-of-view of  $\pm 20^\circ$ .

The SEEP data during the 13 - 14 July magnetic storm<sup>14</sup> is shown in Figures 4 and 5. The prominent equatorial zone is observed between geomagnetic latitudes of  $\pm 20^\circ$  and is stable and repeatable in form during each equatorial pass. The twin peaks in the ion flux (i.e. maxima displaced  $\pm 10^\circ$  in latitude about the geomagnetic equator) are consistent with the north and south side lobes of the temporary ion radiation belt (Figure 1).

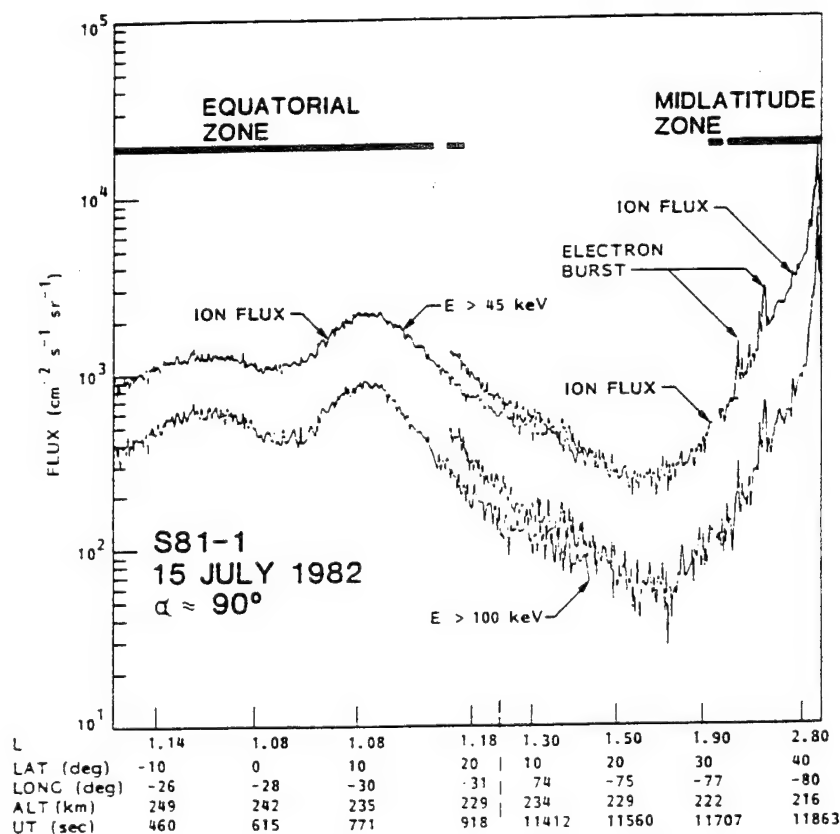


Fig. 4. Low altitude S81-1/SEEP satellite observations of precipitating energetic particles in the midlatitude and equatorial zones [14].

The temporal variations of ions in the equatorial zone are shown in the top panel of Figure 5. In the center panel the L shell variation of the plasma trough location and the equatorward auroral boundary (EAB) location are shown and indicate the relative compression of the magnetosphere and the displacement of the auroral zone to middle latitudes. The magnetic indices Kp and Dst are shown in the lower panel. Near 01:00 hours UT on 14 July 1982 the storm reaches a maximum ( $D_{st} = -325$ ) and the equatorial zone ion flux is observed to simultaneously increase by a factor of about 500 over pre-storm levels. The energetic equatorial neutrals and ions, however, remain high ( $\sim 10^3 \text{ cm}^{-2} \text{ s}^{-1}$ ) after the storm and confirm the development of a low latitude ( $L \sim 1.14$ ) ion radiation belt during the storm main phase that decays relatively slowly in time producing the equatorial zone ionization. The similarity of the day and night intensity and slow temporal variation of energetic particles in the equatorial zone indicate the global extent of ion precipitation.

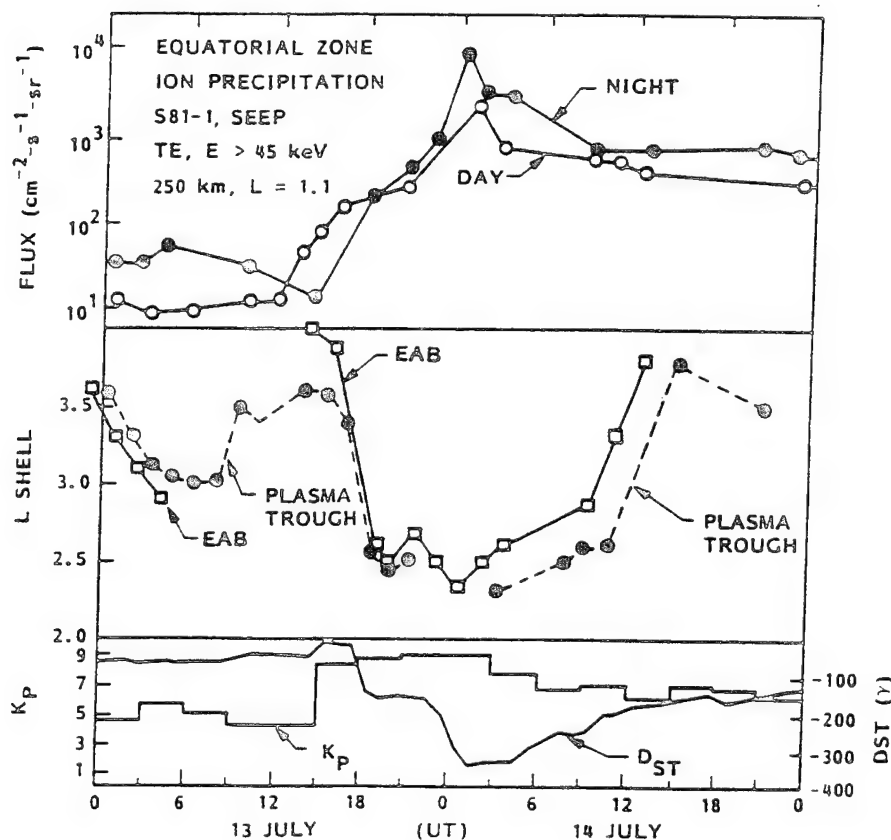


Fig. 5. Variation of equatorial zone ENA/ion precipitation during the magnetic storm of 13-14 July 1982. The location of the plasma (EAB) are also shown [14].

## 5. CRRES ION MASS AND NEUTRAL ATOM SPECTROMETER

The contiguous mapping of the particle distribution by the CRRES satellite over the radial distance range from 400 km to 5.5 Re near the equatorial plane provides a comprehensive data base that can be used for studies of the radiation belt and ring current. The primary objective of the medium energy ion mass spectrometer (IMS-HI) on the CRRES satellite was to obtain the necessary data to construct models of the energetic ion ( $10$  to  $2000$  keV-AMU/ $q^2$ ) and neutral atom ( $10$  to  $1500$  keV) environment of the Earth's radiation belts. The spectrometer<sup>15</sup> measured the energetic ion composition, energy spectrum, charge, and pitch angle distribution with good mass, temporal, and spatial resolution. Additionally simultaneous mass and energy analysis at relatively large geometrical factors ( $10^{-3}$  to  $10^{-2}$  cm<sup>2</sup>ster) was obtained.

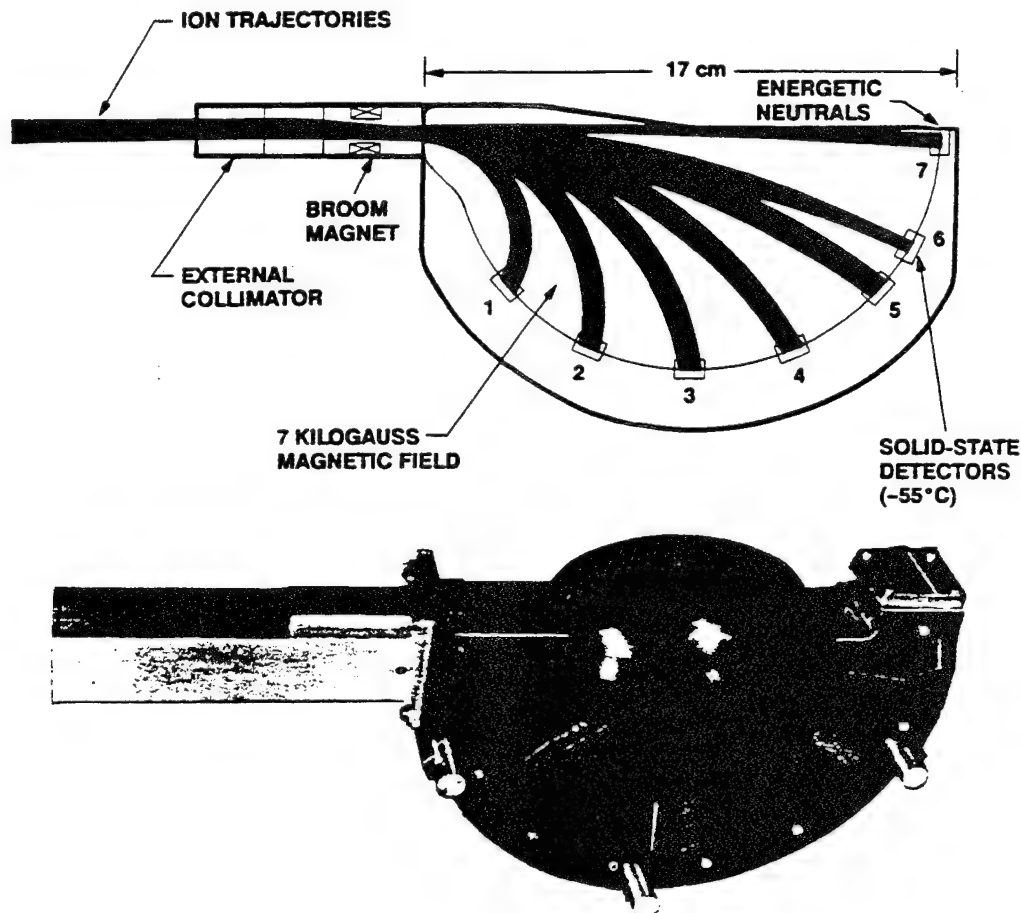


Fig. 6. The IMS-HI instrument on CRRES uses ion momentum, mass defect, and energy analysis from a 7 kG magnet and an array of cooled solid-state detectors. The magnet is shown in the lower portion of the figure and the ENA and ion optics in the upper portion.

The instrument principle of operation is illustrated in Figure 6 and is based on ion momentum separation in a 7kG magnetic field followed by energy and mass defect analysis using an array of cooled ( $-50^{\circ}\text{C}$ ) silicon solid-state detectors. The entrance collimator consists of a series of rectangular baffles that define the ion and neutral beam angular resolution and a broom magnet to reject electrons with energy less than 1 MeV. A seventh sensor, located directly in line with the collimator, measures energetic neutrals and has an ion rejection of approximately  $50 \text{ MeV-AMU}/q^2$ . In principal the spin of the satellite and orbit motion can be used to "raster scan" a portion of the magnetosphere to obtain a neutral atom image. In practice, however, the duty cycle associated with the spinning of the satellite and the background of the radiation belts make this a difficult task from CRRES.

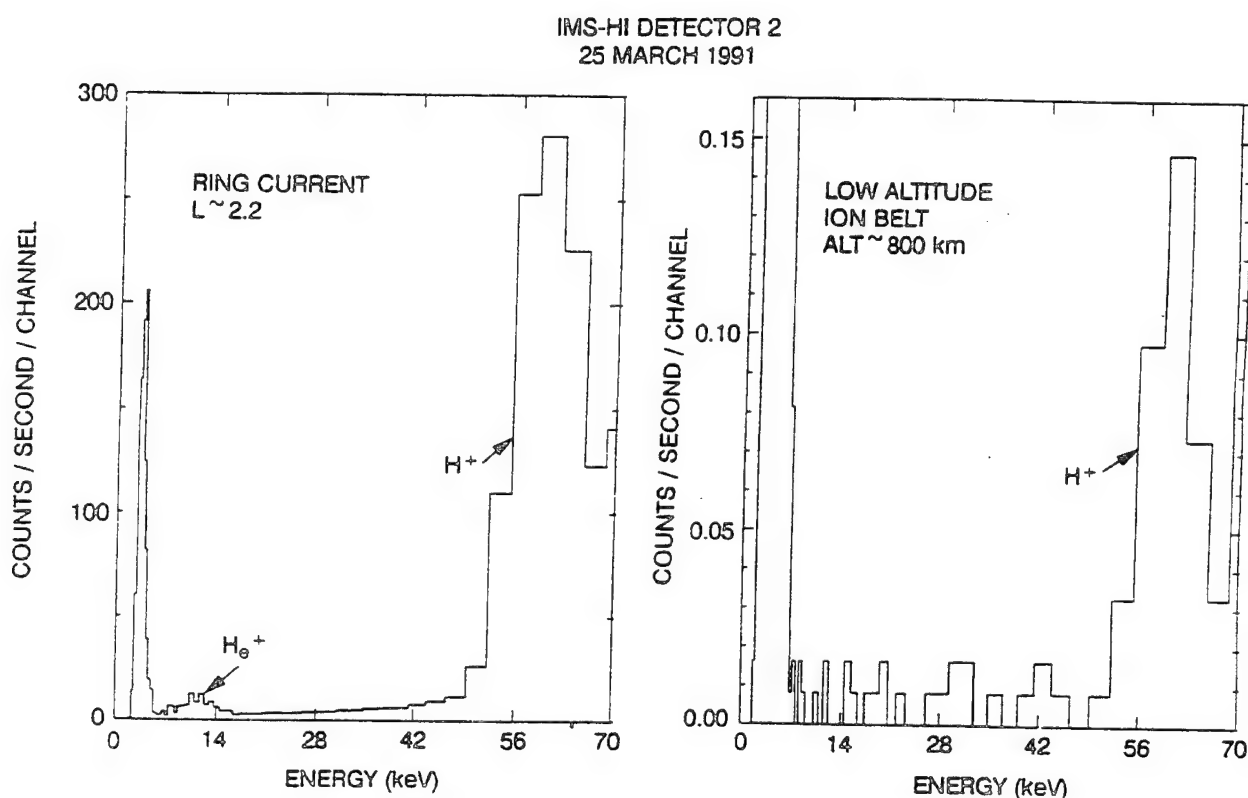


Fig. 7. Mass spectrograms on 25 March 1991 from the IMS-HI instrument on CRRES of the low altitude ion belt which is understood to be the result of ENA and the associated ring current mass spectrogram at  $L \sim 2.2$ .

Near perigee ( $<1000\text{km}$ ), when CRRES is below the inner belt, the IMS-HI instrument is able to directly view the ring current neutrals and ion composition of the low-altitude ion belt. Above the inner belt the IMS-HI instrument is able to make cross-sectional cuts of the ring current ion composition. About one day after the large magnetic storm of 24 March 1991 the ring current ions were



observed to increase and move to lower altitudes. The ring current flux at this time extends down to  $L \sim 2.0$  and is dominated by hydrogen at  $E \sim 60$  keV.  $O^+$ ,  $O^{++}$ , and  $He^+$  are one to two orders of magnitude less in flux at these energies.

The ENA transported to low altitude is again charge exchanged by the atmosphere and temporarily becomes the low-altitude ion belt. Because the ions cannot support drift motion in much of the belt the loss rate is high. The steady-state ion population to first order is a mapping of the source composition multiplied by the appropriate atmospheric loss rates. A mass spectrogram of the low altitude ion belt for detector two is shown for the first time in figure 7 for 25 March 1992. Also shown for comparison is the mass spectrogram of detector two near the inside edge of the ring current at  $L \sim 2.2$ . At this time the prominent ion, inferred from the ring current ENA is  $H^+$  at 60 keV. The average low-altitude hydrogen count rate is about 2000 times lower than the average count rate in the ring current for the IMS-HI spectrometer.

## 6. SEPS ENERGETIC PARTICLE IMAGER

SEPS (Source-Loss/Cone Energetic Particle Spectrometer) is to be flown in the mid-90's on the POLAR Satellite in the NASA ISTP Program. Because SEPS is mounted on the POLAR spacecraft despun platform and is capable of imaging particles over a  $24^\circ \times 48^\circ$  field-of-view in the nadir and zenith directions the particle "source cone" and "loss cone" can be monitored continuously and simultaneously. In addition, over the polar caps, SEPS will be able to image ENA.

The ion/neutral telescope on SEPS has 128 XY pixel elements over a  $1 \text{ in}^2$  by 200 micron deep solid state detector. A strong broom magnet rejects electrons from the entrance collimator of the SEPS pinhole camera. A SiLi detector behind the XY detector is used for anticoincidence. The instrument is designed to cover the energy range from 30 keV to 10 MeV.

In addition to the SEPS ion/neutral telescope the "electron" telescope of SEPS can measure ions and neutrals above 300 keV in 256 pixels over  $2 \text{ in}^2$ . For this telescope a motor driven iris can change the aperture size upon command thereby optimizing the instrument's geometrical factor and associated spatial resolution. Unique electron, ion, and neutral particle images are expected with 100% duty cycle. The SEPS instrument mass is 3.4 kg, the power consumption 3.5W, and the telemetry rate is 1.2 kbps.



## 7. ADVANCED MICROCIRCUIT TECHNOLOGY FOR IMAGING SPECTROMETERS

State-of-the-art sensors and electronics are required on future instrumentation to perform energetic particle imaging and spectroscopy within spacecraft resources. Neutral atom imaging requires large geometrical factor sensors with multi-pixels and good background rejection. Background rejection can be improved by using anticoincidence detectors (as in SEPS), electric and magnetic field deflectors in the optical path, coincidence time-of-flight techniques, and coded aperture devices to improve signal-to-noise.

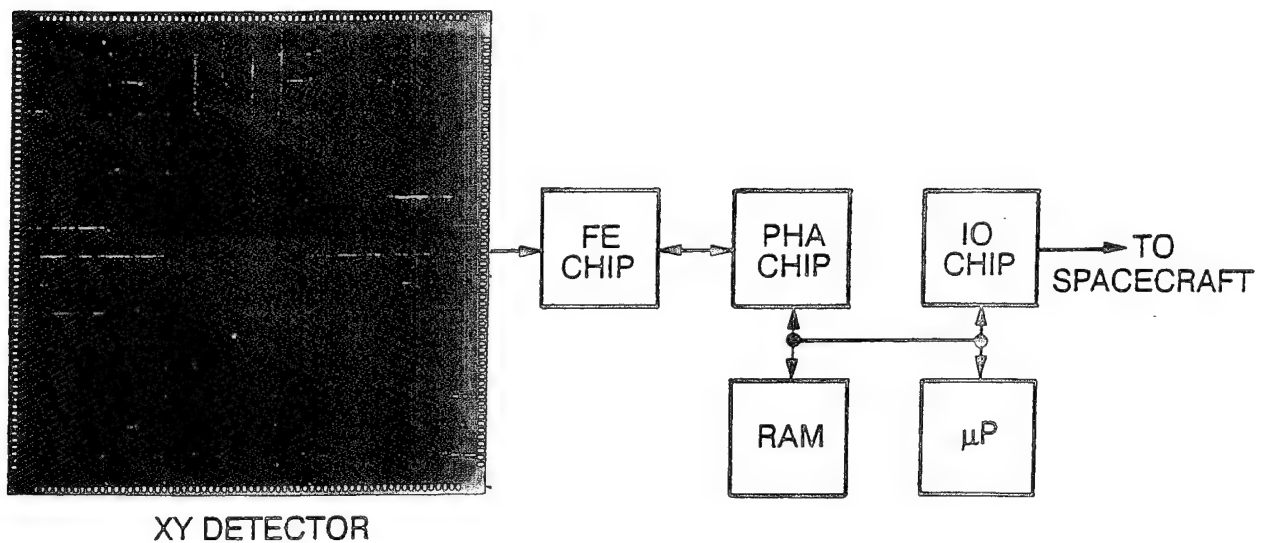


Fig. 8. System block diagram of an advanced microcircuit detector and analog/digital microchips to spectroscopically image energetic particles.

A recent review of instrumentation techniques for the remote sensing of space plasmas in the heliosphere via energetic neutral atoms has been presented by Hsieh et al.<sup>1</sup> Much of the proposed new instrumentation is based on rather sophisticated sensor electronics demands. To simplify instrument development and greatly reduce instrument spacecraft resource requirements the development of advanced microcircuits, solid-state detectors, and microchannel plate sensors have been pursued. Figure 8 illustrates the key modules which have been developed as part of the SEPS program.

To minimize capacitance (i.e. low energy threshold) and crosstalk a 1 in<sup>2</sup> by 200 micron thick solid state sensor was developed with Hamamatsu Inc. that has 256 pixels with individual readouts (Figure 8). The proton dead zone for this

device was found to be 8 keV and has an energy resolution at room temperature of 2 keV FWHM.

Thousands of sensor elements require microcircuit technology to amplify and process the data. To achieve this an advanced CMOS mixed mode (combined analog and digital) gate array microcircuit was developed that is radiation hard. A gate array is a matrix of transistors on a microcircuit that can be interconnected for unique circuit functions. Because the matrix is mass produced and well characterized (semi-custom) the risk, cost, and turnaround are significantly reduced compared to a full custom microcircuit. The arrays are highly reliable since they significantly reduce the number of bonds and PC board parts and permit a parallel system architecture.

The first circuit developed on the rad-hard array (Figure 8) is a 16 channel amplifier chip that features; 1) 0.5 microsecond shaping, 2) peak detection, 3) 32 individual comparators with D to A control, and 4) coincidence and anticoincidence logic. To date, a single channel version of this chip has been tested. The input preamplifier is designed to work with a microchannel plate or sensor in a DC coupled mode to a solid state detector.

The second circuit developed is a pulse height analyzer (PHA) chip that can accumulate counts in an external RAM according to energy and position. It also includes eight 17 bit counters and a 16 level flash A to D converter for log or linear analysis.

The third chip features the necessary IO functions to interface with the spacecraft and the onboard microprocessor. Some of the features of the IO circuit include 1) 8-bit D to A converter with calibrate pulse output, 2) eight multiplexed inputs to a 8 bit A to D converter, 3) interrupt controller, 4) 16-bit counter timer, 5) address decoding, 6) parallel port, 7) serial port, and 8) internal clock processing.

## 8. CONCLUSIONS

Global geospace cannot be effectively observed by multiple *in situ* measurements. The dynamics of the ring current are only partially understood [16]. The ability to remotely sense the heliosphere via ENA may significantly improve our understanding of the large scale dynamics of planetary magnetospheres and shocks. Many rocket and satellite measurements to date have indicated the credibility of ENA and the resulting low-altitude ion fluxes. The recent CRRES data has now made it possible to compare the ion composition of the ring current with the energetic neutrals and the resulting ion composition at low altitudes.

Future instrumentation must be carefully designed to maintain a large geometrical factor with a high background rejection capability. Although the SEPS instrument geometrical factor is small, its ability to stare at the ring current when over the polar cap for several hours will improve the signal-to-noise ratio.

The implementation of several new technologies makes ENA imaging an attractive diagnostic tool for mapping the global particle environment.

## 9. ACKNOWLEDGMENTS

The work at Lockheed was supported in part by the Office of Naval Research under contract N00014-83-C-0476 and by the Lockheed Independent Research Program. We thank all of our colleagues at LPARL who have contributed to the various programs mentioned above. In particular we thank Dr. J.R. Kilner and Mr. R.A. Baraze for their efforts in the development of the SEPS instrument and microcircuits.

## 10. REFERENCES

1. K.C. Hsieh, C.C. Curtis, C.Y. Fan, and M.A. Gruntman, "Techniques for the Remote Sensing of Space Plasma in the Heliosphere via Energetic Neutral Atoms: a Review", in press, 1992.
2. E.C. Roeloff, D.G. Mitchell, and D.J. Williams, "Energetic Neutral Atoms (5-50 keV) from the Ring Current, Imp 7/8 and ISEE-1", J. Geophys. Res., 90, 10991-11008, 1985.
3. H.D. Voss, W.L. Imhof, and J. Mobilia, "Satellite Observations of Energetic Ions and Neutrals in the Equatorial Precipitation Zone", Proceedings Yosemite '84 Planetary Plasma Environments: A Comparative View, ed. C.R. Clauer and J.H. Waite, Jr., 95-96, 1984.
4. J. Moritz, "Energetic Protons at Low Altitudes: A Newly Discovered Radiation Belt Phenomenon and its Explanation", Z. Geophys., 38, 701, 1972.
5. B.A. Tinsley, Neutral Atom Precipitation- a Review, J. Atmos. Terr. Phys., 43, 617, 1981.
6. H.D. Voss and L.G. Smith, "Global zones of energetic particle precipitation", J. of Atmos. and Terr. Phys., 42, 227-239

7. D.B. Hovestadt, B. Hausler, and M. Scholer, "Observations of energetic particles at very low altitudes near the geomagnetic equator", *Phys. Rev. Lett.*, 28, 1340-1344, 1972
8. P.F. Mizera and J.B. Blake, "Observations of Ring Current Protons at Low Altitudes", *J. Geophys. Res.*, 78, 1058-1062, 1973.
9. V.D. Butenko, O.R. Grigoryan, S.N. Kuznetsov, G.S. Malkiel, and V.G. Stolpyskii, "Proton Currents with  $E_p > 70$  keV at Low Altitudes in the Equatorial Region", *Kosmicheskie Issledovaniya*, 13, 508-512, 1975.
10. M. Scholer, D. Hovestadt, and G. Morfill, "Energetic  $\text{He}^+$  Ions from the Radiation Belt at Low Altitudes Near the Geomagnetic Equator", *J. Geophys. Res.*, 80, 80-85, 1975.
11. R.R. Meier and C.S. Weller, "Observations of Equatorial EUV Bands: Evidence for Low-Altitude Precipitation of Ring Current Helium", *J. Geophys. Res.*, 80, 2813-2818, 1975.
12. H. D. Voss and L.G. Smith, "Rocket Observations of Energetic Ions in the Nighttime Equatorial Precipitation Zone", *COSPAR Advances in Space Exploration*, 8, 131-134, 1979.
13. H.D. Voss, J.B. Reagan, W.L. Imhof, D.O. Murray, D.A. Simpson, D.P. Cauffman, and J.C. Bakke, "Low Temperature Characteristics of Solid State Detectors for Energetic X-ray, Ion and Electron Spectrometers", *IEEE Trans. Nucl. Sci.*, NS-29, 164-168, 1982.
14. H.D. Voss, W. L. Imhof, J. Mobilia, E. E. Gaines, and J. B. Reagan, "Energetic Particles in the Nighttime Middle and Low Latitude Ionosphere", *Adv. Space Res.*, 5, 175-178, 1984.
15. H.D. Voss, E. Hertzberg, A.G. Ghielmetti, S.J. Battel, K.A. Appert, B.R. Higgins, D.O. Murray, and R.R. Vondrak, "The Medium Energy Ion Mass and Neutral Atom Spectrometer (ONR-307-8-3)", in press, *J. Spacecraft and Rockets*, 1992.
16. D.J. Williams, "Dynamics of the Earth's Ring Current: Theory and Observations", *Space Sci. Rev.*, 42, 375, 1985.

## Appendix 4

### Narrow Flux Dropouts in the Outer Radiation Belt

Narrow Flux Dropouts in the Outer Radiation Belt. Association With Waves and  
Magnetic Fields

W. L. Imhof, H. D. Voss\*, J. Mobilia, H. L. Collin  
Lockheed Palo Alto Research Laboratory  
Palo Alto, California

J. R. Wygant\*  
Space Sciences Laboratory  
University of California, Berkeley, California

R. R. Anderson  
Department of Physics and Astronomy  
University of Iowa, Iowa City, Iowa

H. J. Singer  
NOAA R/E/SE  
Space Environment Laboratory  
Boulder, Colorado

Abstract

An investigation has been made of localized decreases and increases (dropouts) in energetic particles within the radiation belt (up to 3 orders of magnitude) and their correlations with the intensities of VLF waves and changes in the geomagnetic field. The study was performed with measurements from the CRRES satellite which covered a wide range of L shells at near equatorial positions. At the times of some of the flux dropouts the VLF waves were enhanced and the magnetic fields changed. The CRRES measurements of flux variations with L shell indicate that if the flux decreases were produced by a radial shift of the particle population large spatial movements would have been required in some cases. The investigation emphasized narrow observation time dropouts near midnight with widths of only a few minutes well within the trapped population and at L shells as low as 5.4. Dropouts were often associated with substorms identified by AKR observation.

\* Now at Taylor University, Upland, Indiana

+ Now at University of Minnesota, Minneapolis Minnesota

January 25, 1995

## Narrow Flux Dropouts in the Outer Radiation Belt, Association With Waves and Magnetic Fields

### Introduction

At synchronous or near-synchronous orbit long duration decreases in the fluxes of energetic electrons and protons have been observed followed by very rapid increases (e.g. Walker et al., 1976, Sauvaud and Winckler, 1980, Baker and McPherron, 1990, Baker et al., 1993, Nakamura et al., 1994, Nagai, 1982, Erickson et al., 1979). Many of these decreases have been interpreted as resulting from motion of the trapped particle outer boundary whereas the subsequent flux recoveries have been found to be associated with the expansion phase onset of magnetospheric substorms. Most of these observations have been made from a satellite that remains at the same geosynchronous radial distance which is nominal  $L = 6.6$ . In addition, narrow flux dropouts have been observed both at synchronous altitude (Su et al., 1976, Sergeev et al., 1992) and on lower  $L$  shells (Yeager and Frank, 1969; Kaufmann et al., 1972; Korth et al., 1994).

Broad dropouts with slow decreases followed by rapid increases are commonly observed from synchronous-orbit satellites and are believed to be associated with geomagnetic substorms. On the other hand, narrow dropouts at lower  $L$  values have not been as thoroughly studied and their source mechanism(s) is (are) not as well understood as the wider events. No events have been extensively studied with a wide range of correlated measurements. For example, waves are known to cause particle precipitation from the radiation belts through wave-particle interactions and yet they have not been investigated as the cause of flux dropouts. Based on the known interaction strengths and characteristics of the dropouts it is not likely that they are caused by such processes, but VLF waves may still play an important role in the formation of dropouts.

Our knowledge of flux dropouts can be improved by examining the measurements from a satellite such as CRRES (Combined Release and Radiation Effects Satellite) which has a highly eccentric nearly equatorial orbit. Such an orbit provides one the opportunity to investigate the radial flux profiles associated with dropouts as well as to survey their occurrence over a wide range of  $L$  shells. The CRRES satellite provides a wide variety of particle, wave, and magnetic field data important for investigations of the dropout phenomenon. In



January 25, 1995

this paper, for the first time such a complete set of data is presented in investigation of particle dropouts in the outer radiation belt.

### Instrumentation

The CRRES satellite was launched on July 25, 1990 into an orbit with an apogee of 35,786 km, a perigee of 350 km, and an inclination of  $18^\circ$ . Apogee at launch was at about 08:00 local time, and the spacecraft precessed toward earlier local times at a rate of about 15 hours per year. The satellite spin axis was kept pointing within 15 degrees of the sun.

The particle data used here were acquired with the ONR 307 payload on CRRES. One of the instruments in the payload, the Spectrometer for Electrons and Protons (SEP), had a fine angular resolution ( $\pm 1.5^\circ$ ); measured energy spectra over range 40 keV to 5 MeV for electrons; and had silicon solid-state detectors oriented at  $80^\circ$ ,  $60^\circ$ , and  $40^\circ$  to the satellite spin axis (Nightingale et al., 1992). The electron data presented here are also from the IMS-LO spectrometer in three broad energy bands centered at 1.7, 3.9, and 8.9 keV at  $75^\circ$  to the satellite spin axis and with an angular resolution of  $\pm 2.5^\circ$  (Collin et al., 1992). Further details on these electron spectrometers are available in the referenced papers.

The IMS-HI instrument (Voss et al., 1992) measured the energy spectra and pitch angle distributions of ions and neutral particles from a few tens of keV to a few hundred keV. The IMS-HI instrument was based on ion momentum separation in a magnetic field followed by mass defect (variation with particle mass in the ratio of signal strength to energy deposition in the sensor) separation and energy analysis. An array of seven cooled ( $-50^\circ\text{C}$ ) solid-state sensors was used. After exiting the collimators, ions entered a 7000-G magnetic field where they were deflected ( $mv/qB$ ) onto the sensors. The instrument featured simultaneous mass and energy analysis at relatively large geometric factors (between  $10^{-3}$  and  $10^{-2}\text{ cm}^2\text{ sr}$ ). The look direction from the spin axis was  $75^\circ$  with a pitch angle resolution of  $\pm 2^\circ$ . The energy ranges for the ions used here were: 15 to 2000 keV for  $\text{H}^+$  and 14 to 500 keV for  $\text{He}^+$ .

The AC electric and magnetic field data used in this study were provided by the University of Iowa/Air Force Geophysics Laboratory (AFGL) Plasma Wave Experiment and the University of California at Berkeley/AFGL Electric Field/Langmuir Probe Experiment. The Iowa/AFGL instrument included a

January 25, 1995

sweep frequency receiver and multichannel spectrum analyzer which together provided AC electric field measurements from 5 Hz to 400 kHz and magnetic field measurements from 5 Hz to 10 kHz (Anderson et al., 1992). The Berkeley/AFGL experiment (Wygant et al., 1992) measured electric and magnetic waveforms over frequencies ranging from quasistatic to 40 kHz. The instrument also provided continuous monitoring at several samples per second of the wave amplitudes measured through 3 broadband filters with maximum response at frequencies of 32 Hz, 256 Hz, and 2048 Hz.

The CRRES Fluxgate Magnetometer made 3-axis measurements of the magnetic field at 16 samples/sec (Singer et al., 1992). The least significant bit resolution from each sensor independently was approximately 0.4 nT in a field less than about 900 nT and was about 22 nT when the field was greater than approximately 900 nT. Therefore, during approximately 8 hours out of the 10 hour CRRES orbit, when CRRES was beyond about 3.5  $R_E$ , the instrument provided high resolution measurements. To limit magnetic interference from the spacecraft, the instrument was mounted on a 6.1 m Astromast boom. The magnetometer analog electronics were connected to the Electric Field/Langmuir Probe experiment for power, signal processing, and telemetry formatting.

### Observations

The SEP data set (from August 1990 to early October 1991) was surveyed for pronounced dropouts in the energetic electron fluxes within the outer radiation belt. At the times of such events proton,  $He^+$ , and lower energy electron data from other detectors in the CRRES payload were examined. In this paper samples of these events are provided. First, an example is presented of a broad duration dropout similar to those reported from synchronous orbit observations. Later we primarily consider dropouts with short observation times. The correlated wave and magnetic field data are also presented.

In the top section of Figure 1, for orbit 259 on 9 November 1990, the fluxes of electrons at various energies (1.7 keV, 3.9 keV, and 8.9 keV) and at 30° (or equivalently 150°) pitch angle are plotted versus time and the associated satellite ephemeris parameters, listed at the bottom of the figure. Electrons in the outer radiation belt with such equatorial pitch angles have a mirror point altitude of approximately 20,000 km and therefore do not mirror near the atmospheric loss cone nor near the equator. In the next lower section are plotted the fluxes of electrons at 53, 100, 171, and 265 keV and at 30° (150°) pitch angle. Below the

January 25, 1995

electron data are plotted the electric field wave intensities at three different frequencies from the Berkeley instrument. At the time of the electron flux decreases the wave intensities are observed to become strongest when the flux recovery occurred. In the next lower section of the figure the fluxes of protons at 18, 56, 140, and 360 keV over the full range of pitch angles are plotted for the same time interval. In the bottom section of Figure 1 are plotted the fluxes of  $\text{He}^+$  at 35, 90, and 300 keV. The various energy electrons, protons and  $\text{He}^+$  particles all have a relatively gradual decrease followed by a more abrupt increase. Such a shape is similar to that of the dropouts previously reported at synchronous altitude. In this case, the 53 keV electron flux drops by about 3 orders of magnitude over the L shell range 6.0 to 6.8.

Selected energetic electron, proton and  $\text{He}^+$  particle fluxes for orbit 259 are plotted in the top section of Figure 2. The bottom section contains a spectrogram (frequency versus time with a color coding for intensity) from the Iowa electric field wave data during the satellite pass. If wave-particle interactions involving the electromagnetic electron cyclotron resonance are important and assuming the interaction between electrons and waves is via parallel-propagating whistler mode waves then we would expect an inverse relation between the wave frequency and the electron energy. The emission that fell from about 1 kHz to 20 Hz between 0655 UT and 0705 UT may well be associated with the low energy electron flux decreasing before that of the higher energy electrons. The hiss-like band that rises from about 500 Hz at approximately 0705 UT to about 4 kHz at around 0750 UT has a weaker extension that began falling from about 5 kHz at 0645 UT down to the 500 Hz range at 0705 UT. An enhanced AKR wave band with a central frequency of  $\sim 300$  kHz appears at  $\sim 0730$  UT and is a remote indication of a substorm. However, the AKR is not a local occurrence and is thus not directly related to in situ measurements of particles. The hiss-like waves discussed above are enhanced in the few hundred Hz to few kHz range from 0730 UT to 0750 UT around the time of the return of the flux. However, the most intense emission is in the 5 Hz to 200 Hz range from about 0736 UT to 0740 UT.

In contrast with the flux patterns shown in Figures 1 and 2 a very sharp decrease soon followed by an abrupt increase is shown in Figure 3 for orbit 186 on 10 October 1990. The format of Figure 3 is the same as that of Figure 1. Similar narrow decreases appear in several of the electron channels, the two lowest energy proton channels and the two lowest energy  $\text{He}^+$  channels. At the beginning of the flux decrease the electric field intensities increased, but other than that there was no obvious correspondence with the flux profiles.

January 25, 1995

A color spectrogram of the Iowa wave data from orbit 186 is shown in the bottom section of Figure 4. In the top section are plotted selected particle fluxes. At the time of the narrow flux dropout the wave data at frequencies up to a few kHz were enhanced but the association with the flux variations is not so evident in this case.

Each of the narrow and broad dropouts selected from the survey of the CRRES data is listed in Table 1. All of the narrow dropouts in the list had durations of less than 30 minutes. The broad dropouts, with durations of greater than or equal to 30 minutes, had slow flux decreases followed by rapid recoveries. The table lists several quantities associated with the start of recovery from the dropout: UT in hours, UT in seconds, MLT, L,  $K_p$ , Dst, and  $B/B_0$  where  $B_0$  is the magnetic field strength at the equator. The table indicates whether the dropout also occurred in the ions and if so whether it was comparable in shape to that of the electrons. Also listed is the L value at the nearest location with the same measured flux as at the dropout, the highest L value reached on the satellite pass, and the minimum L interval between either of these quantities and the L value at the start of recovery. The list indicates the number of narrow dropouts within one hour of recovery from the dropout of concern. The presence of VLF wave enhancements is provided as well as whether, if they occur they are narrow, broad or delayed. The presence of AKR radiowaves at  $\sim 10^5$  Hz is also indicated and suggests substorm activity. For most of the narrow and broad dropouts VLF waves were generally enhanced in the time vicinity of the event.

Time profiles of the 256 Hz wave intensities are compared with those for the 56 keV proton fluxes for two narrow dropouts, Figure 5, and wide dropouts, Figure 6. In these examples the energetic electron and 56 keV proton fluxes had similar shaped dropouts. In the two broad dropout particle examples shown the wave intensities are greater at the times of the electron flux recoveries and therefore wave-particle interactions may have played a significant role during this phase. In previous investigations of wave-particle interactions with the CRRES data (Imhof et al., 1992, 1994) for energetic electrons and  $\sim 100$  Hz waves it was found that the primary change in the electron pitch angle distributions was in and about the loss cone. From a survey of pitch angle distributions for the dropouts considered in this paper it was found that the fluxes at pitch angles away from the loss cone did not appear to undergo significant changes. Correlations occur between wave intensities and the narrow dropouts in the examples shown but are not as pronounced as in the wide dropouts shown.

January 25, 1995

During one orbit, 666, the wave intensity spectrogram and the fluxes of electrons at four energies are plotted in Figure 7 as a function of time during a portion of the orbit. Clearly, the VLF wave intensities display a narrow and pronounced increase at the time of the electron flux dropout ( $L \sim 6.75$ ). Other adjacent VLF intensifications show no association with dropouts.

In Figure 8 wave spectrograms are shown for four different satellite passes in which the wave intensities displayed pronounced enhancements. In all of these selected examples the wave intensity maxima occurred at the times of electron flux dropouts indicated by arrows. Also in the general time vicinity of the VLF wave enhancements there was an increase in the AKR intensities at  $\sim 10^5$  Hz.

The magnetometer measurements are now considered. The data used in this analysis were the observed magnetic field strengths minus a model field which is the sum of the Olson-Pfizer 1977 external model and the extrapolated IGRF 1985 internal model. With this procedure the magnetic field data were used in a manner which emphasizes time changes in the magnetic field strength during a satellite pass. In Figures 5 and 6 are shown the perturbations in the absolute field strengths and the  $z$  components of the field strength, where  $z$  is perpendicular to the ecliptic plane. The data indicate that, as reported by other investigators (e.g. Korth et al., 1994), flux dropouts are often associated with changes in the geomagnetic field.

The magnetic local times and  $L$  shell values of the various wide and narrow events observed are shown in Figure 9. The MLT values for many of the events were near local midnight, consistent with their association with magnetic substorms. It is also to be noted that whereas the CRRES satellite covered most  $L$  shells in the outer radiation belt the  $L$  values of many of the events were all close to the location of synchronous orbit satellites from which most such dropouts have been observed. In many of the wide examples shown the wave intensities were greater near the time of the flux recovery. Since many of the broad dropout flux patterns have been shown to be associated with substorms, one might speculate that the increases of wave activities in the frequency band 32 Hz to 2048 Hz were also associated with the expansion phase onset of a substorm.

The spatial versus temporal nature of the dropouts reported here may be addressed by examining data acquired over the same  $L$  shell locations, but at different times. The orbital parameters of the CRRES satellite were such that the  $L$  shell locations of the observed dropouts were sampled within two to three hours previously or subsequently. To search for repeated dropouts the fluxes of



January 25, 1995

53 keV electrons were plotted as a function of L and comparisons made between each portion of an orbit. In none of the cases did a dropout with a similar shape appear at times before and after apogee of the orbit. However, the examples without a repeated dropout do not necessarily preclude a spatial character with a duration of less than about two hours or with a limited longitude extent. Such a time interval is longer than the substorm process time and particle drift times.

The measured particle profiles were used to derive the shifts in L shell required to account for the dropouts. Figure 10 shows the differences in L shell ( $\Delta L$ ) for the same electron flux level at the dropout as in the nearest prolonged same flux level plotted as a function of L at the start of recovery of the dropout. In some cases the flux dropout counting rate was essentially at the instrument background level and the flux may have been nearly zero. In many cases the CRRES satellite did not reach positions beyond the trapping boundary or at appropriate flux levels: in such cases the  $\Delta L$  point is indicated with an arrow. Since the flux gradient at the trapping boundary is usually quite steep the plot would be nearly the same if the L value at the boundary were used. The plot shows that for at least one-third of the dropouts the value of  $\Delta L$  was greater than 0.5; in such cases a large radial shift would be required.

The left section of Figure 11 shows the ion fluxes measured during a 100 second interval around the narrow dropout observed during orbit 186. It was possible to obtain ion fluxes once every second, but without identification of the various ion components. Based on analyses of this interval with broader time resolution it was concluded that the detector response was primarily due to protons. The proton flux is observed to decrease by two orders of magnitude in less than one second at the onset of the dropout. The flux then increased again after  $\sim 10$  seconds to the pre dropout level in less than one second. Subsequently (within  $\sim 3$  seconds) the flux again decreased to the background level, followed by another rapid rise and fall in  $\sim 10$  seconds.

Because of the rapid flux variations observed in the ion fluxes during orbit 186 it is important to consider the corresponding magnetometer measurements on a fast time scale. Such a comparison is made in the right section of Figure 11. At the time of the flux dropout around 0734 UT, the magnetic field begins to become more stretched by about  $25^\circ$  and then becomes more dipolar as the dropout recovers. It is also important to note that the total field magnitude increases during the dropout which may result from the lack of a diamagnetic effect exiting the plasma sheet.

## Discussion

Long duration events followed by an abrupt recovery display flux versus time profiles which are similar to those previously observed at synchronous altitude. This class of flux variations has been interpreted as being associated with the occurrence of substorms (e.g. Baker et al., 1993). The standard AE indices at the times of the CRRES observations are not available, but during many of the dropouts with this characteristic radiowave enhancements at AKR frequencies of  $\sim 10^5$  Hz were observed at the times of the dropouts and it has been shown (Voots et al., 1977) that such waves can be used with good reliability to identify magnetic substorms provided the radio measurements are taken at appropriate positions. Optimum locations are on the nightside of the earth and at altitudes sufficiently far from the earth to avoid local propagation cutoff effects. The CRRES measurements presented here were generally taken at local nighttime and at distances from the earth of about 5 earth radii. We have concluded that to a fair approximation the AKR observations from CRRES should provide a good indication of the occurrence of a substorm. For each of the events observed in this investigation the presence or absence of AKR is indicated in Table 1. For the 8 broad duration dropouts selected on the basis of the energetic particle data the AKR response indicated the occurrence of a substorm in 7 of these events, or equivalently 87.5%.

Based on Explorer 12 observations Yeager and Frank (1969) concluded that narrow flux dropouts in the outer radiation belt are produced by the motion of a flux gradient past a satellite. In another paper using Explorer 12 data Kaufmann et al. (1972) presented evidence that plasma begins flowing rapidly away from the base of the tail during, or slightly before, the sudden expansion phases of substorms. In the present investigation the observations of AKR radiowaves indicate that a magnetic substorm occurred in 8 of the 18 narrow dropout events considered, but AKR data were not available for one of these events. The data, therefore, suggest that at least approximately 44% of the narrow dropouts within the radiation belt were associated with a magnetic substorm.

Various experimenters have considered a major cause of energetic particle flux dropouts in the outer radiation belt to be attributed to distortions of the magnetic field during substorms (e.g. Baker and McPherron, 1990). Magnetic field line changes were observed with the magnetometer on CRRES during many of the dropouts considered here. For example, the correlation between magnetic

January 25, 1995

field line directions and particle flux dropouts is very pronounced for the event observed on orbit 186 and displayed in Figure 11.

For the wide dropouts the measured  $z$  component of the magnetic field strengths increased consistently at the times of the flux recoveries. The increases in  $B_z$  are probably associated with the dipolarization of the field at substorm expansion onset and the field becomes more disturbed. The timing differences between the particle and field signatures are likely related to the location of CRRES relative to the onset location and the time it takes for the  $B$  field disturbance to propagate at Alfvén speeds versus the time it takes for particles of different energies to reach the satellite. The significant changes in the magnetic field at the times of many of the recoveries are consistent with the findings of Baker and McPherron (1990).

Kaufmann et al. (1972) observed electron and proton flux dropouts in the outer radiation belt with very rapid flux changes at the boundaries. The electron fluxes frequently changed abruptly within the one third second resolving time, whereas protons required about 1 to 10 seconds to change from one stable flux level to another. Kaufmann et al. concluded that the observed gradients were much too steep to be maintained as protons and electrons drift around the earth. They found, consistent with the conclusions of Yeager and Frank (1969), that the observed flux changes must be produced by the motion of a relatively steady monotonic flux gradient past the satellite. In the present investigation dropouts appeared with  $< 1$  second rise and fall times; three subsequent double order of magnitude flux changes occurred within a few seconds of each other. This phenomenon could result from either the fast motion of a structured flux gradient past the satellite or the complex motion of a monotonic gradient.

Several instances have been presented here (Figure 8) in which the VLF wave intensities displayed maxima near the times of the electron flux dropouts. This general relationship is consistent with the electron precipitation being caused by wave-particle interactions. However there are many times when VLF waves are enhanced without flux dropouts and vice versa. Many of the flux dropouts were associated with substorms and it has been shown with particle, wave field, and x-ray data that during a substorm most of the electron precipitation can be caused by wave-particle interactions (Kremser et al., 1986). However, at the  $L$  shells of concern a flux tube could not be emptied in less than several minutes even if complete isotropy existed. Furthermore, based on the known strengths of wave-particle interactions and the frequent occurrence of similar dropouts in both electrons and protons over a wide range of energies it is not expected that



January 25, 1995

many of the dropouts are caused by wave-particle interactions. At An effective mechanism for producing the wave enhancements would seem to involve changes in the global-scale magnetic field configurations and the occurrence of wave-particle interactions. Waves may be generated in association with pitch-angle scattering of electrons near the edge of the loss cone. One can only speculate on this interpretation since pitch-angle measurements near the loss cone were generally not made at the appropriate times during the dropout events considered here.

### Summary

Localized decreases of up to 3 orders of magnitude in the fluxes of electrons, protons and  $\text{He}^+$  particles have been observed within the outer radiation belt. The coordinated measurements of waves and magnetic field strengths add to our understanding of the flux behavior in the radiation belt. The data provide a basis for evaluating the importance of substorm activity, VLF wave intensities and magnetic field configuration changes. The measurements provide values for the radial shifts required to account for the flux dropouts. For the narrow dropouts the following conclusions can be drawn:

- At the times of many flux dropouts the VLF wave intensities were enhanced and the geomagnetic fields changed.
- Wave - particle interactions were probably not responsible for many of the flux dropouts, but the VLF wave enhancements may have been associated with the particle configurations.
- If produced solely by radial shifts of the particle population along paths similar to that of CRRES then large spatial movements ( $\Delta L > 0.5$ ) were often required.
- Consistent with the known occurrence of substorms at the times of dropouts observed from synchronous orbit satellites, AKR radiowave observations from CRRES suggest that substorms were present in more than about half of the narrow dropouts.
- Similar ion dropouts were present in approximately two-thirds of the narrow electron dropouts and absent in about one-third of the cases, indicating a variability in the responsible mechanisms.

January 25, 1995

- Some dropouts were observed to have  $< 1$  second rise and fall times indicating that they had not been present in the trapped population for long time periods.

The above considerations show that a variety of mechanisms may be responsible for flux dropouts and their relative importance may vary with location in the radiation belt as well as general activity conditions.

### References

- Anderson, R. R., D. A. Gurnett, and D. L. Odem, The CRRES plasma wave experiment, *J. Spacecr. Rockets*, 29, 570-573, 1992.
- Baker, D. N. and R. L. McPherron, Extreme energetic particle decreases near geostationary orbit: a manifestation of current diversion within the inner plasma sheet, *J. Geophys. Res.*, 95, 6591-6599, 1990.
- Baker, D. N., T. I. Pulkkinen, R. L. McPherron, J. D. Craven, L. A. Frank, R. D. Elphinstone, J. S. Murphree, J. F. Fennell, R. E. Lopez, and T. Nagai, CDAW 9 analysis of magnetospheric events on May 3, 1986: event C, *J. Geophys. Res.*, 98, 3815-3834, 1993.
- Collin, H. L., J. M. Quinn, G. R. Smith, E. Hertzberg, S. Roselle, and S. J. Battel, The low energy ion spectrometer (ONR-307-8-1, 2) on CRRES, *J. Spacecr. Rockets*, 29, 617-620, 1992.
- Erickson, K. N., R. L. Swanson, R. J. Walker, and J. R. Winckler, A study of magnetosphere dynamics during auroral electrojet events by observations of energetic electron intensity changes at synchronous orbit, *J. Geophys. Res.*, 84, 931-942, 1979.
- Imhof, W. L., R. M. Robinson, H. L. Collin, J. R. Wygant, and R. R. Anderson, Simultaneous equatorial measurements of waves and precipitating electrons in the outer radiation belt, *Geophys. Res. Lett.*, 19, 2437, 1992.

January 25, 1995

- Imhof, W. L., R. M. Robinson, H. L. Collin, J. R. Wygant, and R. R. Anderson, Simultaneous measurements of waves and precipitating electrons near the equator in the outer radiation belt, *J. Geophys. Res.*, 99, 2415-2427, 1994.
- Kaufmann, R. L., J. T. Horng, and A. Konradi, Trapping boundary and field-line motion during geomagnetic storms, *J. Geophys. Res.*, 77, 2780-2798, 1972.
- Korth, A., R. Friedel, D. N. Baker, H. Luhr, S. L. Ullaland, J. F. Fennell, and G. D. Reeves, Dynamics of the plasma sheet in the dawn sector of the magnetosphere: observations from CRRES. Submitted to the Proceedings of ICS-2 Fairbanks Alaska, April 19, 1994.
- Kremser, G., A. Korth, S. Ullaland, J. Stadsnes, W. Baumjohann, L. Block, K.M. Torkar, W. Riedler, B. Aparicio, P. Tanskanen, I.B. Iversen, N. Cornilleau-Wehrlin, J. Solomon and E. Arnata, Energetic electron precipitation during a magnetospheric substorm and its relationship to wave particle interaction, *J. Geophys. Res.*, 91, 5711-5718, 1986.
- Nagai, T., Local time dependence of electron flux changes during substorms derived from multi-satellite observations at synchronous orbit, *J. Geophys. Res.*, 87, 3456-3468, 1982.
- Nakamura, R., D. N. Baker, T. Yamamoto, R. D. Belian, E. A. Bering III, J. R. Benbrook, and J. R. Theall, Particle and field signatures during pseudobreakup and major expansion onset, *J. Geophys. Res.*, 99, 207-221, 1994.
- Nightingale, R. W., R. R. Vondrak, E. E. Gaines, W. L. Imhof, R. M. Robinson, S. J. Battel, D. A. Simpson, and J. B. Reagan, The ONR-307-3 spectrometer for electrons and protons on the CRRES Satellite, *J. Spacecr. Rockets*, 29, 614-617, 1992.
- Sauvaud, J. A., and J. R. Winckler, Dynamics of plasma, energetic particles, and fields near synchronous orbit in the nighttime sector during magnetospheric substorms, *J. Geophys. Res.*, 85, 2043-2056, 1980.
- Sergeev, V. A., T. Bosinger, R.D. Belian, G. D. Reeves, and T. E. Cayton, Drifting holes in the energetic electron flux at geosynchronous orbit following substorm onset. *J. Geophys. Res.*, 97, 6541-6548, 1992.

January 25, 1995

- Singer, H. J., W. P. Sullivan, P. Anderson, F. Mozer, P. Harvey, J. Wygant, and W. McNeil, The fluxgate magnetometer instrument on the Combined Release and Radiation Effects Satellite (CRRES), *J. Spacecr. Rockets*, 29, 599-601, 1992.
- Su, Shin-yi, T. A. Fritz, and A. Konradi, Repeated sharp flux dropouts observed at 6.6 RE during a geomagnetic storm, *J. Geophys. Res.*, 81, 245-252, 1976.
- Voots, G. R., D. A. Gurnett, and S. I. Akasofu, Auroral kilometric radiation as an indicator of auroral magnetic disturbances, *J. Geophys. Res.*, 82, 2259-2266, 1977.
- Voss, H. D., E. Hertzberg, A. G. Ghielmetti, S. J. Battel, K. L. Appert, B. R. Higgins, D. O. Murray, and R. R. Vondrak, Medium energy ion mass and neutral atom spectrometer, *J. Spacecr. Rockets*, 29, 566-569, 1992.
- Walker, R. J., K. N. Erickson, R. L. Swanson, and J. R. Winckler, Substorm-associated particle boundary motion at synchronous orbit, *J. Geophys. Res.*, 81, 5541- 5550, 1976.
- Wygant, J. R., P. R. Harvey, D. Pankow, F. S. Mozer, N. Maynard, H. Singer, M. Smiddy, W. Sullivan, and P. Anderson, The CRRES electric field/Langmuir probe instrument, *J. Spacecr. Rockets*, 29, 601-604, 1992.
- Yeager, D. M. and L. A. Frank, Large temporal variations of energetic electron intensities at midlatitudes in the outer radiation zone, *J. Geophys. Res.*, 74, 5697-5708, 1969.

#### Acknowledgments

The SEP, IMS-LO, and IMS-HI are part of the ONR307 experiment on CRRES, and much of the data analysis presented here was sponsored by the Office of Naval Research (contract N00014-83-C-0476). The Lockheed Independent Research Program provided partial support for the analysis. Special thanks are extended to J. P. McGlennon for his dedicated data analysis contributions. Appreciation is give for the contribution of R. R. Vondrak. The research effort at the University of Iowa has been supported by NASA under subcontract 9-X29-D9711-1 with Los Alamos National Laboratory. Special thanks go to R. W. Lane for his programming efforts and to M.D.

January 25, 1995

Brown for producing the data plots. The U. C. Berkeley work was performed under Air Force contract F19628-92-K-0009.

### Figure Captions

1. Fluxes of various energy electrons, protons, and alpha particles as well as electric field intensities.
2. In the top section are plotted the fluxes of electrons, protons, and alpha particles. In the bottom section is a color spectrogram of the Iowa wave data.
3. Fluxes of various energy electrons, protons, and alpha particles as well as electric field intensities.
4. In the top section are plotted the fluxes of electrons, protons, and alpha particles. In the bottom section is a color spectrogram of the Iowa wave data.
5. Time profiles of the absolute magnetic field strengths and the z components of the field strength, the 256 Hz wave intensities, and the 56 keV proton fluxes.
6. Time profiles of the absolute magnetic field strengths and the z components of the field strength, the 256 Hz wave intensities, and the 56 keV proton fluxes.
7. VLF wave intensities and electron flux versus time for orbit 666.
8. VLF wave intensities for different satellite passes.
9. The L shell versus magnetic local time for narrow dropouts.
10. Differences in L shell for the same electron flux at the start of recovery of the dropouts as at the nearest position with the same flux level.
11. Fluxes of various energy electrons and protons plotted as a function of time and associated ephemeris parameters. (Left section). Fluxes of 53 keV electrons and magnetic field strengths plotted as a function of time. (Right section).

Table 1. Characteristics of Narrow and Broad Dropouts (Do)

orbit	date	at start of recovery						ion	L at	Max L	$\Delta L$	DO In	VLF Hz	AKR
		UT (h)	UT (sec)	MLT	L	Kp	Dst	B/Bo	DO flux					
									comp. to			an hour	wave	yes/no
									elect. DO				enh.	
Narrow Dropout (<30min)														
186	10/10/90	7.6	27360	02.9	05.41	6	-114	02.65	07.79	8.4	2.38	4	narrow	no
186	10/10/90	12.8	46080	06.5	07.20	5	-88	03.10	07.87	8.4	0.67	2	no	no
279	11/17/90	14.3	51480	02.9	06.76	4	-36	01.71	-	6.8	>0.04	3	narrow	weak
370	12/24/90	22.45	81000	01.0	06.46	4	-47	01.27	-	6.8	>0.34	1		
542	3/5/91	14.04	50544	23.4	06.76	4	-30	01.81	06.26	6.8	0.5	1	narrow	no
547	3/7/91	14.72	52992	23.0	06.96	4	-20	01.87	06.95	6.9	0.01	1	narrow	weak
552	3/9/91	17.6	63360	23.9	06.24	3+	-30	02.45	-	7.0	>0.76	2	narrow	weak
583	3/22/91	9.45	34020	22.9	06.43	4	-38	01.33	-	6.7	>0.27	1	narrow	no
615	4/4/91	11.24	40464	21.9	07.22	6+	-3	02.39	07.13	7.2	0.09	3	broad	no
666	4/25/91	9.5	34200	21.9	06.75	3	-21	02.43	-	7.0	>0.25	1	narrow	weak
686	5/3/91	12.4	44640	20.3	08.05	3	-22	03.91	-	8.2	>0.15	1	narrow	yes
712	5/14/91	5.3	19080	21.1	06.29	3+	-28	01.34	-	6.7	>0.41	1	no	no
719	5/17/91	0.75	2700	20.2	06.61	6	13	01.06	-	6.7	>0.09	1	no	no
737	5/24/91	11.45	41220	20.9	07.07	2+	-19	04.15	-	7.9	>0.83	1	narrow	weak
759	6/2/91	10.48	37728	19.8	07.89	4	-43	03.91	07.95	8.0	0.06	1	narrow	yes
766	6/5/91	4.2	15120	17.8	05.95	7+	-76	01.48	06.68	7.3	0.73	1	broad	no
768	6/6/91	3.88	13968	18.5	06.68	6	-147	01.65	-	6.7	>0.02	1	broad	weak
902	8/2/91	9.81	35316	18.0	05.98	5+	-91	01.80	06.63	7.7	0.65	3	narrow	no
Broad Dropout ( $\geq 30$ min)														
186	10/10/90	9.3	33480	04.3	07.95	6-	-180	03.91	-	8.4	>0.45	4	narrow	no
259	11/9/90	7.5	27000	02.2	06.63	3-	-22	04.45	-	8.6	>1.97	2	delayed	yes
547	3/7/91	13.24	47664	22.1	06.65	4-	-29	01.40	-	6.9	>0.25	1	delayed	yes
591	3/25/91	13.81	49716	21.3	06.85	8-	-166	01.85	-	7.3	>0.45	1	broad	yes
591	3/25/91	17.35	62460	23.6	06.24	6-	-139	03.16	-	7.3	>1.06	0	broad	yes
613	4/3/91	13.3	47880	20.4	06.34	5	-69	01.67	-	7.5	>1.16	1	delayed	yes
686	5/3/91	13.4	48240	20.9	08.12	3	-25	04.98	-	8.2	>0.08	0	broad	yes
759	6/2/91	10.2	36720	19.6	07.97	4	-43	03.79	-	8.0	>0.03	1	broad	yes

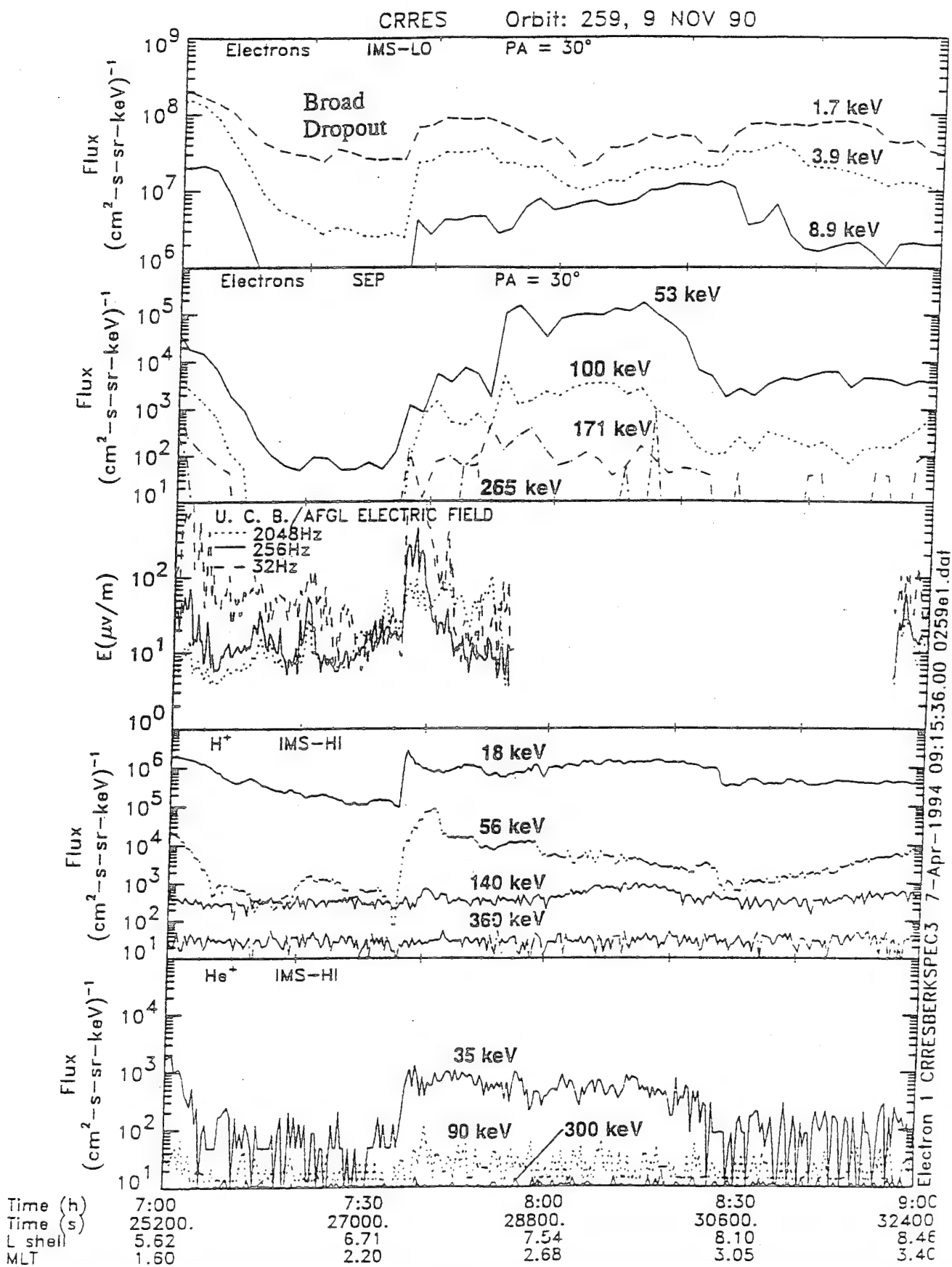


Figure 1



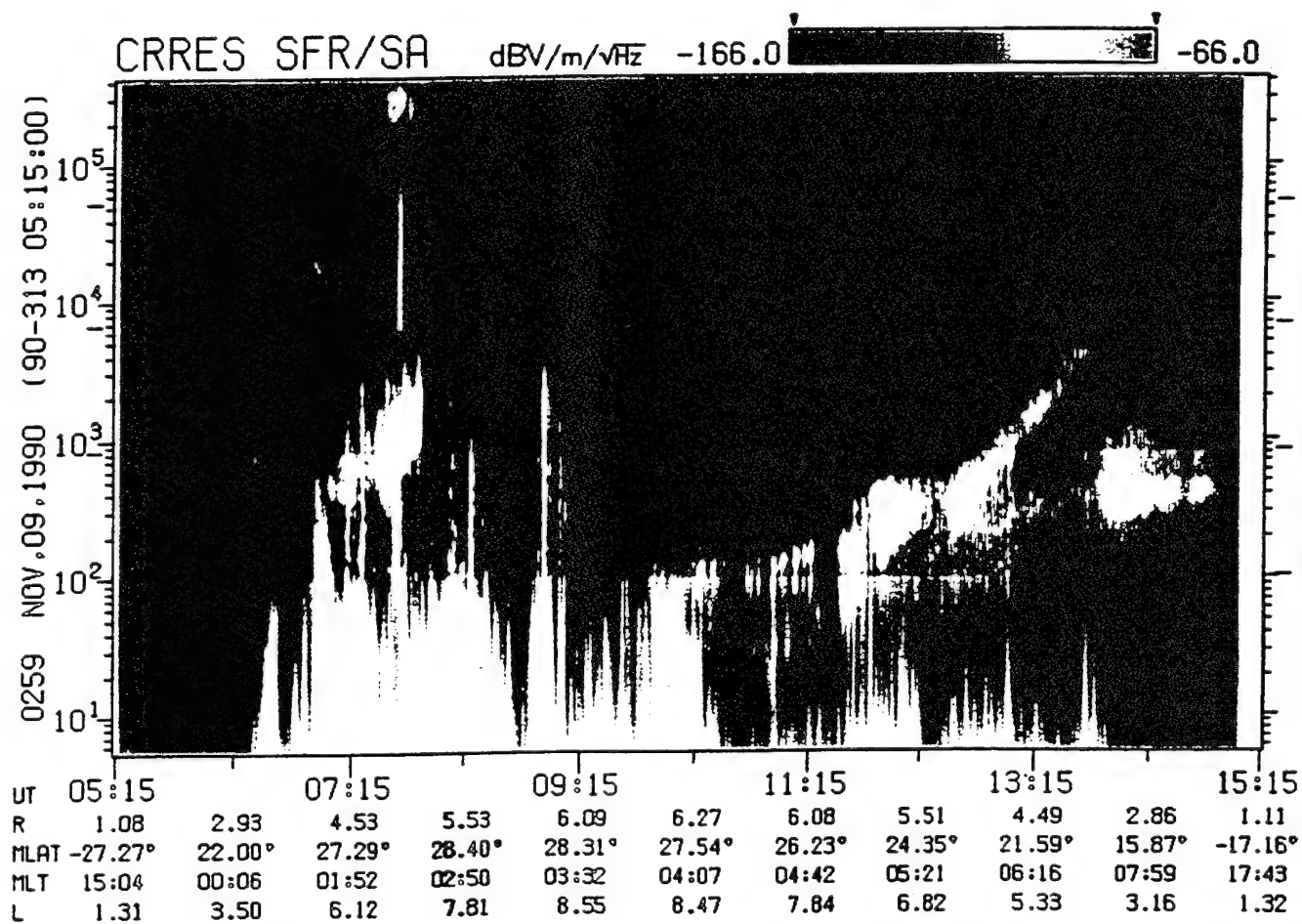
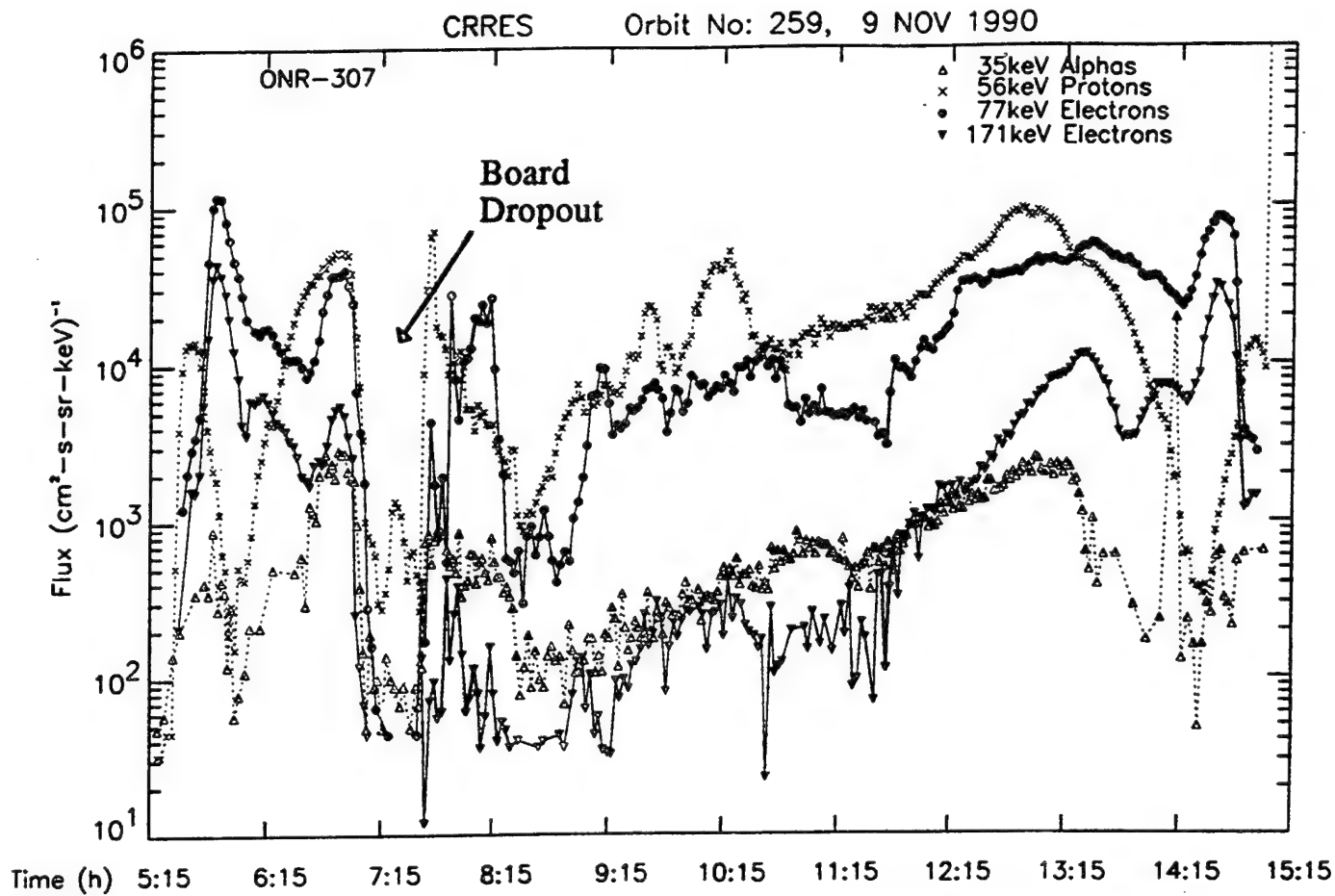


Figure 2



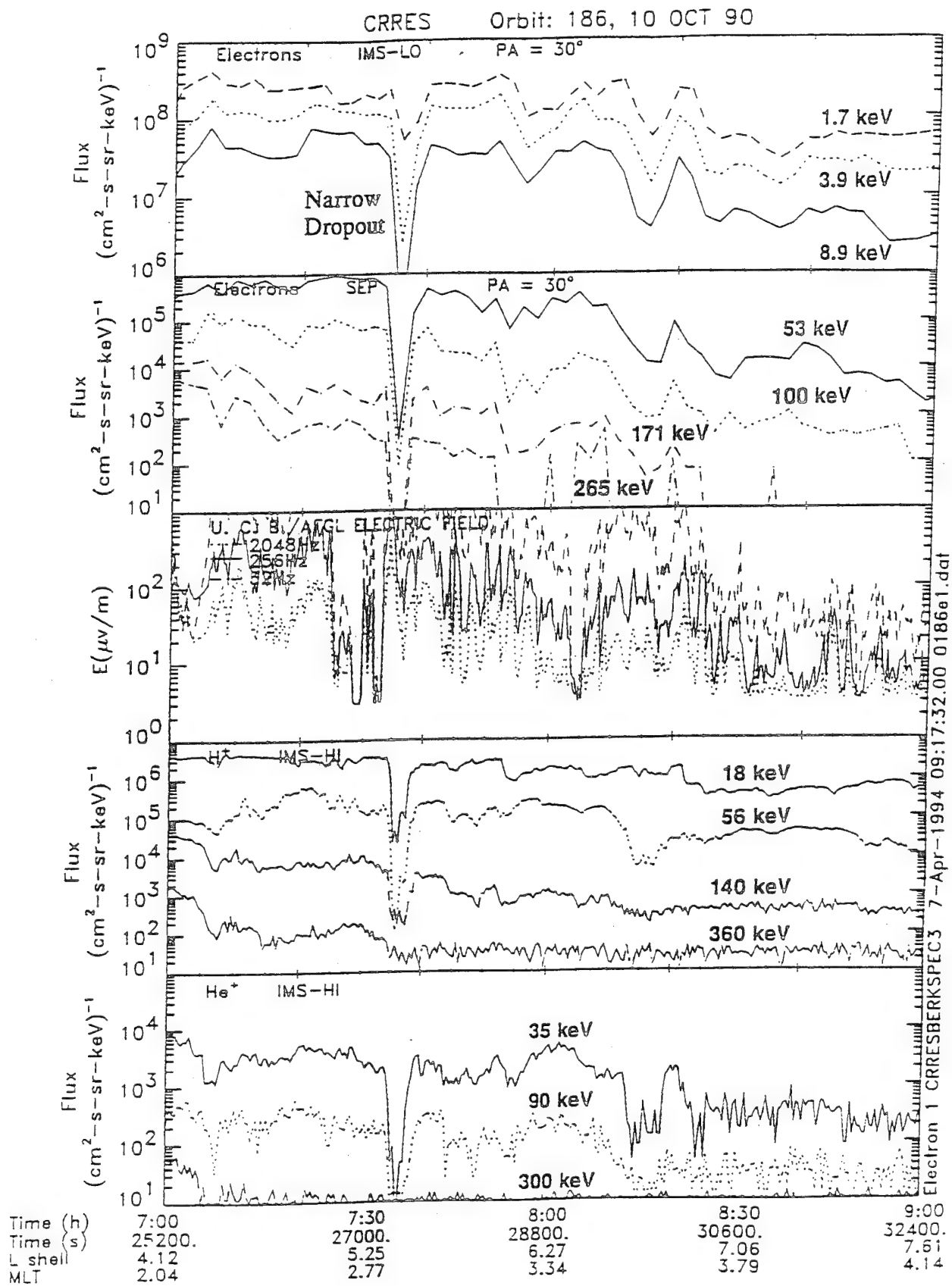


Figure 3

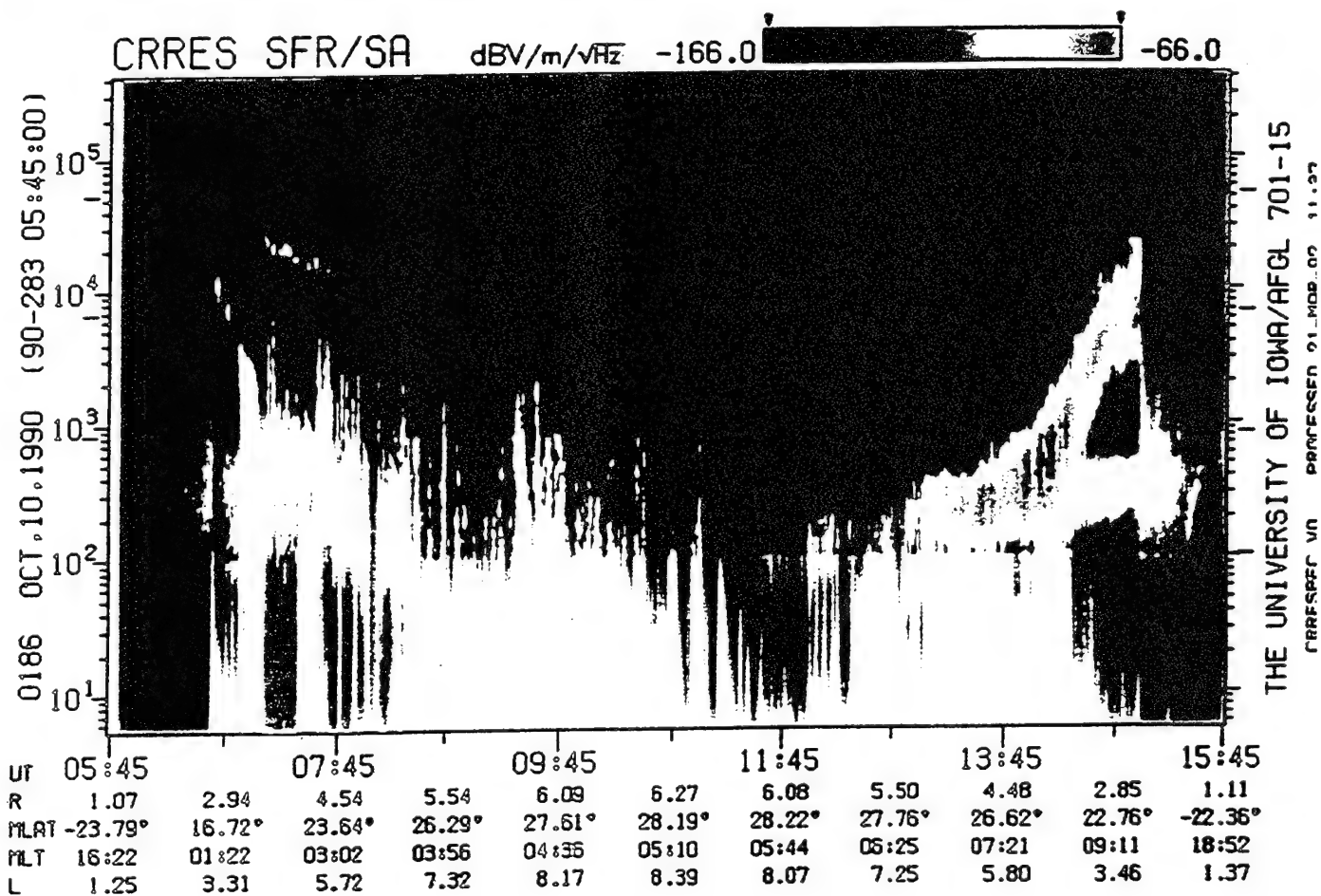
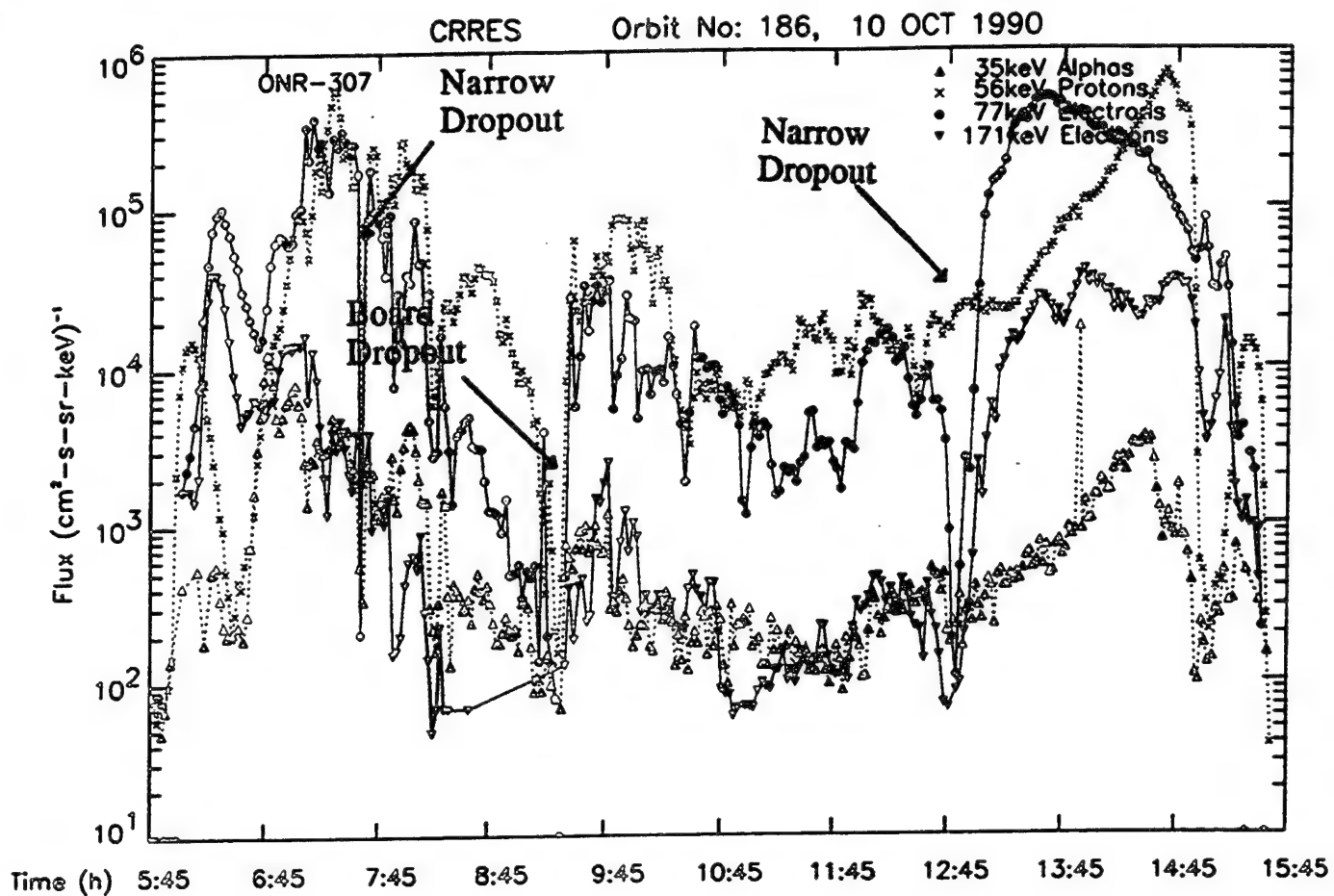


Figure 4

# CRRS

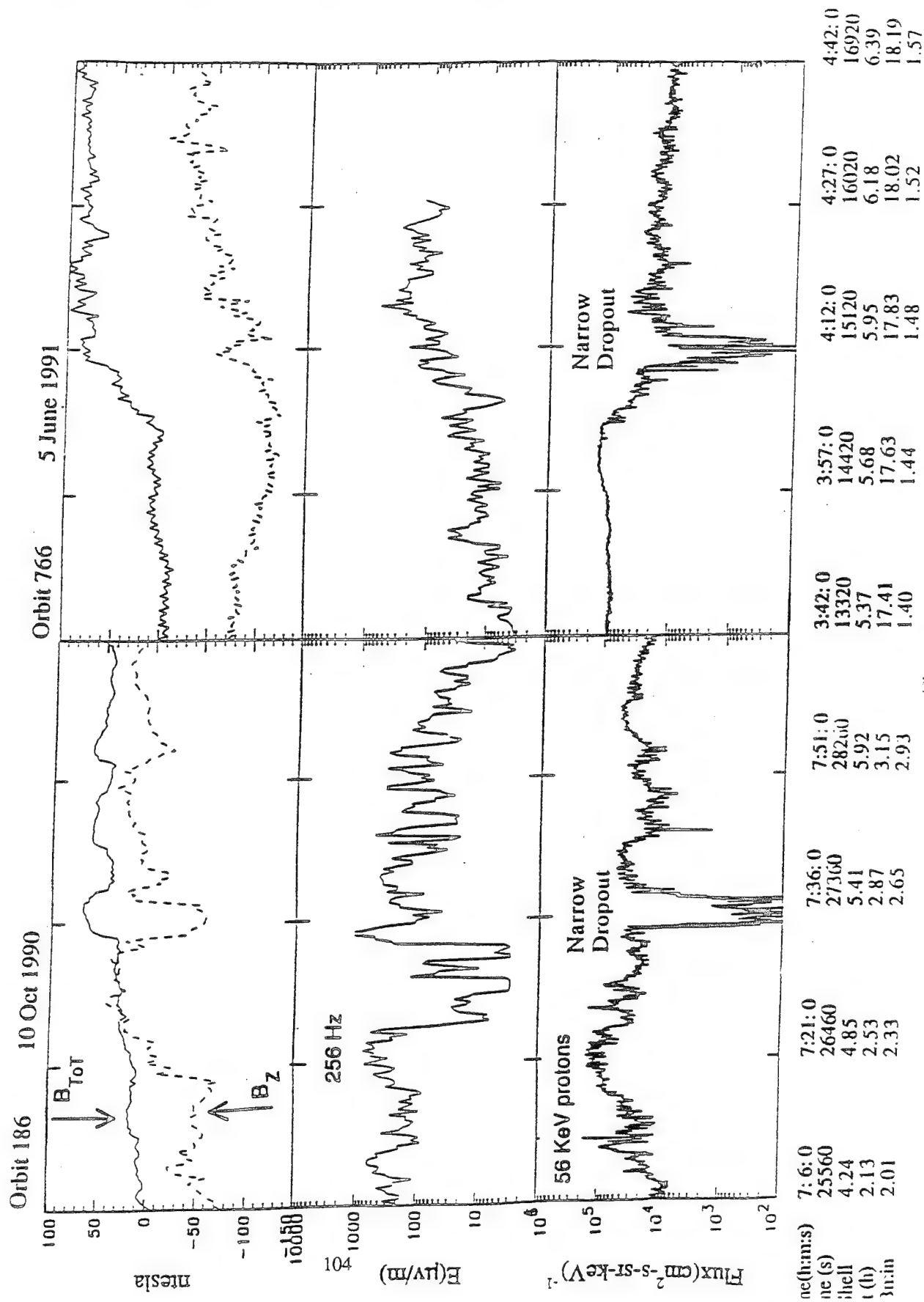


Figure 5

# CRRES

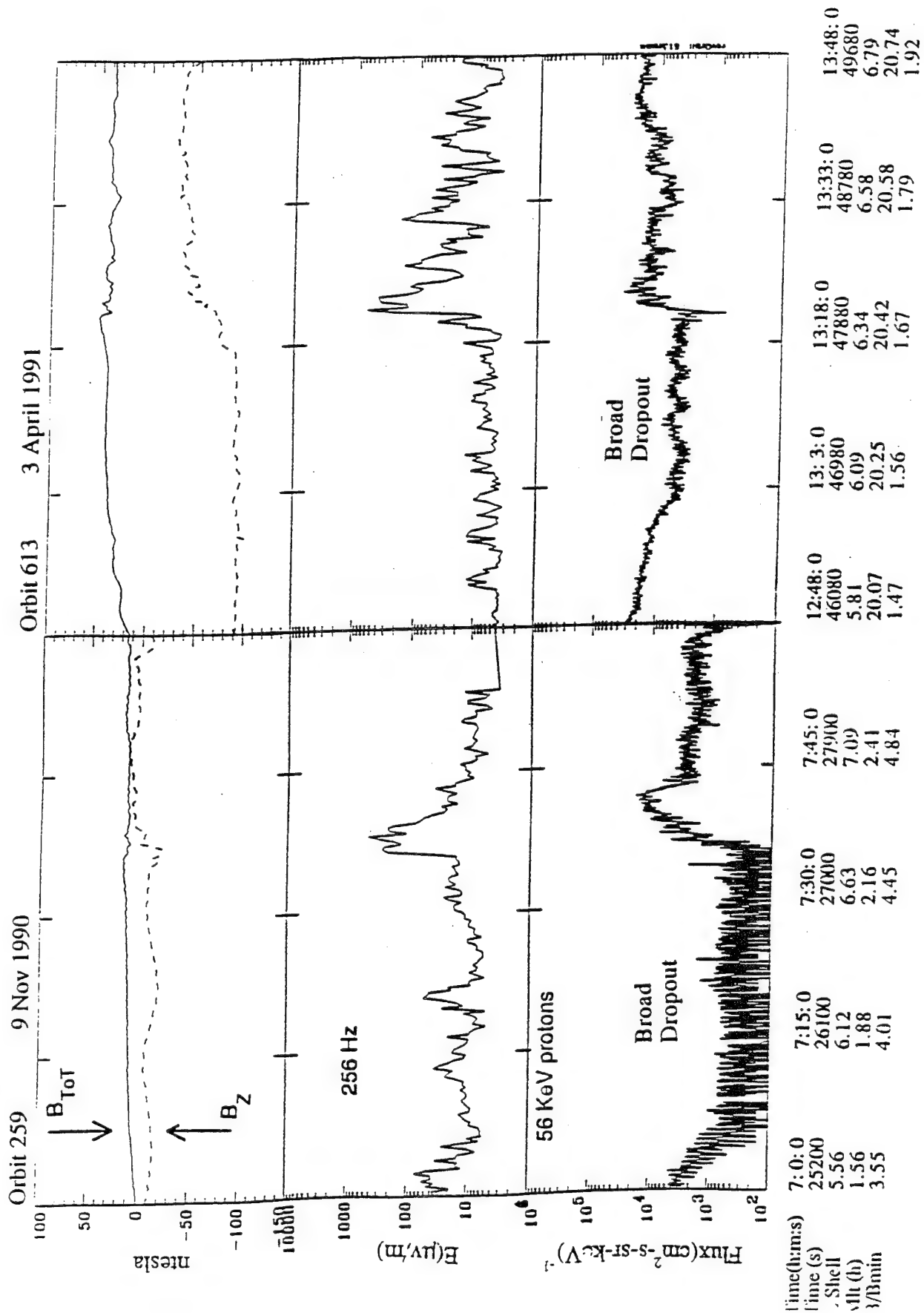


Figure 6

# CRRES Orbit 666 25 April 1991

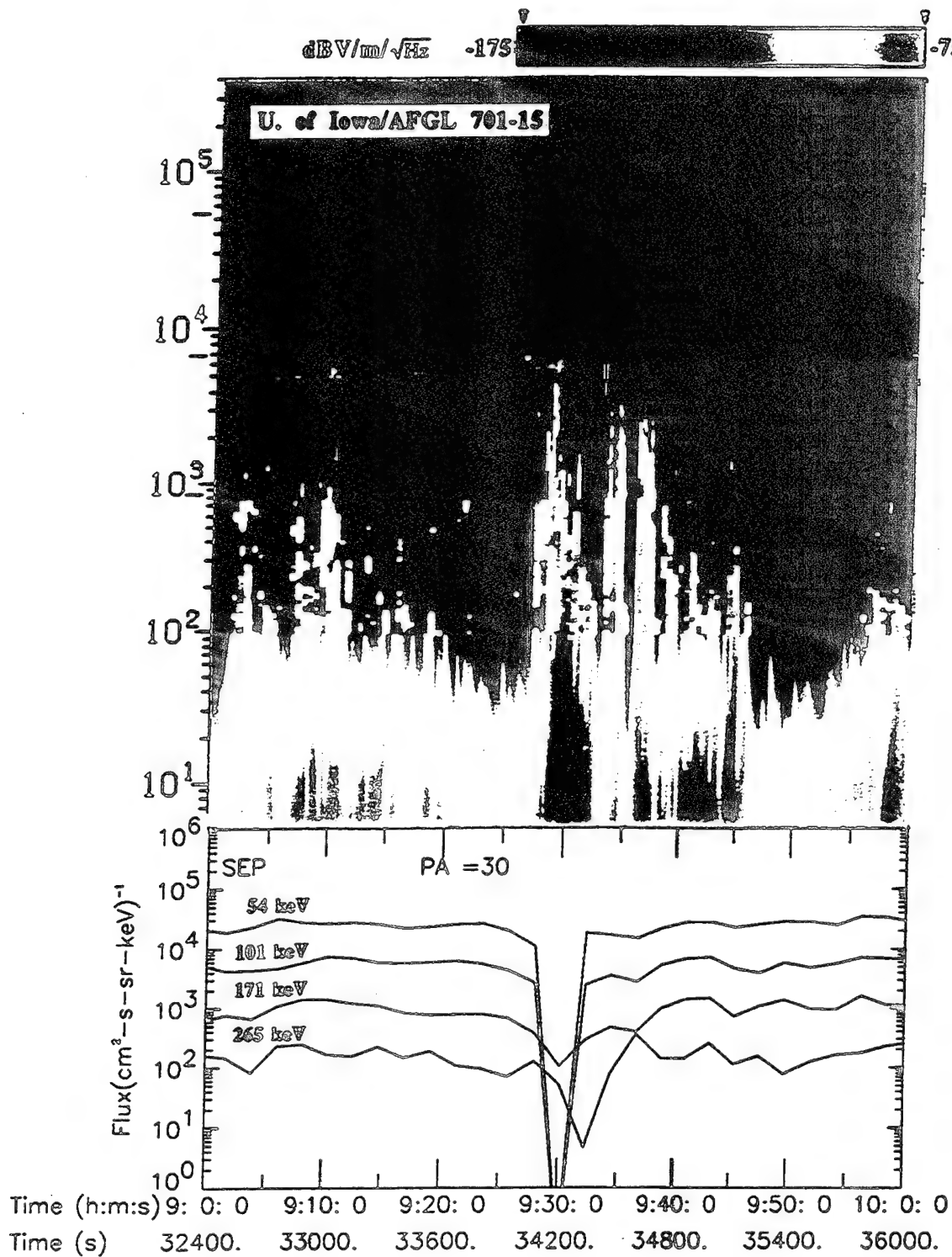


Figure 7

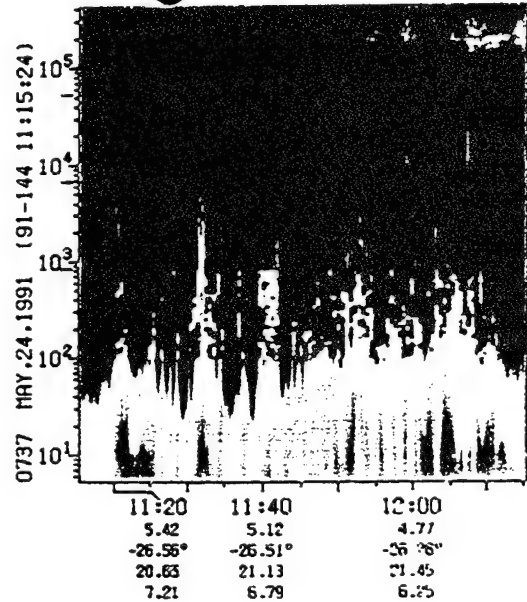
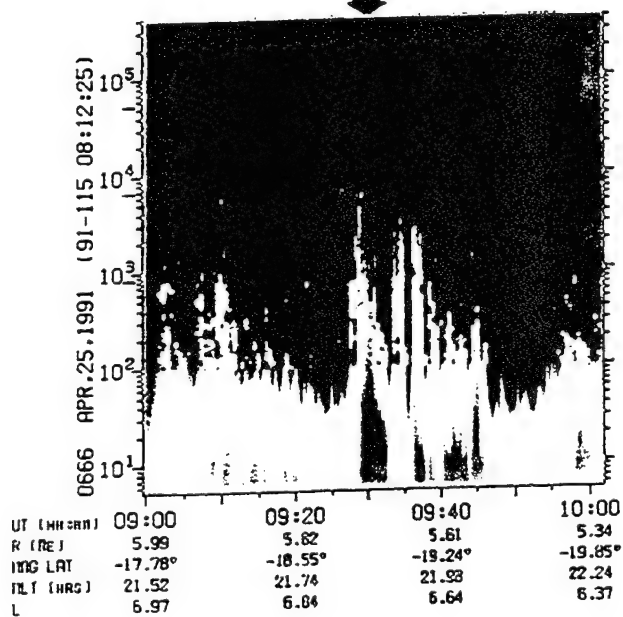
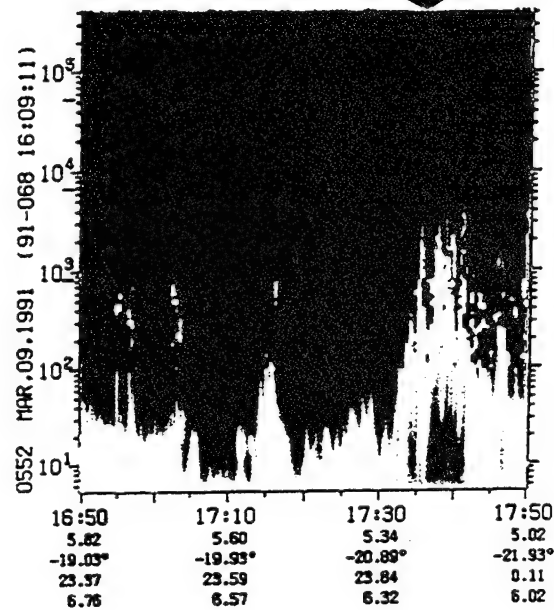
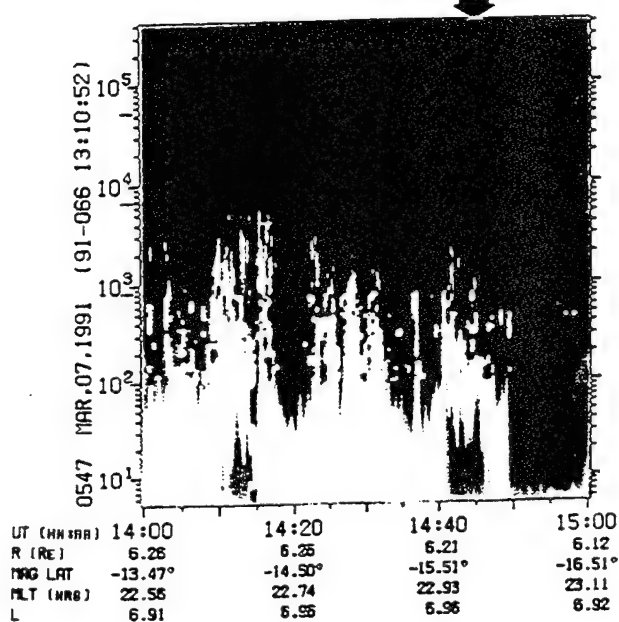


Figure 8

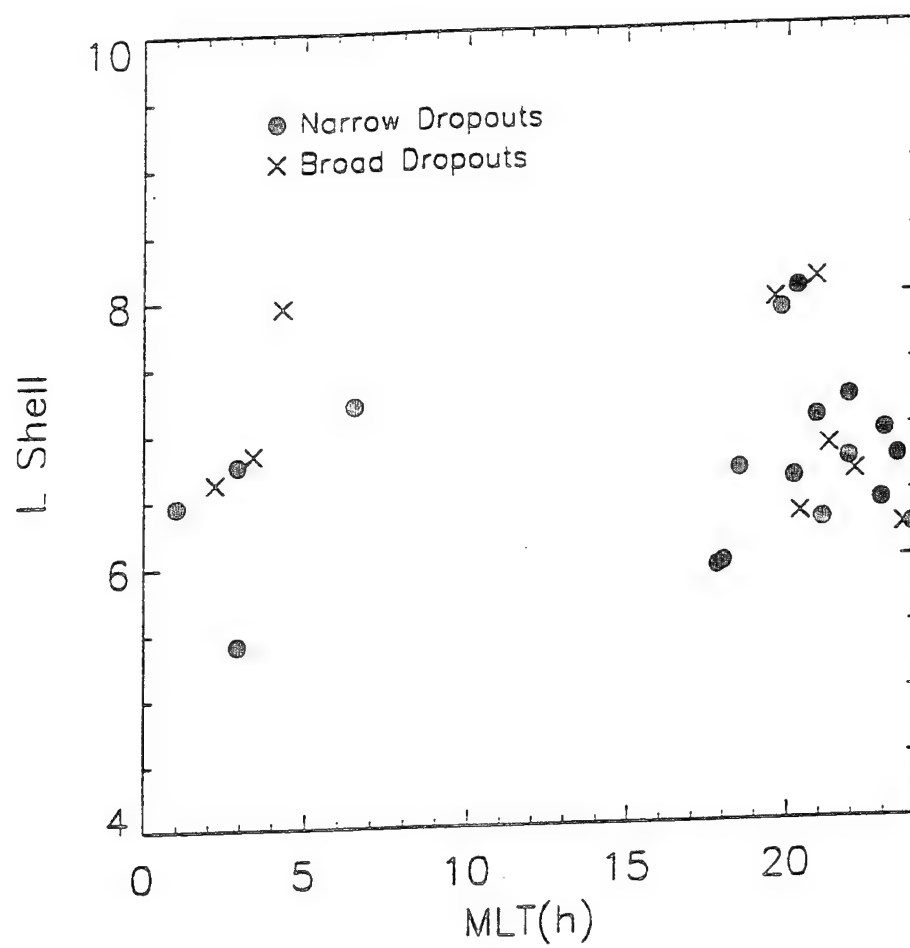


Figure 9

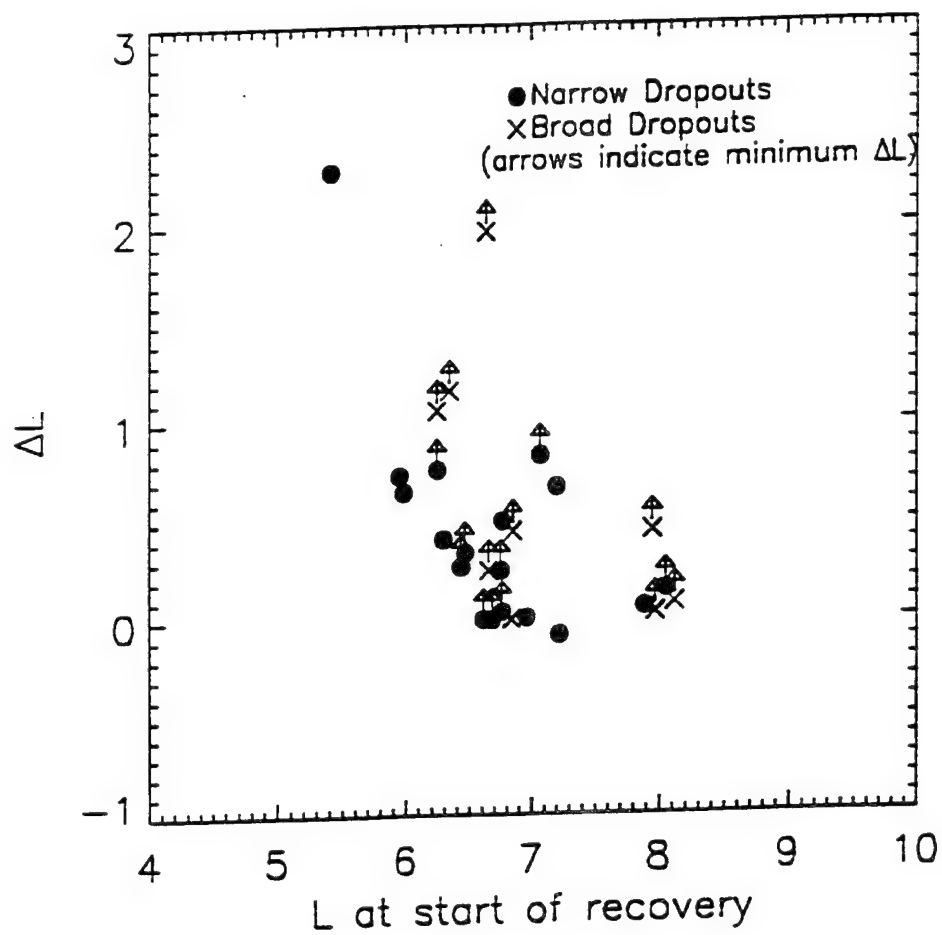
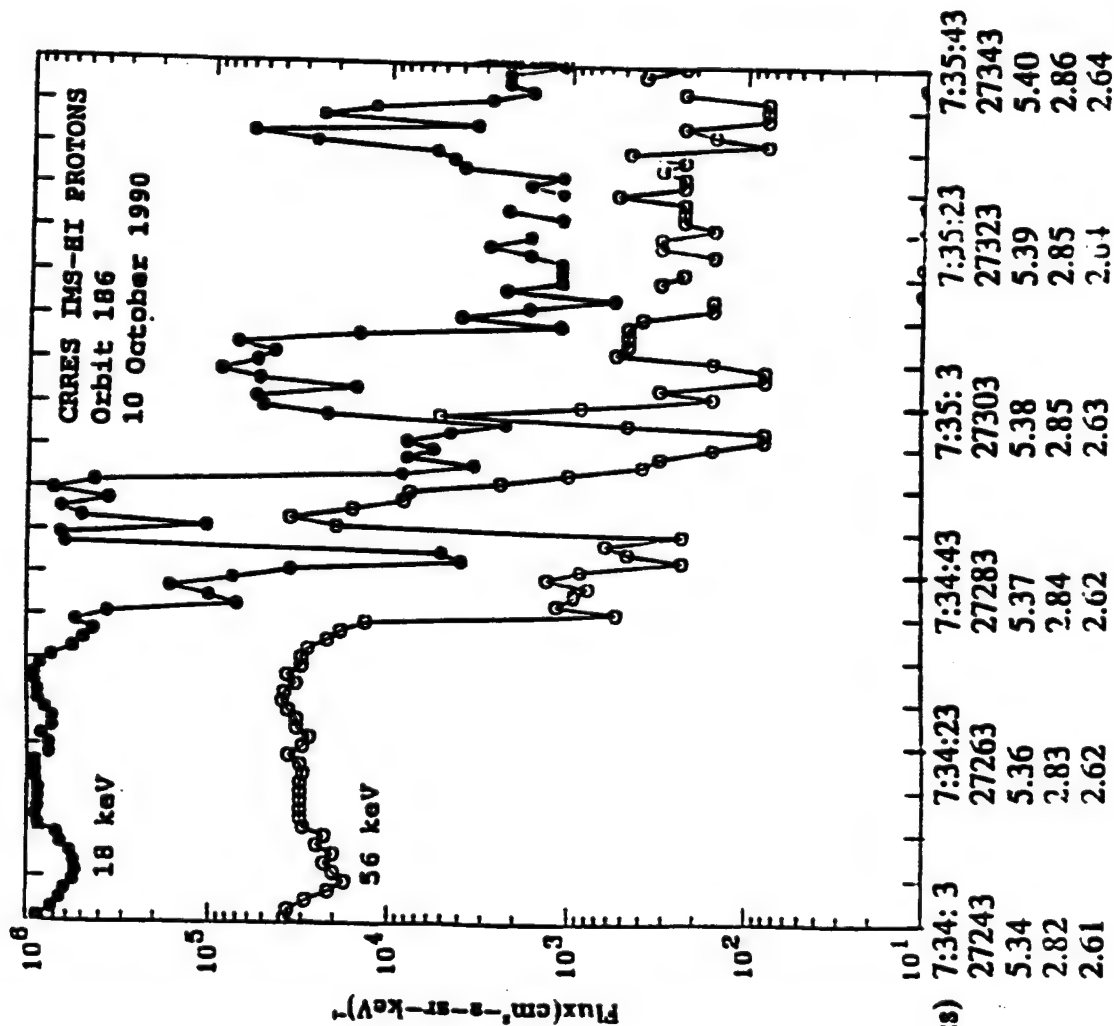
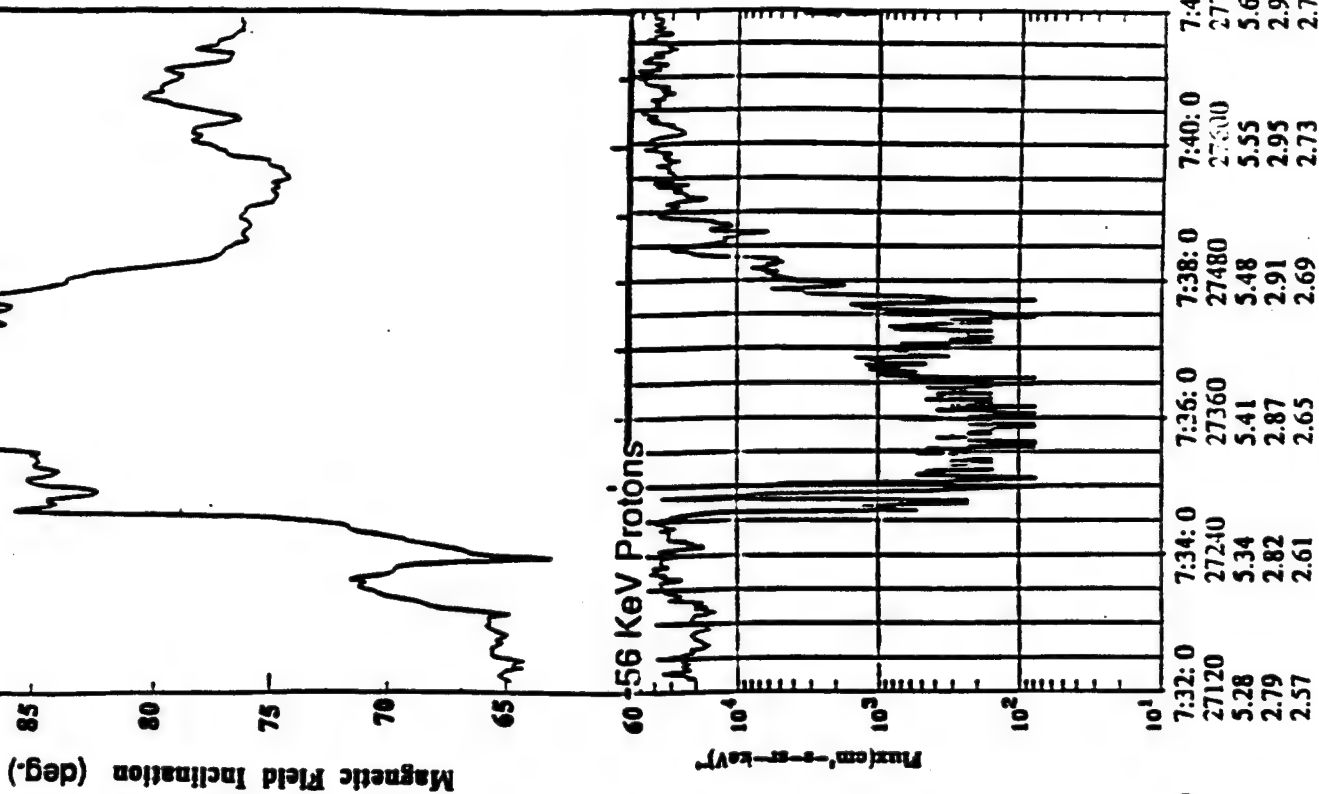


Figure 10





Time(h:m:s)  
Time (s)  
L Shell  
Mlt (h)  
B/Bmin

Figure 11

## **Appendix 5**

### **Abstracts of Papers Presented**

CRRES IMS-HI Energetic Ion Composition  
Measurements During the August 1990  
and March 1991 Storms

1. 1991 Fall Meeting

H.D. Voss J. Mobilia and R.A. Baraze (Lockheed Palo  
Alto Research Laboratory, 3251 Hanover St., Palo  
Alto, CA 94304)

The energetic ion composition (10 to 2000 keV-AMU/q<sup>2</sup>) during the 26 August 1990 and 24 March 1991 storms provides unique insight into the dynamics of the radiation belts compared to quiet-time profiles. The IMS-HI (ONR 307-8-3) spectrometer on the CRRES satellite measures the energetic ion composition, energy spectrum charge, and pitch angle distribution with good mass, temporal, and spectral resolution. One of the instrument detectors measures neutrals with ion rejection of  $< 100 \text{ MeV/AMU/q}^2$ . Because IMS-HI has a relatively large geometric factor and 100% duty cycle the instrument is well suited for mapping the fluxes of radiation belt H<sup>+</sup>, He<sup>+</sup>, O<sup>+</sup>, O<sup>++</sup>, and neutrals during quiet time periods and for the study of wave-particle interactions and the loss-cone fluxes. For the August storm ULF waves in H<sup>+</sup> and O<sup>+</sup> are observed as precursors to the sudden commencement and occur in both storms during several of the injection events. A product of the IMS-HI investigation is to obtain an energetic particle database of the penetrating radiation fluxes for specifying and modeling the radiation belt environment.

Observations from the IMS-HI (ONR 307-8-3)  
Energetic Neutral and Ion Composition  
Instrument on the CRRES Satellite

1. 1991 Fall AGU mee:

J. Mobilia H.D. Voss and R.A. Baraze (Lockheed  
Palo Alto Research Laboratory, 3251 Hanover St.,  
Palo Alto, CA 94304)

Observations made with the IMS-HI (ONR 307-8-3) energetic neutral and ion composition instrument on the CRRES satellite will be presented. CRRES was launched into a geosynchronous transfer (350 x 33500 km) orbit on 25 July 1990 at an inclination of 18.1 degrees and period of ~10 hours. The IMS-HI spectrometer simultaneously measures mass, charge, and energy for 10 to 2000 keV-AMU/q<sup>2</sup> ions with high time resolution and 100% duty cycle. The instrument consists of seven detectors with the seventh measuring neutrals in the 10 to 1500 keV range. The major magnetospheric ions, H<sup>+</sup>, He<sup>+</sup>, O<sup>+</sup>, and O<sup>++</sup> are measured with high sensitivity which allows good radiation belt mapping. Intensity modulations in the particle distribution have been observed on numerous occasions and will be discussed. The energetic neutral atoms and ion composition profiles are used as a basis for developing models of the radiation belt populations.

**CRRES Energetic Particles and Ion Composition Measurements  
During the March 1991 Storm**

1. 1991 Fall Meeting

R. M. Robinson, H. L. Collin, H. D. Voss, R. R. Vondrak, R. W. Nightingale and W. L. Imhof, (Lockheed Palo Alto Research Laboratory, 3251 Hanover St., Palo Alto, CA 94304)

The ONR 307 experiment package on the Combined Release and Radiation Effects Satellite (CRRES) consists of three different types of instruments that measure particle fluxes and ion composition with good temporal and angular resolution. The Spectrometer for Electrons and Protons (SEP) measures electrons with energies from 40 keV to 5 MeV and protons with energies between 900 keV and 40 MeV. The low energy ion mass spectrometer (IMS-LO) measures electrons and major ions between 110 eV and 35 keV. The medium energy ion mass spectrometer (IMS-HI) measures the composition of ions at ring current energies. The development of the March 1991 storm over the energy ranges and particle types sampled by the ONR 307 instruments will be described. The SEP instrument monitored the dramatic increases in energetic electrons and protons associated with the storm including the onset of the solar proton event at 1100 UT on 23 March and the second proton belt beginning at 0400 UT on 24 March. The IMS-LO data show persistent dispersive signatures in the ion fluxes that are suggestive of multiple injection events. Dynamic variations in the low energy plasma fluxes were observed near apogee in association with the storm. The IMS-HI measurements provide information about the behavior of the ring current. The data from these three experiments are inter-compared to study the relative responses of electrons and ions over a broad energy range throughout the storm period.

Spring Agu 1992

**Intense  $>10$  MeV Particle Injection Near  $L=2.5$  During the 24 March  
1991 Magnetic Shock**

**H D Voss W L Imhof M Walt J Mobilia R M Robinson and  
R W Nightingale**  
(Lockheed Palo Alto Research Laboratory,  
3251 Hanover St, Palo Alto, CA 94304)

On 24 March 1991 a strong magnetospheric shock reached the Earth at 3:42 UT. Between 3:42 and 3:54 the ONR 307 instruments on the CRRES satellite measured impulsive bursts of  $>10$  MeV electrons, protons, and alphas in the slot region ( $2.1 < L < 2.5$ ) near the equator at 3 MLT. The electron bursts are consistent with drift echos of about 15 MeV while the protons are consistent with drift echos of  $>20$  MeV. Particle measurements were obtained with the High-Energy Ion Mass Spectrometer (IMS-HI) and the Spectrometer for Electrons and Protons (SEP) which are part of the ONR 307 experiment on CRRES. IMS-HI uses a 7 KG magnet and 7 solid-state detectors to analyze ion mass and energy. No medium energy  $18 \text{ keV} < E < 1.5 \text{ MeV}$  ion bursts were observed at this time. However, in the neutral detector, which is also sensitive to protons with  $E > 50 \text{ MeV}$ , a particle burst was observed 0.5 minutes before the electron peak. SEP employs a telescope of three solid-state detectors and is surrounded by a scintillator. During the burst event the instrument scanned through 8 logic modes to measure electrons ( $40 \text{ keV} < E < 5 \text{ MeV}$ ), protons ( $0.9 < E < 100 \text{ MeV}$ ), and alphas ( $7 < E < 24 \text{ MeV}$ ). Simultaneous injection/acceleration of  $> 10 \text{ MeV}$  particles at  $L \sim 2.5$  with a sudden commencement is surprising and suggests that an unexpected acceleration mechanism is active in that region.

Acceleration of Particles to  $> 10$  MeV at  $L=2.5$   
during a Sudden Commencement

1. 1992

H. D. VOSS (Lockheed Palo Alto Research Laboratory, Palo Alto, California 94304)

Simultaneous injection/acceleration of  $>10$  MeV particles at  $L$  of about 2.5 with a magnetic storm onset is surprising and suggests a powerful injection mechanism. On 24 March 1991, between 0342 and 0354 UT, the particle instruments on the CRRES satellite observed impulsive bursts of  $>10$  MeV electrons, protons and alphas in the slot region ( $2.1 < L < 2.5$ ) near the equator at 0300 MLT. The origin of this event is puzzling and any proposed theory must explain the following key data: 1) the narrow longitude spread and brief interval of injection inferred from the short 5 s pulse width of the electrons, 2) the preferential acceleration of high energy electrons, protons and alphas of MeV energies, 3) the greater injected particle energy at lower  $L$ , 4) the 30 second delay between proton and electron peaks, and 5) the nearly simultaneous acceleration of particles with a sudden commencement. To investigate the first order physics, a simple model was formulated using a dipole earth field and a dynamic magnetosphere produced by an approaching image dipole. Using the 100 gamma increase observed on CRRES over a 40 s interval the standoff distance drops to about 3 Re. Particles initially near noon at  $3 < L < 10$  are transported below 3 Re and accelerated (a factor of about 10 for 7 Re initial position) by adiabatic compression assuming that the first invariant is conserved. Because of the compression, the constant  $B$  particle drift contours are shifted sunward so that the slot region has momentary *direct access* to the magnetosphere acceleration region. For  $>10$  MeV particles the longitude drift periods are short ( $< 3$  min.) allowing the particles to drift out of the compression region to low  $L$  on the night side. After the initial magnetopause compression to  $\sim 3$  Re it appears that the standoff distance retreats in about 1 minute to somewhat larger distances so that the  $>10$  MeV particles injected into the slot region violate the third invariant.

# SATELLITE INSTRUMENTATION FOR IMAGING ENERGETIC NEUTRAL ATOMS

H.D. Voss, J. Mobilia, H.L. Collin, and W.L. Imhof  
Dept. 91-20, Bldg. 255  
Lockheed Palo Alto Research Laboratory  
3251 Hanover St.  
Palo Alto, Ca. 94303  
Phone: 415-424-3299  
Fax:: 415-424-3333

We wish to submit this abstract to the conference "Instrumentation for Magnetospheric Imagery " (S. Chakrabarti) at San Diego ' 92

Direct measurements of energetic neutral atoms (ENA) and ions have been obtained with the cooled solid state detectors on the low altitude (220 km) three-axis stabilized S81-1/SEEP satellite and on the spinning  $1.1 \times 6$  Re CRRES satellite. During magnetic storms ENA and ion precipitation is evident over the equatorial region from the LE spectrometer in the SEEP payload (ONR 804) on S81-1. The spinning motion of the CRRES satellite allows for simple mapping of the magnetosphere using the IMS-HI (ONR 307-8-3) neutral spectrometer. This spectrometer covers the energy range from 20 to 1000 keV and uses a 7 kG magnetic field to screen out protons less than about 50 MeV. Recently, an advanced spectrometer (SEPS) has been developed to image electrons, ions, and neutrals on the despun platform of the POLAR satellite ( $\sim 1.8 \times 9$  Re) for launch in 1994 as part of the NASA ISTP/GGS program. For this instrument a 256 element solid state pixel array has been developed that interfaces to 256 amplifier strings using a custom 16 channel microcircuit chip. In addition, this instrument features a motor controlled iris wheel and anticoincidence electronics.

H. D. Voss received his B.S. degree in Electrical engineering from Illinois Institute of Technology in 1972 and M.S. and PhD. degrees in space physics from the University of Illinois, Urbana in 1974 and 1977, respectively. From 1977 to 1979 he developed 10 rocket payloads as a research associate at U. of Illinois. From 1979 to present he has been with the Lockheed Palo Alto Research Laboratory where he has been directly involved with the development of energetic particle, plasma, X-ray, optical, and dust instruments for satellites. He is the author or co-author of over 60 scientific papers in space physics.



**Narrow Flux Drop-offs and Enhancements in the Outer  
Radiation Belt, Association With Waves and Magnetic  
Fields**

W.L. Imhof, H.D. Voss, J. Mobilia, H.L. Collin (Lockheed Palo Alto  
Research Laboratory, Palo Alto, California 94304)

J.R. Wygant, (Space Sciences Laboratory, University of California,  
Berkeley, California 94720)

R.R. Anderson, (Department of Physics and Astronomy, University  
of Iowa, Iowa City, Iowa 52242)

H.J. Singer, (Space Environment Laboratory, NOAA R/E/SE,  
Boulder, Colorado 80303)

An investigation has been made of localized decreases and increases in the energetic particles, some at positions deep within the trapped population of the radiation belt. The study was performed with measurements of electrons, protons and He<sup>+</sup> particles at near equatorial position from the CRRES satellite. Electric field wave and magnetic field strength data recorded on CRRES were also used. Narrow observation time drop-offs near midnight with widths of only a few minutes well within the trapped population occurred at L shells as low as 5.4. Drop-offs occurred in both electrons and protons, and on some occasions with very similar flux profiles whereas in other cases there were major differences such as no proton flux decreases at the times of large changes in the electrons. Other events typically at higher L shells had slow decreases in particle flux followed by rapid increases, consistent with those often observed from synchronous orbit satellites and attributed to substorms, as substantiated by observations of AKR. Repeated narrow duration drop-offs and enhancements were sometimes observed around a broad event. The CRRES measurements of flux variations with L shell indicate that if the flux decreases are produced by a radial shift of the particle population, large spatial movements are required. Coordinated measurements of waves and magnetic field strengths are used to provide important information on the source(s) of fine-structure flux variations.